Synthesis and Characterisation of New Cathode Materials for Second Generation Sodium Batteries

Irene Munaó

University of
St Andrews

This thesis is submitted in partial fulfilment for the degree of PhD
at the
University of St Andrews

February 2017

1. Candidate's declarations:

I, Irene Munaó, hereby certify that this thesis, which is approximately 29,000 words in length, has been written by me, and that it is the record of work carried out by me, or principally by myself in collaboration with others as acknowledged, and that it has not been submitted in any previous application for a higher degree.

I was admitted as a research student in September, 2013 and as a candidate for the degree of PhD in August, 2014; the higher study for which this is a record was carried out in the University of St Andrews between 2013 and 2017.

Date …… signature of candidate……

2. Supervisor's declaration:

I hereby certify that the candidate has fulfilled the conditions of the Resolution and Regulations appropriate for the degree of PhD in the University of St Andrews and that the candidate is qualified to submit this thesis in application for that degree.

Date …… signature of supervisor ……

3. Permission for publication:

In submitting this thesis to the University of St Andrews I understand that I am giving permission for it to be made available for use in accordance with the regulations of the University Library for the time being in force, subject to any copyright vested in the work not being affected thereby. I also understand that the title and the abstract will be published, and that a copy of the work may be made and supplied to any bona fide

library or research worker, that my thesis will be electronically accessible for personal or research use unless exempt by award of an embargo as requested below, and that the library has the right to migrate my thesis into new electronic forms as required to ensure continued access to the thesis. I have obtained any third-party copyright permissions that may be required in order to allow such access and migration, or have requested the appropriate embargo below.

The following is an agreed request by candidate and supervisor regarding the publication of this thesis:

PRINTED COPY

Embargo on all or part of print copy for a period of one year on the following ground:

- Publication would preclude future publication

Supporting statement for printed embargo request if greater than 2 years:

Two further papers are still to be published that describe work discussed in the thesis.

ELECTRONIC COPY

Embargo on all or part of electronic copy for a period of one year on the following ground:

- Publication would preclude future publication

Supporting statement for electronic embargo request if greater than 2 years:

Two further papers are still to be published that describe work discussed in the thesis.

ABSTRACT AND TITLE EMBARGOES

I agree to the title and abstract being published YES

Date …….

signature of candidate ……

signature of supervisor ……

Abstract

This thesis reports exploratory studies on the synthesis and characterisation of new compounds as cathode materials for second generation sodium batteries, with a particular emphasis on preparing new iron-phosphite and molybdenum oxyfluoride cathode materials.

Seven different compounds are hereby reported: the sodium iron fluoro-phosphite of formula $NaFe_3(HPO_3)_2[(H,F)PO_2OH)_6]$, the iron-phosphite $Fe_2(HPO_3)_3$, the sodium iron-phosphite $NaFe(H_2PO_3)_4$, the sodium iron phosphate $NaFe(HPO_4)(H_2PO_4)_2 \cdot H_2O$ and three molybdenum oxyfluoride compounds of formula $Na_2MoO_2F_4$, $KNaMoO_2F_4$ and $KMoO_2F_3$.

The synthesis of these compounds was performed by hydrothermal and solvothermal methods at temperatures ranging from 100 °C to 160 °C. The compounds were then fully characterised using the following techniques: single crystal X-ray diffraction (SXD), powder X-ray diffraction (PXRD), energy-dispersive X-ray spectroscopy (EDX), elemental analysis (EA), infrared spectroscopy (IR), thermogravimetric analysis (TGA) and electrochemical testing. Magnetic properties have also been studied where appropriate.

Acknowledgements

I would like to thank the University of St Andrews and Professor Philip Lightfoot for giving me the opportunity to work at this project.

A special thanks to Dr Cameron Black, Dr Lucy Clark, Dr Robert Armstrong and Dr David Cordes for their priceless scientific guidance and invaluable help during my whole PhD time, together with their precious friendship.

I am particularly grateful to Professor Alexandra Slawin for our chats, her moral support and friendship, especially in the last part of my time in St Andrews.

I have been really lucky finding so many precious friends during my PhD. A special thanks to Dr Orlando Santoro, Dr Federico Grillo, Dr Tania Triscari Barberi and Dr Brunello Nardone who have been more than a second family to me.

Finally, the biggest thanks are for my parents who supported me every time and everywhere, teaching me how to be an adventurous and enthusiastic person, and to Dr Stefano Guidone, who has always been by my side, donating me smiles, music and love.

Contents

Chapter 1

Introduction

1.1 The energy storage issue

In the last decades, the energy storage issue has become a growing global concern due to the increased energy demand, together with the increased price of fossil fuels and improved environmental regulations in order to have more environmentally responsible alternative sources for both energy generation and storage.

In the last few years, electrochemical energy storage (EES) technologies based on batteries have been shown to be promising solutions for large-scale energy storage, due to their high efficiency, flexibility, compact size, long cycle life and low maintenance. In addition, batteries are really useful systems for storing intermittent energy provided by renewable resources, such as wind turbines and photovoltaic energy, where it is necessary to manage peak load energy and load-level output fluctuations.

Since they were discovered, lithium ion batteries have played a key role in the EES technologies, due to their high efficiency and portability, hence there has been a rapid increase in the demand for lithium ion batteries as a major power source in portable electronic devices and vehicles, such as hybrid-electric and plug-in electric vehicles. However, even if lithium ion batteries will certainly play an important role in the next generation of EES systems, a few concerns over them have been revealed.[1,2] In

particular, the increased demand for lithium and the relatively low global availability of lithium resources have increased its cost. In addition, the most easily accessible global lithium reserves are located in remote or in politically sensitive areas.[2,3,4,5]

Together with the limited availability of some transition metals for cathode materials, these concerns shifted the development of more sustainable EES systems to those based on more suitable elements, such as Fe, Mo and Na. Sodium is a globally abundant natural resource and more economically available. Together with its redox potential [$E^o(Na^+/Na)$= -2.71 V *vs* the standard hydrogen electrode] which is only 0.3 V above that of lithium, these features make sodium a really promising element for EES applications (Table 1.1).[2]

Table 1.1 Principal characteristics of sodium and lithium battery materials against Standard Hydrogen Electrode (S.H.E.).

Characteristics	Na	Li
Price (for carbonates) (£ kg^{-1})	0.06-0.30	3.29-3.59
Capacity density (A h g^{-1})	1.16	3.86
Voltage *vs* S.H.E. (V)	-2.7	-3.0
Ionic radius (Å)	0.98	0.69
Melting point (°C)	97.7	180.5

1.2 General aspects of sodium ion cells

The first sodium ion batteries were developed in the 1980s, together with the lithium batteries.[2,7-13] Since the 1990s, lithium ion batteries had a greater success in portable electronics applications due to their higher energy density, higher potential and lower mass. However, for stationary applications where portability is not required, sodium ion batteries are potentially an equally useful technology. However, insufficient cycle life

and the need for the discovery of new materials for both the positive and the negative electrodes are big issues for this type of battery which need to be solved in order to increase their performance. For this reason, more attention and research have been focused on sodium ion battery technology in order to make them available in the coming years.

A sodium ion battery consists of two different electrodes immersed in an electrolyte and separated from each other by a salt bridge. The electrolyte is an ionic conductor and allows the passage of anions or cations. On discharge, an electrolytic cell converts chemical energy to electrical energy through oxidation-reduction reactions. The typical working system of a sodium ion battery shows sodium ions leaving the positive electrode, with a typical working potential of 3 V *vs* Na^+/Na, in order to reach the negative electrode, with a working potential of 1 V vs Na^+/Na, passing through the salt bridge during the battery charge. During the battery discharge, an oxidation reaction occurs at the anode (negative electrode) and electrons are released to the external circuit. These electrons are then accepted by the cathode (positive electrode) from the external circuit and the cathode is reduced during the electrochemical reaction. Sodium ions are de-intercalated from the negative electrode and migrate across the electrolyte and re-intercalated in the positive electrode. The process is spontaneous because characterised by a favourable free energy which allows the battery to release energy to the device attached to the battery. During the battery charge, the positive electrode is oxidised and electrons released in the external circuit. Sodium ions are de-intercalated from the positive electrode, migrate across the electrolyte and are then intercalated back into the negative electrode (Table 1.2, Figure 1.1, Figure 1.2).[2]

Table 1.2 Oxidation-reduction reactions in a sodium battery during charge and discharge.

Discharge *(spontaneous)*

	Oxidation	Reduction
Negative electrode (Anode)	$Na \rightarrow 2Na^+ + 2e^-$	
Positive electrode (Cathode)		$Na_{1-x}M + xNa^+ + xe^- \rightarrow NaM$

Charge *(no spontaneous)*

	Oxidation	Reduction
Negative electrode (Anode)		$2Na^+ + 2e^- \rightarrow Na$
Positive electrode (Cathode)	$NaM \rightarrow Na_{1-x}M + xNa^+ + xe^-$	

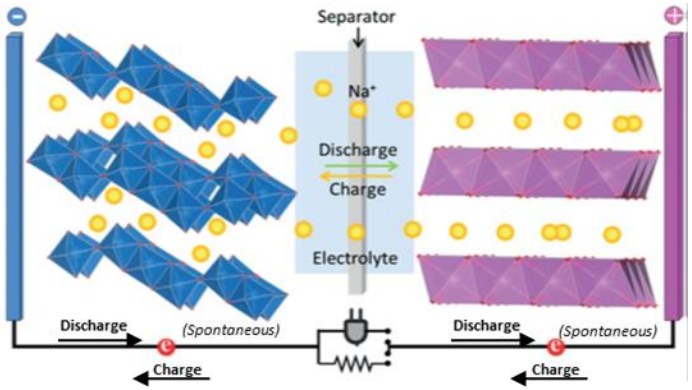

Figure 1.1. Typical working system for sodium ion batteries. Sodium ions migrate in the electrolyte between the negative and positive electrodes during charge and discharge. The electron flow happening through the external electrical circuit counterbalances the sodium ion flow. The resulting difference of potential between the positive and negative electrodes defines the cell voltage. Taken from reference 2 with permission of Angew. Chem. Int. Ed.

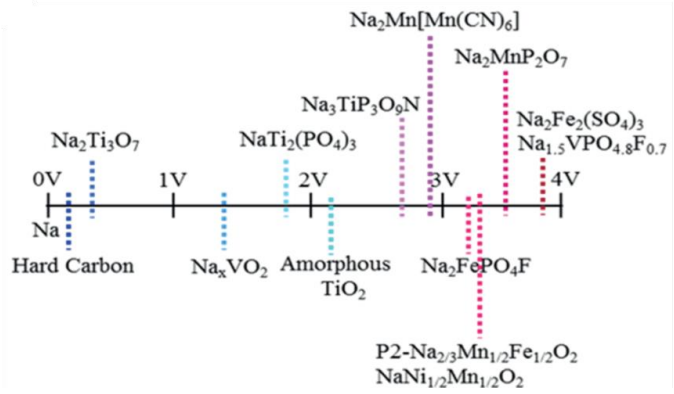

Figure 1.2. Relative working potential of a few typical electrode materials for sodium ion batteries. Taken from reference 2 with permission of Angew. Chem. Int. Ed.

The most common negative electrode for batteries is composed of graphitic carbons. However, due to the fact that sodium atoms do not intercalate significantly in this kind of material, they are replaced by hard carbons, such the ones prepared by pyrolysis, reaching reversible capacities close to 300 mAh g^{-1}.[14-20]

One of most important issues prohibiting 100% of Coulombic efficiency in sodium batteries is related to on-site reactions occurring between the electrolyte and electrode surfaces, which do not permit the return of sodium ions after the charge process. A C-rate is a measure of the rate at which a battery is discharged relative to its maximum capacity. A 1C rate means that the discharge current will discharge the entire battery in one hour. Commonly, a C-rate of 1 C is known as a one-hour discharge, a 0.5 C (or C/2) is a two-hour discharge and 0.2 C (or C/5) is a 5-hour discharge.[2]

1.3 Cathode materials for sodium ion batteries

1.3.1. Layered sodium transition-metal oxides

Layered sodium transition-metal oxides, characterised by the general formula AMO_2 (with A = Na, M = Co, Fe, Mn)[21-24] have been deeply studied in the past as high performance cathode materials. These materials are classified as different types on the basis of the orientation of the different close-packed oxygen layers. In particular, following the notation of Delmas, it is possible to define the O3 (ABCABC) and P2 (ABAB) types, in which the ions of sodium occupy octahedral and prismatic sites respectively.[25] These materials show structural phase transitions when their sodium ions are extracted. In particular, in the O3 type the oxygen packing changes from the "ABCABC" to the "ABBCCA" of the P3 type phase due to a glide translation of the MO_2 slabs, without breaking the M-O bonds.[25-28] In the P2 type, instead, the prismatic site are stabilised by the big sodium ions so, when they are extracted, the MO_2 slabs move to form octahedral sites, leading to the formation of the new O2 type phase characterised by "ABACAB" oxygen packing (Figure 1.3).[25-30]

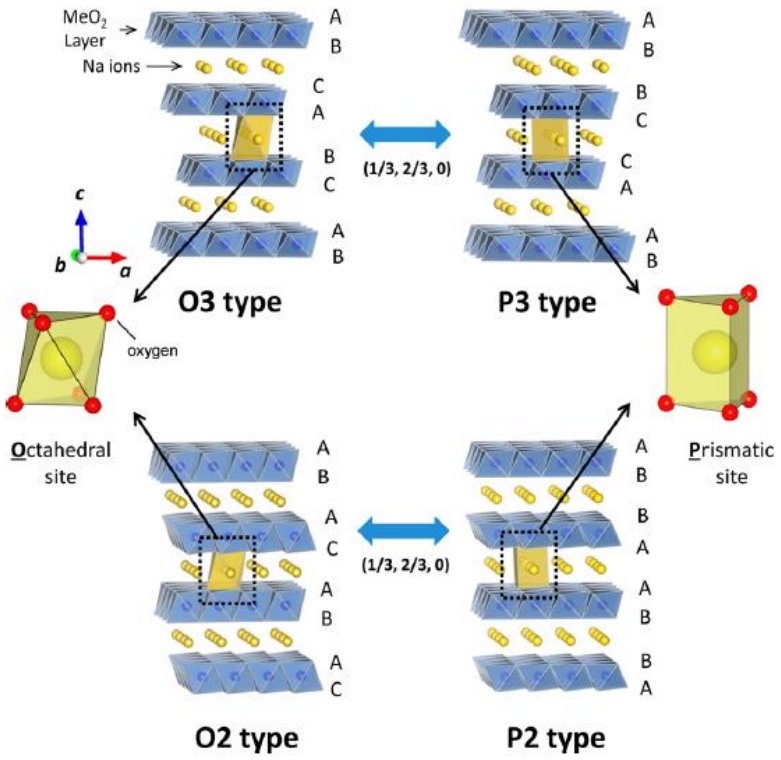

Figure 1.3. Classification of Na-*M*-O layered materials. MO_6 octahedra in blue and sodium ions in yellow. The phase transition processes induced by the extraction of sodium ions are indicated as glide vectors (1/3,2/3,*z*) and (1/3,2/3,*z*). Taken from reference 28 with permission of Chem. Rev.

Na_xCoO_2 compounds

The Na_xCoO_2 system had been studied as a cathode material since the 1980s.[26,32] Four different phases of Na_xCoO_2 are known; α-Na_xCoO_2 (O3-type), α'-Na_xCoO_2 (O′3), β-Na_xCoO_2 (P′3) and γ-Na_xCoO_2 (P2). Experimental studies reported in the literature, confirm that the P2 phase is usually obtained at higher temperature (650 - 900 °C) for $0.55 < x < 0.88$, while the other three phases, O3, O′3 and P′3, are obtained at lower T (500 °C - 550 °C) with $0.92 < x < 1.00$, $0.75 < x < 0.83$ and $0.60 < x < 0.67$, respectively. The O3-O′3 phase transition occurs at room temperature for $0.88 < x < 1$

(Figure1.4).[25,33] The O and P classifications refer to the local structure around the sodium ions, in particular if each oxygen atom is located in an octahedral or prismatic site. The numerical classification is related to the repeat period of the transition metal stacking perpendicular to the sodium layers. In the O′3 and O3, all sodium ions are located in edge sharing octahedral sites. At the contrary, the P′3 structure is characterised by sodium ions displaying prismatic coordination with one side sharing and another face sharing with a Co octahedron. The symbol A, B and C indicate the layers of oxygen with different stacking (Figure 1.4).[33]

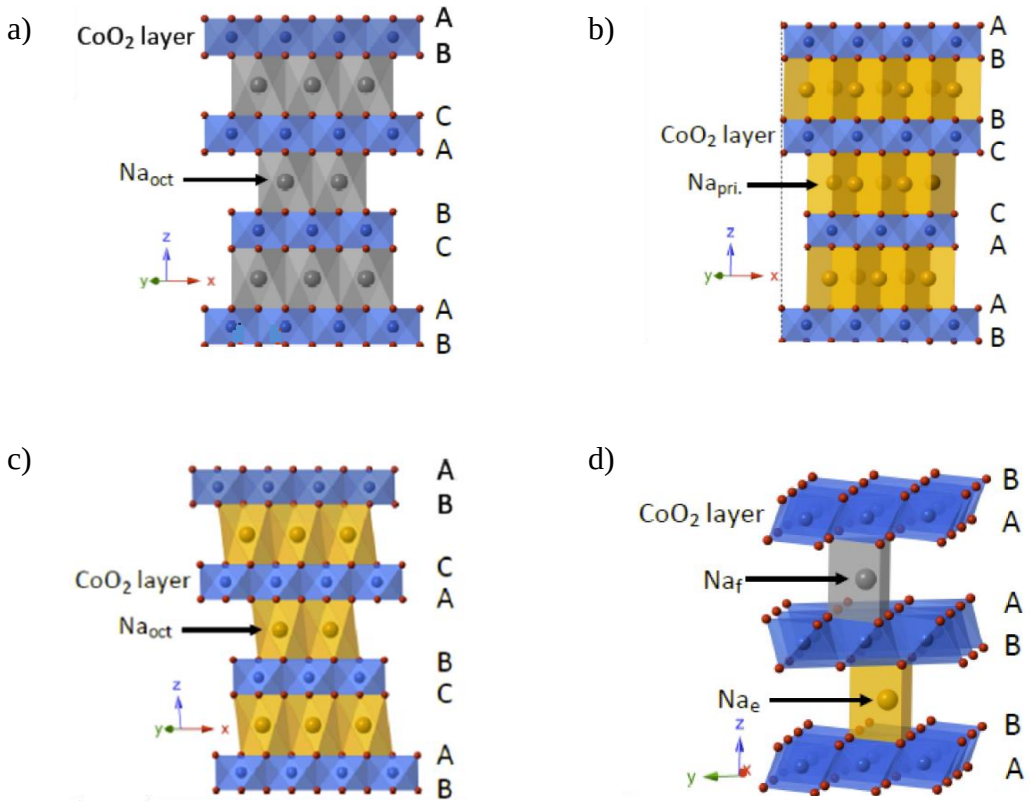

Figure 1.4. Different polytypes of Na_xCoO_2: a) O3 type, b) P′3 type, c) O′3 type, d) P2 type; CoO_2 layers in blue, sodium octhaedra in yellow, oxygen atoms in red. Taken from reference 33 with permission of Chem. Mater.

The O3-type is electrochemically active with up to 0.5 sodium ions able to be extracted and intercalated, leading to a phase transition to the O′3 and the P3-types, permitting layer gliding at room temperature as the sodium concentration changes.[26,34]

Na_xFeO_2 compounds

These kind of materials are characterised by high redox potentials and high energy densities. The $NaFeO_2$ compound exists in two polytypes, α-$NaFeO_2$ and β-$NaFeO_2$, but only α-$NaFeO_2$ is electrochemically active (Figure 1.5).[31]

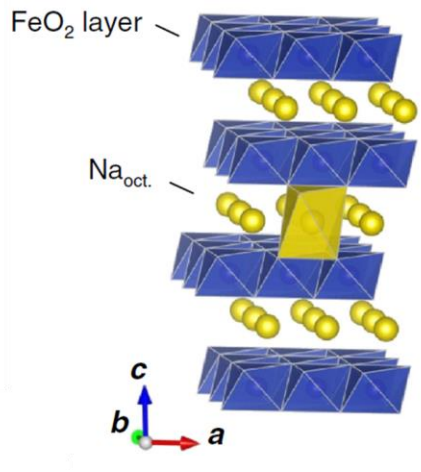

Figure 1.5. Crystal structure of O3-type $NaFeO_2$.Taken from reference 31 with permission of J. Electrochem. Soc.

The electrochemical performance of O3-type $NaFeO_2$ (α-$NaFeO_2$) can deliver 80-100 $mAhg^{-1}$ of reversible capacity, with around 0.3 sodium ions per mole reversibly extracted and intercalated and a nearly flat voltage profile at approximately 3.3 V *vs* Na/Na^+. It has been observed that the electrode performance can deteriorate significantly due to an oxidation process when $x > 0.5$ in $Na_{1-x}FeO_2$. In particular, this loss of electrode reversibility is due to irreversible structural change and iron ion migration in layered host structures. The sodium ion insertion into the host structures

would be disturbed by the irreversible structural change when charging $Na_{1-x}FeO_2$ (x > 0.5) with a voltage higher than 3.4 V. Therefore, this material shows good electrochemistry properties only in the limited composition of x = 0-0.45 in $Na_{1-x}FeO_2$. In addition, it has been reported that the reversibility of electrode material is significantly influenced by the cut-off conditions upon charge (sodium extraction) process. Indeed, the charging capacity, corresponding to the amount of sodium extracted from the crystal lattice, increases as a function of the cut-off voltage and the reversible capacity decreases when the system is charged beyond 3.5 V. The cut-off voltage of 3.4 V instead leads to excellent reversibility equal to 80 $mAhg^{-1}$ and 0.3 mole of sodium extracted from the crystal structure (Figure 1.6a).[31,34] Studies involving charging to different voltages of 3.4-4.5 V and discharge to 2.5 V with a rate of 12.1 mAg^{-1} have been reported and show good capacity retention. The initial reversible capacity is equal to 80 $mAhg^{-1}$ when the cut-off voltage is limited to 3.4 V, suggesting good capacity retention. Indeed, the reversibility capacity retention is equal to 60 $mAhg^{-1}$ after 30 charge and discharge cycles (Figure 1.6b).[31,34]

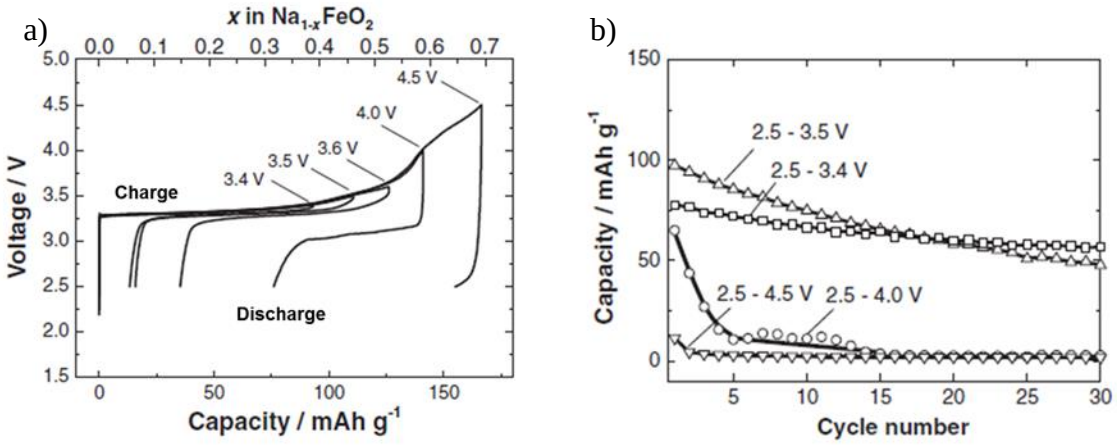

Figure 1.6. a) Charge and discharge curves for $Na_{1-x}FeO_2$ with the different cut-off voltage at a rate of 12 $mAhg^{-1}$ and b) comparison of the discharge capacity retention for 30 cycles. Taken from reference 31 with permission of J. Electrochem. Soc.

Na_xMnO_2 compounds

$NaMnO_2$ is another layered sodium transition-metal oxide that shows interesting electrochemical properties. Two phases exist for $NaMnO_2$, one at low temperature (173 K) called α-$NaMnO_2$, with the O3-type layered structure and a monoclinic structural distortion due to the Jahn-Teller distortion of the Mn^{3+} ion, and one at room temperature called β-$NaMnO_2$, a phase with an orthorhombic crystal structure. This structure contains different layers of MnO_2 sheets, with a double stack of edge-sharing MnO_6 octahedra and sodium ions in the octahedral sites between two neighbouring sheets.[35,36]

The α-$NaMnO_2$ has good electrochemical properties, with 0.8 sodium ions able to be reversibly extracted and intercalated in the structure. The galvanostatic cycling between 2.0 V and 3.8 V for the first cycle shows a discharge capacity at 185 $mAhg^{-1}$, while the discharge capacity after 20 cycles is 132 $mAhg^{-1}$ with the battery completely discharged over a period of 10 hours (C/10). The voltage profile reported in Figure 1.7 shows the

charge and discharge curves upon sodium de-intercalation and intercalation when the cell is charged up to 3.8 V vs Na/Na^+ and discharged to 2.0 V. The amount of sodium that can be de-intercalated from the crystal structure is equal to 0.85 Na and 0.8 Na can be reversibly intercalated back upon discharge to 2.0 V. The charge and discharge curves are significantly different suggesting that the performance of this material is affected by a hysteresis process (Figure 1.7a).[35-38] In the first and tenth galvanostatic cycle at C/10 (1C=240 $mAhg^{-1}$) the coulombic efficiencies are low meaning that side reactions involving the electrolyte can take place also during the charge process (Figure 1.7b).[35-38]

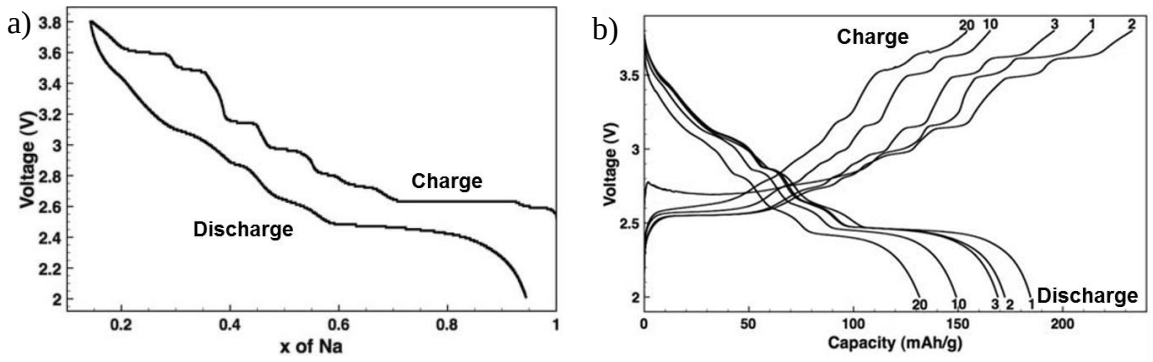

Figure 1.7. Voltage profiles of Na_xMnO_2 a) upon sodium extraction and intercalation and b) after multiple cycles at C/10. Taken from reference 36 with permission of J. Solid State Chem.

In comparison, β-$NaMnO_2$ has a different layered structure than conventionally adopted by $NaMnO_2$ type compounds. In this structure no planar layers of MnO_6 octahedra are observed, as previously noted in α-$NaMnO_2$, instead the layers of edge-sharing MnO_6 octahedra are in a zig-zag conformation with sodium ions in octahedral sites (Figure 1.8).[39]

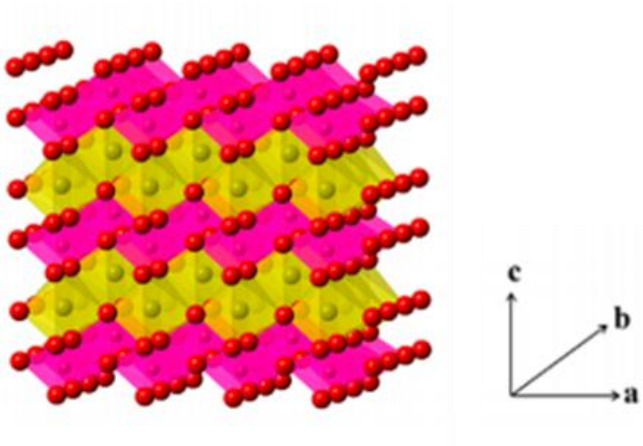

Figure 1.8. Schematic representation of β-$NaMnO_2$ in the Pmnm space group; MnO_6 octahedra in pink, NaO_6 octahedra in yellow, oxygen atoms in red. Taken from reference 39 with permission of J. Am. Chem. Soc.

The β-$NaMnO_2$ compound shows a reversible extraction of 0.15 sodium ions and a potential of 2.7 V *vs* Na^+/Na. The first discharge capacity (equal to the capacity to electrochemically reinsert sodium in the material) for this material is up to 190 $mAhg^{-1}$, which corresponds to 0.82 sodium ions reinserted in the structure per formula unit. After 100 cycles, the discharge capacity is around 130 $mAhg^{-1}$ (Figure 1.9, 1.10). [35,39]

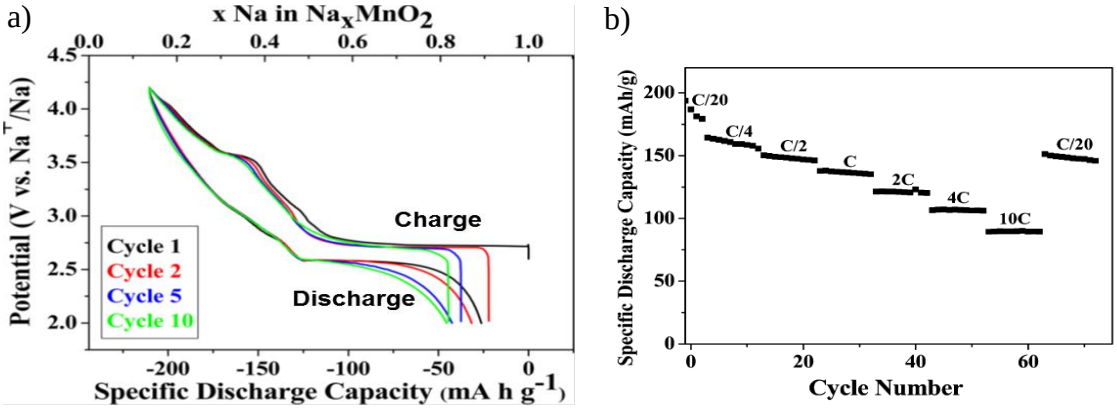

Figure 1.9. Electrochemical data for β-$NaMnO_2$ a) Load curves at a rate of C/20 (10 $mAhg^{-1}$). b) Cycling data obtained between 2.0 and 4.2 V *vs* Na^+/Na at various rates and at room temperature. Sodium extraction was performed at a rate of C/4. Sodium intercalation was performed at the rate indicated on top of each set of data. For data acquired at C/20, both extraction and intercalation are showed. Taken from reference 39 with permission of J. Am. Chem. Soc.

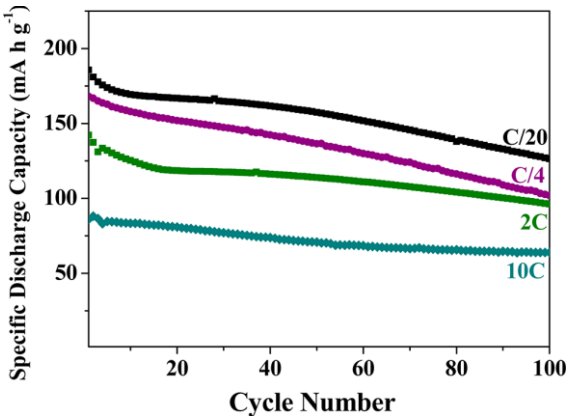

Figure 1.10. Discharge capacities for β-$NaMnO_2$ cycled between 2 and 4.2 V *vs* Na^+/Na at room temperature and at different rates. One hundred cycles are presented for each rate. Taken from reference 39 with permission of J. Am. Chem. Soc.

MoO_3 compounds

Another interesting type of layered oxide cathode material is represented by the molybdenum oxide (MoO_3), which has been proposed as a cathode material since the 1970s.[12,40,41] This oxide is present in nature in three polymorphs. The most stable polymorph is the layered orthorhombic structure (α-MoO_3), which is characterised by the MoO_6 octahedron as the basic structural unit and by a double sheet of MoO_6 octahedra (Figure 1.11a).[41] The second polymorph of this oxide is represented by β-MoO_3. This polymorph has a perovskite-like structure (general formula ABO_3) in which the *A* site is vacant and so can give the possibility for the intercalation of small ions for battery systems (Figure 1.11b).[42] The third polymorph of MoO_3 is hexagonal, which has been reported only as a product of the oxidative extraction and intercalation of the hydronium material, $(H_3O)_xMoO_3 \cdot nH_2O$ (Figure 1.11c).[43,44]

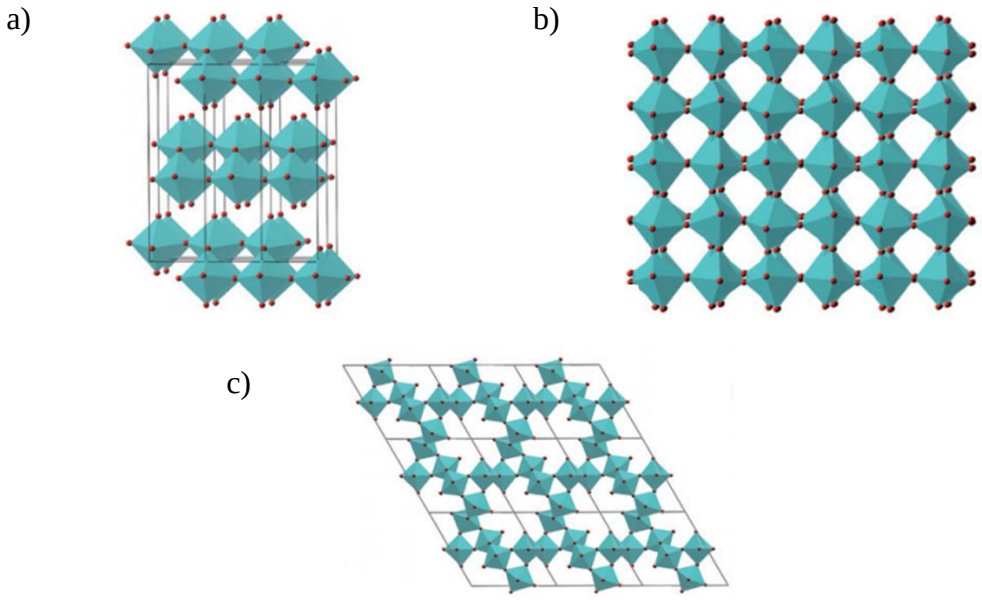

Figure 1.11. Polymorphs of molybdenum trioxide: a) layered α-MoO_3, (b) perovskite-like β-MoO_3, (c) hexagonal *h*-MoO_3. Taken from reference 44 with permission of J. Mater. Chem.

All these polymorphs of MoO_3 show crystal structures with open channels that can favour the intercalation and extraction/intercalation of ions, and for this reason they have been deeply studied in the past as cathode materials for batteries.[12]

1.3.2. Sodium transition-metal polyanionic framework compounds

In a wider context, polyanionic framework compounds are a more general class of 3D materials based on polyanionic polyhedral motifs (XO_4 or XO_3) that are often combined with MO_6 octahedral metals.[46-71]

The compounds characterised by the general formula $Na_xM^{III}_2(XO_4)_3$ or $M^{IV}_2(XO_4)_3$ with X = P, S, W, also known as NASICON, are among the first materials studied in this field and have received more attention as battery materials in recent years.[46-55]

When M is a transition-metal, these types of material can offer open-framework structures with many interstitial spaces to allow insertion of sodium ions. In particular, the availability of low-energy sodium ion migration pathways and the robust covalent frameworks can result in an increased stability at high temperatures and at high charging voltages. For these reasons, these compounds have been deeply explored as cathode materials for the development of the second generation of sodium batteries.[46-71]

Phosphates

$NaFePO_4$ is one of the most representative structures in sodium battery materials (Figure 1.12). This shows a very good thermal stability due to the strong covalent P-O bonds in the $(PO_4)^{3-}$ polyanionic groups and a voltage of 3.45 V with a good electrochemical stability.[46]

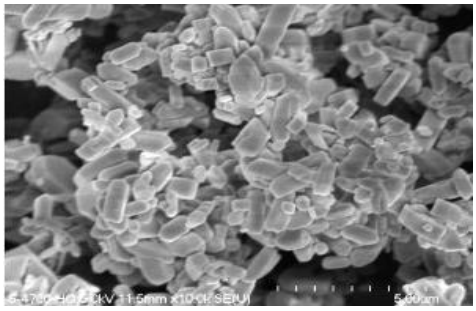

Figure 1.12. SEM picture of $NaFePO_4$. Taken from reference 46 with permission of Chem. Mater.

The most stable version of $NaFePO_4$ is the matricite structure that is electrochemically inactive due to the absence of free pathways for the movement of sodium ions (Figure 1.13a).[46,47]

The olivine type of $NaFePO_4$, is metastable and electrochemically active and its electrochemical profile shows an intermediate phase, $Na_{0.7}FePO_4$ (Figure 1.13b). [46,47]

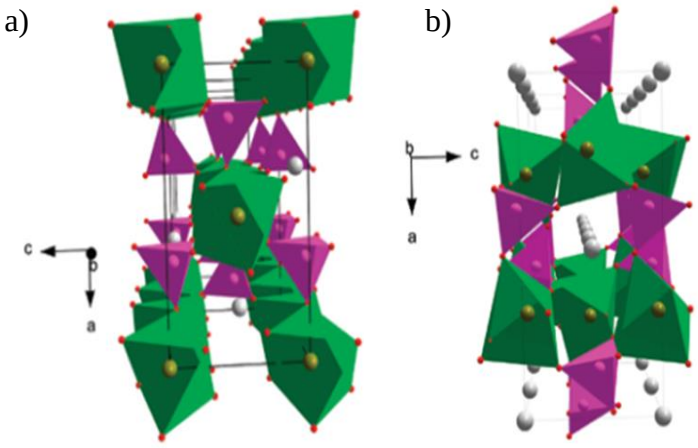

Figure 1.13. Structures of a) matricite $NaFePO_4$ b) olivine $NaFePO_4$; iron in yellow, phosphorus in pink, sodium in grey, oxygen in red. Taken from reference 47 with permission of Chem. Mater.

One of the most interesting NASICON compound is $Na_3V_2(PO_4)_3$ which shows a very high energy density of 400 $Whkg^{-1}$ and a good thermal stability during charge and discharge. Looking at its electrochemical profile, two voltage plateaus has been reported with the first at 3.4 V corresponding to the V^{3+}/V^{4+} redox couple, whereas the second plateau at 1.6 V corresponds to the V^{2+}/V^{3+} redox couple. [2,48]

Fluorophosphates

Fluorine based materials have an important role in materials used for energy and storage applications. Indeed, the presence of fluorine, increases the structure stability and the electrochemical behaviour of battery systems due to the high electronegativity and high free energy of formation of fluorides. The high electronegativity of fluorine and its inclusion in covalent polyanionic frameworks lead to the formation of fluoride structures with octahedral $[M^{n+}F_6]^{(6-n)-}$ units. If the metal-fluorine ratio is less than 6, the octahedral units are linked together through common vertices, edges or faces. In this way the electroneutrality is established and the metal can be at a lower oxidation state. In this way, a variety of 1D chain, 2D net, and 3D framework structures can be formed and be of interest for battery systems.[49]

An interesting fluorophosphate compound is Na_2FePO_4F, showing a two-dimensional framework of $Fe_2O_7F_2$ bioctahedra connected by PO_4 tetrahedra and hosting two sodium ions in the interlayer space (Figure 1.14).[50-52]

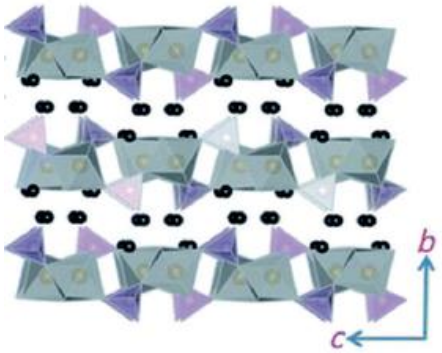

Figure 1.14. Na_2FePO_4F structure. FeO_6 octahedra in grey, PO_4 tetrahedra in pink, and sodium ions in black. Taken from reference 2 with permission of Angew. Chem. Int. Ed.

The electrochemical profile of Na_2FePO_4F shows two-phase plateaux at 2.90 V and 3.05 V *vs* Na/Na^+ for both the charge and discharge profiles with an achievable capacity of 96 $mAhg^{-1}$ (theoretical capacity: 120 $mAhg^{-1}$) (Figure 1.15).[2,50-52]

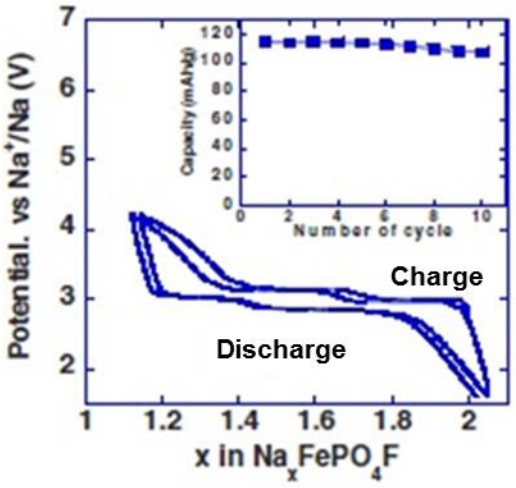

Figure 1.15. Electrochemical profile of Na_2FePO_4F. Taken from reference 2 with permission of Angew. Chem. Int. Ed.

Despite the excellent mobility of sodium ions in this structure, the electrochemical profiles of Na_2FePO_4F are not comparable to what was reported for related vanadium

compounds with a layered structure formed by $V^{4+}O_5F$ and $V^{3+}O_4F_2$ octhahedra and PO_4 tetrahedra.[2,53] In particular, $NaVPO_4F$ shows a reversible capacity of 80 $mAhg^{-1}$ and an average discharge voltage of 3.7 V.[54] Recently, a novel vanadium compound of formula $Na_{1.5}VPO_{4.8}F_{0.7}$ has been reported (Figure 1.16).[53]

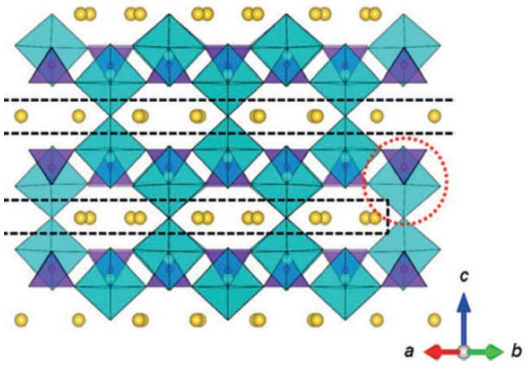

Figure 1.16. $Na_{1.5}VPO_{4.8}F_{0.7}$ structure. Vanadium octahedra in green, PO_4 tetrahedra in purple, sodium ions in yellow. Taken from reference 2 with permission of Angew. Chem. Int. Ed.

The electrochemical tests performed on this material show redox potential of 3.8 V *vs* Na^+/Na of redox potential and a capacity retention of 95% after 100 cycles (85% after 500 cycles) at a rate of 1 C. This material shows high stability during the charge and discharge process, with only 2.9% volume change (Figure 1.17).[53]

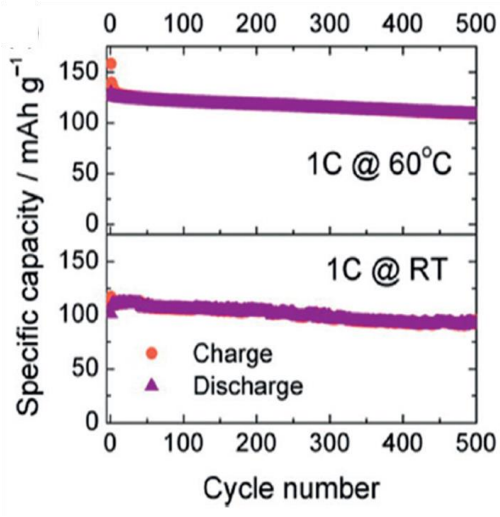

Figure 1.17. $Na_{1.5}VPO_{4.8}F_{0.7}$ electrochemical data at 60 °C (top) and at 25 °C (bottom) at 1C rate and 2-4.7 V. Taken from reference 2 with permission of Angew. Chem. Int. Ed.

An analogue NASICON structure occurs for the compound of formula $Na_3V_2(PO_4)_2F_3$, which shows an average voltage of 3.9 V and a capacity of 111.5 $mAhg^{-1}$ (Figures 1.18-1.19-1.20).[55]

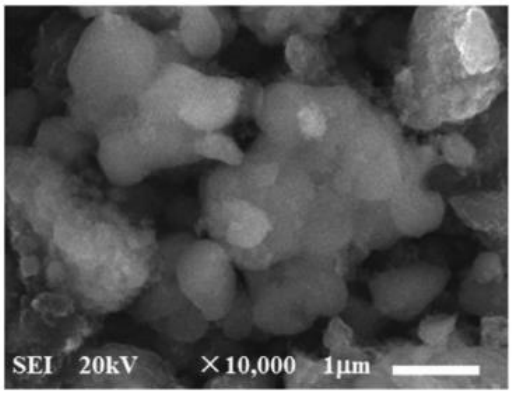

Figure 1.18. SEM picture of $Na_3V_2(PO_4)_2F_3$. Taken from reference 55 with permission of RSC. Adv.

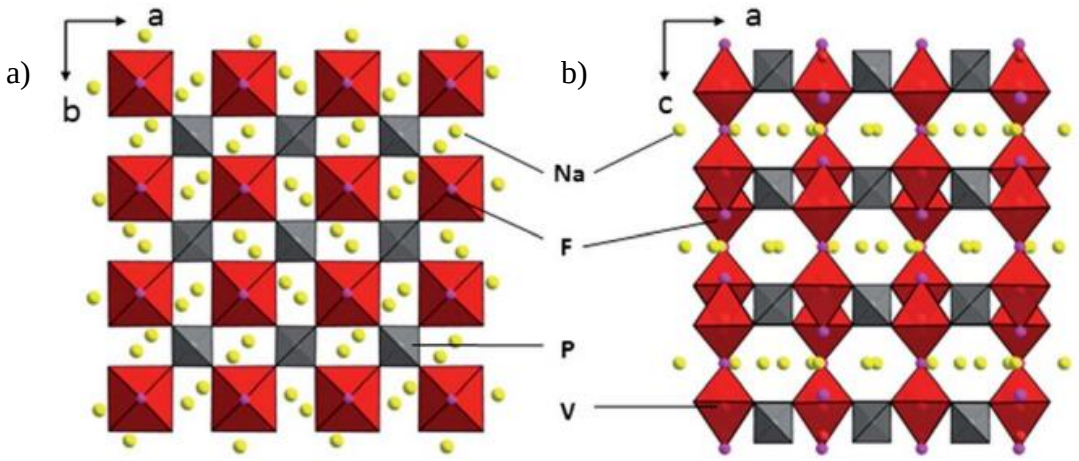

Figure 1.19. $Na_3V_2(PO_4)_2F_3$ structure along a) the *c*-axis and b) the *b*-axis; vanadium octahedra in red, PO_4 tetrahedra in grey, sodium ions in yellow, oxygen in red. Taken from reference 55 with permission of RSC. Adv.

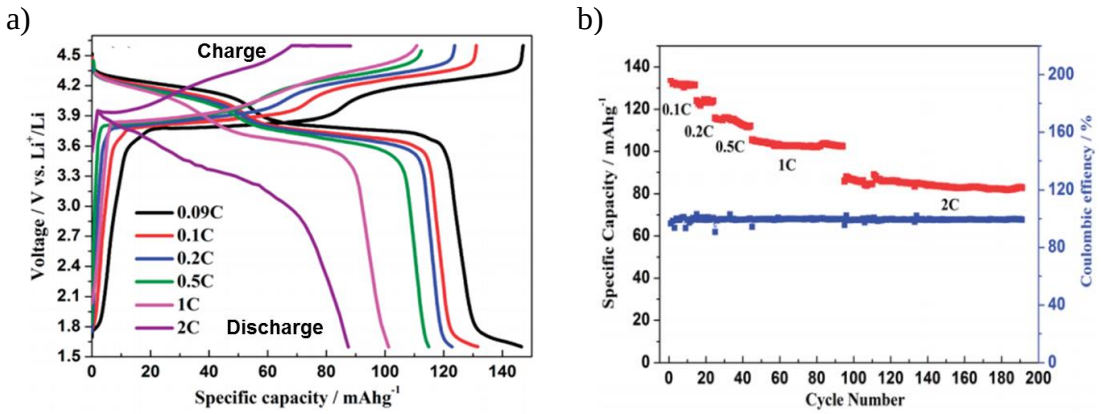

Figure 1.20. $Na_3V_2(PO_4)_2F_3$ electrochemical data: a) charge/discharge profiles at different current densities b) the C-rate and cycling performances. Taken from reference 55 with permission of RSC Adv.

Pyrophosphates

A series of sodium pyrophosphate compounds have been reported.[56-61] $Na_2FeP_2O_7$ shows a reversible capacity of 82 $mAhg^{-1}$ within a potential window of 2.0-4.0 V, an

average voltage of 3 V, a good thermal stability, together with a phase transition occurring during the extraction of sodium ions that results in the formation of $NaFeP_2O_7$ (Figure 1.21).[56]

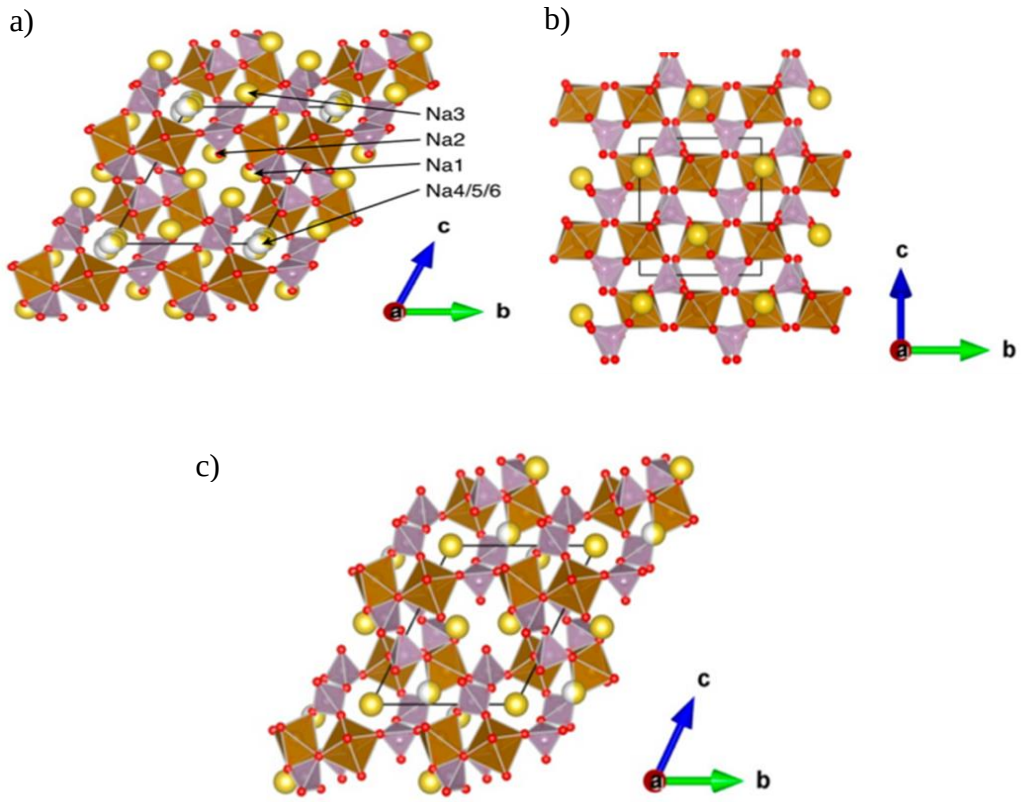

Figure 1.21. Crystal structure of a) $Na_2FeP_2O_7$, b) α-$NaFeP_2O_7$, c) β-$NaFeP_2O_7$; FeO_6 octahedra in orange, PO_4 tetrahedra in grey, sodium ions in yellow, oxygen in red. Taken from reference 56 with permission of Chem. Mater.

Other interesting pyrophosphate compounds are $Na_2MnP_2O_7$ and β-$Na_2MnP_2O_7$,[57] showing 3D channels, a discharge capacity of 80 mAh g^{-1} at a rate of C/20 and 3.6 V redox potential, and $Na_2CoP_2O_7$,[58] showing a layered orthorhombic structure with 2D channels available for sodium ion intercalation, delivering a reversible capacity close to 80 $mAhg^{-1}$ with an average potential of 3 V (Figure 1.22).

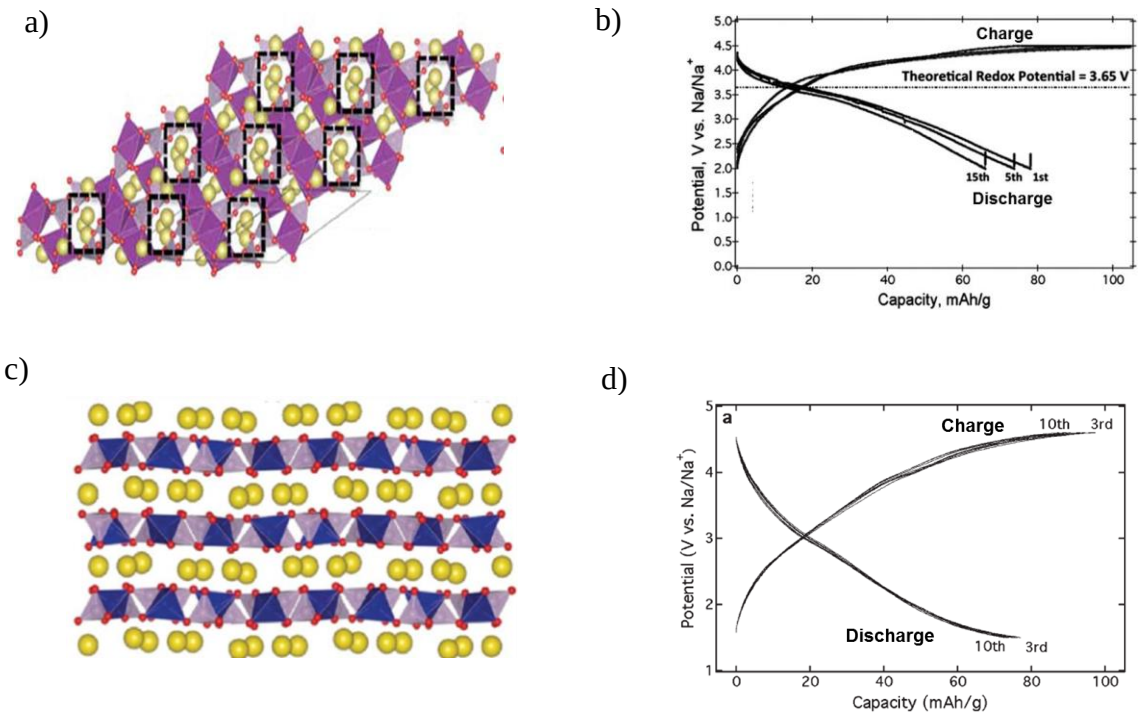

Figure 1.22. a) Crystal structure of β-$Na_2MnP_2O_7$ projected along the *a*-axis with MnO_6 octahedra in pink, PO_4 tetrahedra in light purple and Na atoms in yellow and b) its electrochemical profile; c) Crystal structure of $Na_2CoP_2O_7$ projected along the *c*-axis; CoO_4 tetrahedra in blue, PO_4 tetrahedra in light grey, Na atoms in yellow; d) electrochemical profile of $Na_2CoP_2O_7$. Taken from references 57 and 58 with permission of J. Mater. Chem. And RSC Adv.

An unusual mixed polyphosphate and pyrophosphate cathode material of formula $Na_4Fe_3(PO_4)_2(P_2O_7)$ has also been reported. This material delivers an energy density of 380 $Whkg^{-1}$; three sodium ions are extracted from this structure during the charging process with a small change in volume (4%). The presence of both phosphate and pyrophosphate groups resulted in an increased stability for this structure.[59-61]

Phosphites

The difference in the oxidation state of the phosphorous atom, a lower number of oxygens and a lower charge may lead to new materials for sodium batteries. Studies of transition-metal phosphites have indicated that interesting and novel structures can be produced using hydrothermal methods, including structures containing channels and cavities, particularly interesting for the intercalation and extraction of sodium ions for electrochemical purposes.[62] Barpanda and co-workers have studied the electrochemical properties of $NaFe(PO_3)_3$ for the first time, reporting a reversible capacity above 30 $mAhg^{-1}$ with a redox potential of 3.1 V *vs* Na/Na^+ (Figure 1.23).[63,64]

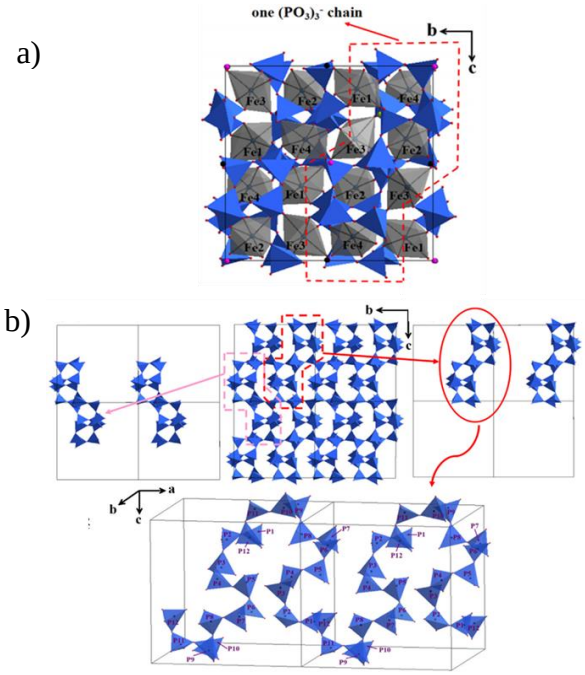

Figure 1.23. a) Structure of $NaFe(PO_3)_3$ with FeO_6 octahedra in blue and PO_4 tetrahedra in grey; b) view of the $NaFe(PO_3)_3$ structure where only PO_4 tetrahedra in blue are shown and Na and Fe atoms are omitted. Taken from reference 64 with permission of Materials Science and Engineering B.

Liu and co-workers have synthesized a polyphosphate $NaFe(PO_3)_3$ compound containing $(PO_3)^{1-}$ chains connected by FeO_6 octahedra and monovalent sodium ions located in the tunnels determined by the connection of PO_4 tetrahedra and FeO_6 octahedra. Only partial reversible discharge capacity could be obtained with less than 0.10 sodium ions per formula unit over the voltage range of 1.5-3.9 V (Figure 1.24).[64]

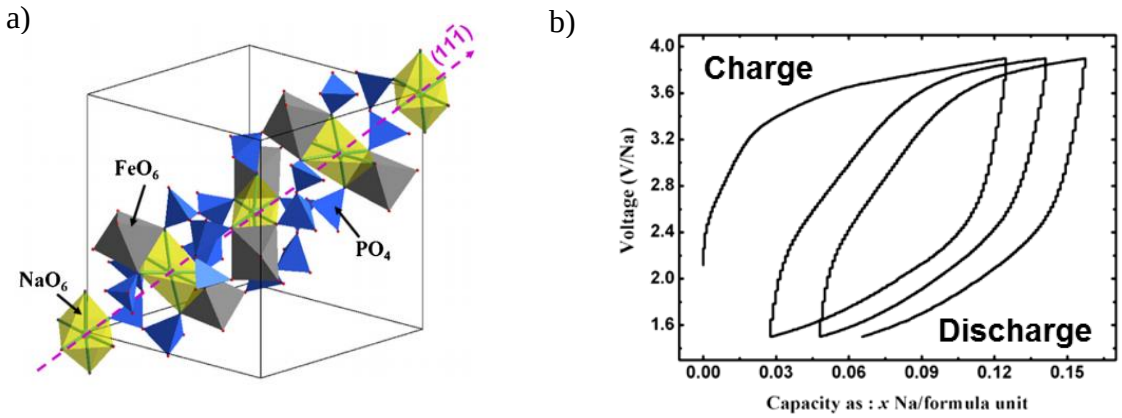

Figure 1.24. a) The typical sodium ion diffusion path in $NaFe(PO_3)_3$ structure along the [1 1 1] direction, FeO_6 octahedra in grey, PO_4 tetrahedra in blue, NaO_6 octahedra in yellow; b) Electrochemical profile for $NaFe(PO_3)_3$ with the current density corresponding to a extraction/insertion of 1 sodium ion per formula unit for 40 h. Taken from reference 64 with permission of Materials Science and Engineering B.

Fluorosulfates and sulfates

Sulfates and fluorosulfates, displaying a tavorite framework structure, are interesting types of polyanionic material in terms of inductive effect they can provide to the whole structure. In particular, they can lead to an increase of 0.8 V as starting contribution to the potential of the material, more than reported for their phosphate counterparts (Figure 1.25).[2,65]

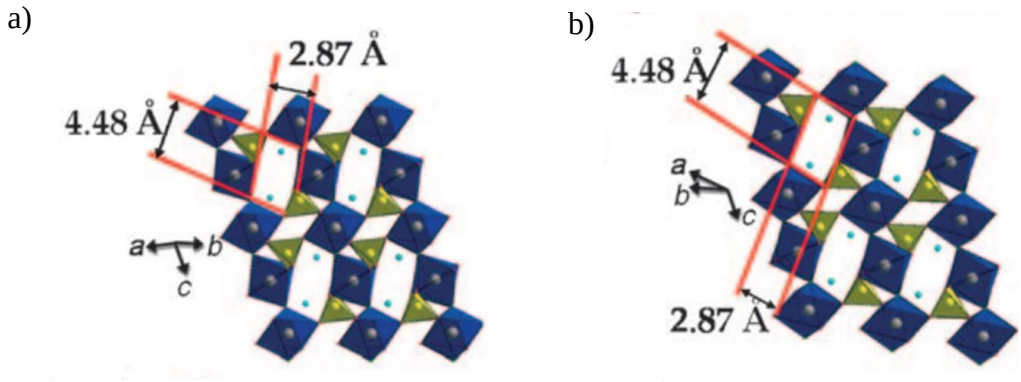

Figure 1.25. a) Structure of $NaFeSO_4F$ along the *a*-axis and b) *b*-axis; two tunnels almost orthogonal to each other are present in the structure. FeO_6 octahedra in blue, SO_4 tetrahedra in yellow, sodium ions in green. Taken from reference 67 with permission of Angew. Chem. Int. Ed.

$NaFeSO_4F$ shows a limited ion mobility and large volume change during the charge and discharge process, resulting in poor electrochemical properties. In particular, only 6% of the theoretical capacity (137 $mAhg^{-1}$) has been achieved with a Fe^{2+}/Fe^{3+} plateau centred around 3.6 V (Figure 1.26).[2,66-68]

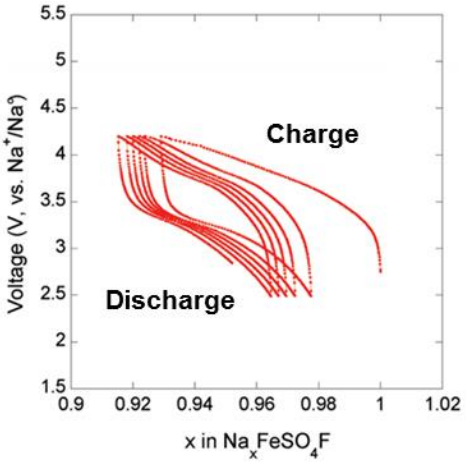

Figure 1.26. Electrochemical charge–discharge profiles for $NaFeSO_4F$ at C/20. Taken from reference 68 with permission of Inorg. Chem.

The structures of $Na_2M(SO_4)_2 \cdot 4H_2O$ and $Na_2M(SO_4)_2 \cdot 2H_2O$ (M = Mg, Fe, Co, Ni) have been reported and explored as cathode materials for sodium batteries.[69,70] Only $Na_2Fe(SO_4)_2 \cdot 4H_2O$ and its dehydrated derivative are electrochemically active materials, which show potentials up to 3.3 V *vs* Na/Na^+. The loss of water during the extraction of sodium ions leads to the formation of an amorphous structure during the charge process. In contrast, the dihydrate version $Na_2Fe(SO_4)_2 \cdot 2H_2O$ show a potential of 3.25 V with good structural reversibility (Figure 1.27).[69,70]

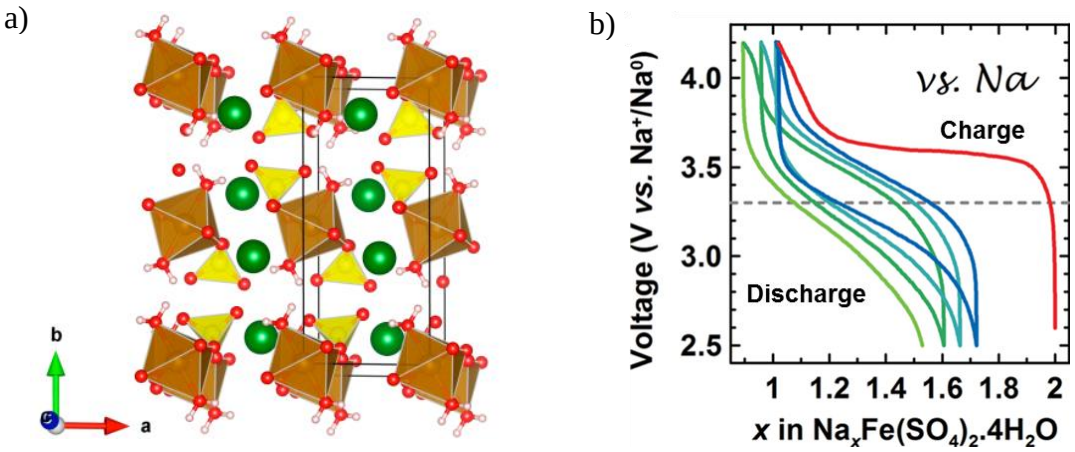

Figure 1.27. a) Structure of $Na_2Fe(SO_4)_2 \cdot 2H_2O$. FeO_6 octahedra in brown, SO_4 tetrahedra in yellow, sodium ions in green, oxygen atoms in red; b) Electrochemical charge and discharge profiles for $Na_2Fe(SO_4)_2 \cdot 4H_2O$. The shift to the left suggests a progressive solvent decomposition upon charging. Taken from reference 69 and 70 with permission of J. Mater. Chem. and Nat. Commun.

Also reported in the literature is an alluaudite framework for the compound $Na_2Fe_2(SO_4)_3$, showing a redox potential of 3.8 V *vs* Na/Na^+, a capacity of 102 $mAhg^{-1}$ (85% of the theoretical value) and a small change in volume during the charge and discharge process (1.6%) (Figure 1.28).[71]

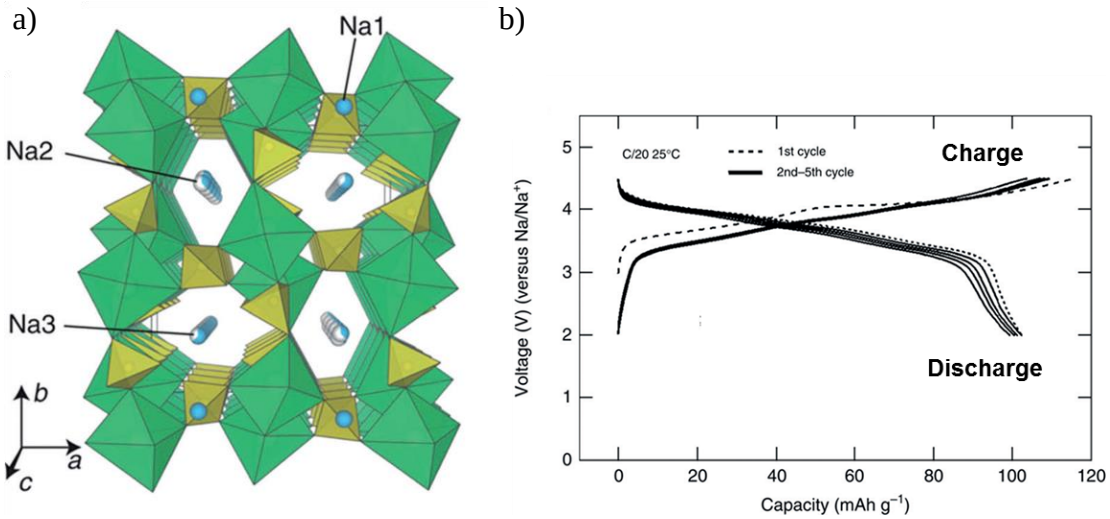

Figure 1.28. a) Structure of $Na_2Fe_2(SO_4)_3$. FeO_6 octahedra in green, SO_4 tetrahedra in yellow, sodium ions in blue; b) Electrochemical charge and discharge profiles for $Na_2Fe_2(SO_4)_3$ cycled at a C/20 rate against sodium. Taken from reference 2 with permission of Angew. Chem. Int. Ed.

1.4 Anode materials for sodium ion batteries

In order to achieve good performance, a battery depends on the safety and efficiency of the anode used in the tests. One of the most common anode material used for testing sodium batteries has been sodium metal. However, for safety issues related to commercial applications, new safer anodes materials have been developed.

1.4.1 Carbons

Graphitic carbons have been widely used in battery systems.[18,72,73] However, sodium atoms hardly intercalate in these structures, so new types of carbon anode materials have been developed for testing sodium batteries. In particular, hard carbons prepared by pyrolysis of sucrose are commonly used, hosting sodium atoms in the porosity

generated by the hard carbon and achieving up to 300 $mAhg^{-1}$ of reversible capacity.[18,72,73]

1.4.2 NASICON type hosts, transition-metal oxides and phosphates

These types of materials assure good safety aspects together with high volumetric energy densities.[74-77]

$NaTi_2(PO_4)_3$ shows a NASICON type structure and exhibits observed capacity very close to the theoretical capacity of 133 $mAhg^{-1}$.[74]

O3-type $NaVO_2$ and P2-type $Na_{0.7}VO_2$ are layered vanadium oxides, highly efficient in the reversible intercalation of sodium.[5,75,76] The working potential of 2.5-1.5 V is to deem these as practical anode materials. Good performances have been shown by $Na_{0.66}Li_{0.22}Ti_{0.78}O_2$ with 120 $mAhg^{-1}$ of reversible capacity at C/10, an average voltage of 0.7 V *vs* Na/Na^+ and 75% of retention after 1200 cycles. This material shows a very small change in volume during the charge and discharge process (0.8%).[77]

1.4.3 Alloys

Alloys are known for their high energy densities and low redox potentials. These key features have been deeply investigated as anode materials for sodium batteries. Unfortunately, for sodium batteries they lack high performance as anode materials. In particular, silicon and germanium do not intercalate sodium at room temperature; lead and bismuth show very poor cyclability with large volume expansions.[78,79] Even if it has a quite significant volume expansion, tin is deemed the most promising candidate as anode material for sodium batteries, with a voltage of 0.3 V *vs* Na/Na^+, a capacity of 500 $mAhg^{-1}$ to be compared with the theoretical capacity of 790 $mAhg^{-1}$.[78]

1.5 Electrolytes

The electrolyte has a key role in a battery providing good ionic conductivity.[2] The most important electrolytes for sodium batteries are of non-aqueous type.[2] These materials consist of a sodium salt dissolved in a solution of organic solvent and ionic liquids (ILs). The ionic liquids chosen are organic salts (R^+X^-) mixed with a fraction of sodium salt equivalent (Na^+X^-). Ethylene carbonate (EC) and propylene carbonate (PC) are the main non-aqueous electrolytes used in sodium batteries due to their high dielectric constants, low volatilities and large electrochemical window.[2,80] Ionic liquids, being practically non-flammable, have been deeply studied as electrolytes for sodium batteries in order to avoid safety issues related to high volatility and flammability of organic liquid electrolytes. The main drawback of ILs is the high operating temperature they require due to their high melting points and viscosity.[2]

1.6 Aims of research

Increasing interest in safe, cheap and sustainable battery materials based on transition-metals such as iron and molybdenum and the already known contribution of polyanions to the performance of battery systems have been key inspiring points for this PhD project. In addition, the relative unknown sodium-phosphite cathode materials together with the important role played by fluorine in order to increase the ionicity of the bonds and the redox potentials of the compounds have been the driving force for the synthesis of new cathode materials for second generation sodium batteries. The aims of this PhD project were to explore new polyanion fluoride frameworks based on the phosphite and phosphate groups and on the molybdenum oxyfluoride group in order to investigate

their properties and behaviour as potential cathode materials for second generation sodium batteries.

Characterisation of these materials was performed by Single Crystal X-ray diffraction, Powder X-ray diffraction, Energy-dispersive X-ray spectroscopy (EDS or EDX), Elemental Analysis (EA), Infrared Spectroscopy (IR), Thermogravimetric analysis (TGA), electrochemical and magnetic properties tests, in collaboration with Dr AR Armstrong (University of St Andrews), Dr Lucy Clark (University of St Andrews), Dr Hajime Ishikawa (University of Tokyo), Professor Alexander N. Vasiliev and his research group (Moscow State University).

1.7 References

1. J. M. Tarascon, M. Armand, *Nature*, 2001, **414**, 359.
2. D. Kundu, E. Talaie, V. Duffort, L.F. Nazar, *Angew. Chem. Int. Ed.* 2015, **54**, 2.
3. F. Risacher, B. Fritz, *Aquat. Geochem.*, 2009, **15**, 123.
4. A. Yaksic, J. E. Tilton, *Resour. Policy*, 2009, **34**, 185.
5. S. Fletcher, Bottled Lightning: Superbatteries, Electric Cars and the New Lithium Economy, *Hill and Wang*, New York, 2012.
6. K.Zaghib, J. Trottier, A. Mauger, H. Groult, C.M. Julien, *Int. J. Electrochem. Sci.*, 2013, **8**, 9000.
7. H. Böhm, G. Beyermann, *J. Power Sources*, 1999, **84**, 270.
8. R. C. Galloway, S. Haslam, *J. Power Sources*, 1999, **80**, 164.
9. T. Javadi, A. Petric, *J. Electrochem. Soc.*, 2011, **158**, A700.
10. T. M. O. Sullivan, C. M. Bingham, R. E. Clark, *International Symposium on Power Electronics, Electric Drives, Automation and Motion*, 2006, pp. 34.
11. D. J. L. Brett, P. Aguiar, N. P. Brandon, *J. Power Sources*, 2006, **163**, 514.
12. M. S. Whittingham, *Prog. Solid State Chem.*, 1978, **12**, 41 – 99.
13. A. S. Nagelberg, W. L. Worrell, *J. Solid State Chem.*, 1979, **29**, 345.
14. I. A. Udod, H. B. Orman, V. K. Genchel, *Carbon*, 1994, **32**, 101.
15. M. M. Doeff, Y. Ma, S. J. Visco, L. C. De Jonghe, *J. Electrochem. Soc.*, 1993, **140**, L169.
16. D. A. Stevens, J. R. Dahn, *J. Electrochem. Soc.*, 2000, **147**, 1271.
17. D. A. Stevens, J. R. Dahn, *J. Electrochem. Soc.*, 2001, **148**, A803.
18. S. Komaba, W. Murata, T. Ishikawa, N. Yabuuchi, T. Ozeki, T. Nakayama, A. Ogata, K. Gotoh, K. Fujiwara, *Adv. Funct. Mater.*, 2011, **21**, 3859.

19. R. C. Asher, *J. Inorg. Nucl. Chem.*, 1959, **10**, 238.

20. P. Ge, M. Fouletier, *Solid State Ionics*, 1988, **28 – 30**, 1172.

21. T. Ohzuku, A. Ueda, M. Nagayama, Y. Iwakoshi, H. Komori, *Electrochim. Acta*, 1993, **38**, 1159.

22. K. Ozawa, *Solid State Ionics*, 1994, **69**, 212.

23. R. Yazami, N. Lebrun, M. Bonneau, M. Molteni, *J. Power Sources*, 1995, **54**, 389.

24. T. Ohzuku, Y. Makimura, *Chem. Lett.*, 2001, **8**, 744.

25. R. Berthelot, D. Carlier, C. Delmas, *Nat. Mater.*, 2011, **10**, 74.

26. C. Delmas, J.-J Braconnier,C. Fouassier, P. Hagenmuller, *Solid State Ionics*, 1981, **3−4**, 165.

27. C. Delmas, C. Fouassier, P. Hagenmuller, *Physica B*, 1980, 99.

28. N. Yabuuchi, K. Kubota,M. Dahbi,S. Komaba, *Chem. Rev.*, 2014, **114**, 11636.

29. Z. Lu, J.R. Dahn, *J. Electrochem. Soc.*, 2001, **148**, A710.

30. Z. Lu, J.R. Dahn, *J. Electrochem. Soc.*, 2001, **148**, A1225.

31. N. Yabuuchi, H. Yoshida, S. Komaba, *Electrochemistry*, 2012, **80**, 716719

32. L.W. Shacklette, T.R. Jow, L. Townsend, *J. Electrochem. Soc.*, 1988, **135**, 2669.

33. Y. Lei, X. Li, L. Liu, G. Ceder, *Chem. Mater.*, 2014, **26**, 5288.

34. M.H. Han, E. Gonzalo, G. Singha, T. Rojo, *Energy Environ. Sci.*, 2015, **8**, 81.

35. A. Mendiboure, C. Delmas, P. Hagenmuller, *J. Solid State Chem.*, 1985, **57**, 323.

36. X. Ma, H. Chen, G. Ceder, *J. Electrochem. Soc.*, **158**, 2011, A1307.

37. J.-P. Parant, R. Olazcuaga, M. Devalette, C. Fouassier, *J. Solid State Chem.*, 1971, **3**, 1.

38. O. I. Velikokhatnyi, C.-C. Chang, P. N. Kumta, *J. Electrochem. Soc.*, 2003, **150**, A1262.

39. J. Billaud, R.J. Clément, A.R. Armstrong, J. Canales-Vázquez, P.Rozier, C.P. Grey, P.eter G. Bruce, *J. Am. Chem. Soc.*, 2014, **136**, 17243.

40. L. Campanella, G. Pistoia, *J. Electrochem. Soc.*, 1971, **118**, 1905.

41. J. Margalit, *J. Electrochem. Soc.*, 1974, **121**, 1460.

42. E.M. McCarron, *J. Chem. Soc., Chem. Commun.*, 1986, 336.

43. J.-D. Guo, P. Zavalij, M. S. Whittingham, *J. Solid State Chem.*, 1995, 117.

44. N.A. Chernova, M. Roppolo, A.C. Dillonb, M.S. Whittingham, *J. Mater. Chem.*, 2009, **19**, 2526.

45. F. W. Dampier, *J. Electrochem. Soc.*, 1974, **121**, 656.

46. J. Lu, S. C. Chung, S. Nishimura, A. Yamada, *Chem. Mater.*, 2013, **25**, 4557.

47. P. Moreau, D. Guyomard, J. Gaubicher, F. Boucher, *Chem.Mater.* 2010, **22**, 4126.

48. K. Saravanan, C.W. Mason, A. Rudola, K. H.Wong, P. Balaya, *Adv. Energy Mater.*, 2013, **3**, 444.

49. G. G. Amatucci, N. Pereira, *J. Fluorine Chem.*, 2007, **128**, 243.

50. B. L. Ellis, W. R. M. Makhanouk, Y. Makimura, K. Toughilland, L. F. Nazar, *Nat. Mater.*, 2007, **6**, 749.

51. N. Recham, J.-N. Chotard, L. Dupont, K. Djellab, M. Armand, J-M. Tarascon, *J. Electrochem. Soc.*, 2009, **156**, A993.

52. Y. Kawabe, N. Yabuuchi, M. Kajiyama, N. Fukuhara, T.Inamasu, R. Okuyama, I. Nakai, S. Komaba, *Electrochem. Commun.*, 2011, **13**, 1225.

53. Y. U. Park, D. H. Seo, H. S. Kwon, B. Kim, J. Kim, H. Kim, I. Kim, H. I. Yoo, K. Kang, *J. Am. Chem. Soc.*, 2013, **135**, 13870.

54. J. Barker, M. Y. Saidi, J. L. Swoyer, *Electrochem. Solid- State Lett.*, 2003, **6**, A1.

55. W. Song, X. Ji, Z. Wu, Y. Zhu, F. Li, Y. Yao, C. E. Banks, *RSC. Adv.*, 2014, **4**, 11375.

56. P. Barpanda, G. Liu, C. D. Ling, M. Tamaru, M. Avdeev, S. C.Chung, Y. Yamada, A. Yamada, *Chem. Mater.*, 2013, **25**, 3480.

57. P. Barpanda, T. Ye, M. Avdeev, S. C. Chunga, A. Yamada, *J. Mater. Chem. A*, 2013, **1**, 4194.

58. P. Barpanda, J. Lu, T. Ye, M. Kajiyama, S. C. Chung, N. Yabuuchi, S. Komaba, A. Yamada, *RSC Adv.*, 2013, **3**, 3857.

59. H. Kim, I. Park, D.-H. Seo, S. Lee, S.-W. Kim, W. J. Kwon,Y.-U. Park, C. S. Kim, S. Jeon, K. Kang, *J. Am. Chem. Soc.*, 2012, **134**, 10369.

60. H. Kim, I. Park, S. Lee, H. Kim, K.-Y. Park, Y.-U. Park, H. Kim, J. Kim, H.-D. Lim, W.-S. Yoon and K. Kang, *Chem. Mater.*, 2013, **25**, 3614.

61. L.P. Wang, L. Yu, X. Wang, M. Srinivasan, Z.J. Xu, *J. Mater. Chem. A*, 2015, **3**, 9353.

62. R.E. Morris, M.P Attfield, A.K. Cheetham, Acta Crystallogr. C, 1994, **50**, 473.

63. R. Gond, G. Shinde, P. Barpanda., Abstract MA2016-02 720, ECS Meeting abstracts, 2016.

64. X. Lin, Y. Zhao, Y. Dong, Q. Kuang, Z. Liang, D. Yan, X. Liua, *Materials Science and Engineering B*, 2015, **197**, 58.

65. J. Pizarro-Sanz, J. Dance, G. Villeneuve, M. Arriortua-Marcaida, *Mater. Lett.*, 1994, **18**, 327.

66. R. Tripathi, T. N. Ramesh, B. L. Ellis, L. F. Nazar, *Angew.Chem. Int. Ed.*, 2010, **49**, 8738.

67. R. Tripathi, T. N. Ramesh, B. L. Ellis, L. F. Nazar, *Angew.Chem. Int. Ed.*, 2010, **122**, 8920.

68. P. Barpanda, J.-N. Chotard, N. Recham, C. Delacourt, M. Ati,L. Dupont, M. Armand, J.-M. Tarascon, *Inorg. Chem.*, 2010, **49**, 7401.

69. M. Reynaud, G. Rousse, A. M. Abakumov, M. T. Sougrati, G. V. Tendeloo, J. N. Chotarda, J. M. Tarascon, *J. Mater. Chem.A*, 2014, **2**, 2671.

70. P. Barpanda, G. Oyama, C. D. Ling, A. Yamada, *Chem. Mater.*, 2014, **26**, 1297.

71. P. Barpanda, G. Oyama, S. Nishimura, S. C. Chung, A. Yamada, *Nat. Commun.*, 2014, **5**, 4358.

72. R. C. Asher, *J. Inorg. Nucl. Chem.*, 1959, **10**, 238.

73. P. Ge, M. Fouletier, *Solid State Ionics*, 1988, **28 – 30**, 1172.

74. S. I. Park, I. Gocheva, S. Okada, J. Yamaki, *J. Electrochem. Soc.*, 2011, **158**, A1067.

75. C. Didier, M. Guignard, C. Denage, O. Szajwaj, S. Ito, I. Saadoune, J. Darriet, C. Delmas, *Electrochem. Solid-State Lett.*, 2011, **14**, A75.

76. M. Guignard, C. Didier, J. Darriet, P. Bordet, E. Elka, C. Delmas, *Nat. Mater.*, 2013, **12**, 74.

77. Y. Wang, X. Yu, S. Xu, J. Bai, R. Xiao, Y.-S. Hu, H. Li, X.-Q. Yang, L. Chen, X. Huang, *Nat. Commun.*, 2013, **4**, 2365.

78. S. Komaba, Y. Matsuura, T. Ishikawa, N. Yabuuchi,W. Murata,S. Kuze, *Electrochem. Commun.*, 2012, **21**, 65.

79. L. D. Ellis, B. N. Wilkes, T. D. Hatchard, M. N. Obrovac, *J. Electrochem. Soc.*, 2014, 161, A416.

80. A. Hayashi, K. Noi, A. Sakuda, M. Tatsumisago, *Nat. Commun.*, 2012, **3**, 856.

Chapter 2

Experimental and Characterisation Techniques

2.1 Solvothermal and hydrothermal syntheses

Solvothermal synthesis is a useful method in order to obtain different materials such as semiconductors, ceramic and polymeric materials. It is characterised by the use of a solvent at a temperature above its normal boiling point (typically between 100 °C and 1000 °C) and therefore under pressure (between 1 atm and 10,000 atm), in order to promote enhanced interactions of starting materials under these conditions. When the solvent used is water, the method is named hydrothermal synthesis and in this case the temperature during the synthesis is usually below the supercritical temperature of water (374 °C).[1]

It is possible to prepare materials with different morphologies (films, powders, single crystals and nanocrystals) by modifying the concentration of the solvent, the type of chemicals used and the kinetics of the reaction.

The synthesis involves heating the starting materials in a closed vessel consisting of a steel pressure apparatus known as autoclave (Figure 2.1). The thick stainless steel withstands the high pressures observed during the synthesis and is fitted with safety

valves. The internal part of the autoclave is usually lined with inert materials, such as Teflon (Figure 2.1).

Figure 2.1. Autoclave.

In these processes the autoclave is placed in an oven and heated, so the pressure increases. In the hydrothermal synthesis the water remains liquid above its normal boiling temperature of 100 °C and, for this reason it is called superheated water. The hydrothermal conditions are present when the pressure is above atmospheric pressure. These conditions may be present in nature, and different materials, such as zeolites and gemstones, are made by this process.[1]

Solvothermal and hydrothermal synthesis allow to work at high pressures and with lower temperatures compared to ambient pressure conditions reducing the probability of decomposition of the starting materials. It is possible to synthesise compounds with unusual oxidation states, that are stabilised by the pressure and the temperature produced inside the autoclave, or to stabilise metal oxide systems where the oxides are not soluble in water at ambient conditions but can be solubilised in superheated water.[1]

Many of the compounds synthesised by these routes can crystallise during the reaction, facilitating the identification of phases and crystal structures. Also, the presence of materials in solution increases the rate of reaction to those observed in solid state reactions, thus requiring shorter reaction times. Another advantage of hydrothermal and solvothermal techniques is the possibility to run several reactions by heating the autoclaves simultaneously in the same location allowing a quicker route to investigate synthesis parameters (*i.e.* temperature, pressure and solvent).[1]

The benefits of solvothermal and hydrothermal methods means that these techniques are widely used in a variety of research fields for the synthesis of new compounds with specific physical properties, to investigate difficult multicomponent systems at elevated temperatures and pressures and, at the industrial level, to prepare large crystals (e.g. zeolites and gemstones).[2]

2.2 X-ray diffraction

X-ray diffraction is a powerful technique allowing one to characterise crystalline compounds.[3] X-rays are generated by an electrically heated filament of tungsten that emits electrons accelerated by a high potential difference, between 20 and 50 kV. These electrons strike an anode: a metal target (mostly copper or molybdenum) that is water cooled (Figure 2.2).[3]

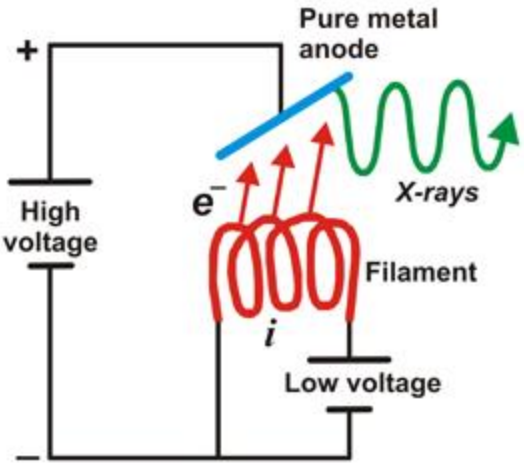

Figure 2.2. X-ray production in a conventional X-ray tube.[3]

These bombarding electrons knock out the core electrons from the anode (K, n=1), creating vacancies, that are then filled with the electrons coming from the higher energy shells (L or M) and the released energy results in a continuous flow of X-rays. In particular, it is possible to distinguish two main sharp and intense X-ray peaks called K_α, produced by electrons descending from the L shell (n=2), and K_β, produced by electrons descending from the M shell (n=3) (Fig 2.3).[3] The position of these X-ray peaks is modified by changing the target material (for example from Cu to Mo), with a shift to shorter wavelength with an increased Z value. K_α and K_β are actually not single peaks, but very closely-spaced doublets, $K_{\alpha1}$- $K_{\alpha2}$ and $K_{\beta1}$- $K_{\beta2}$.[1,3-5]

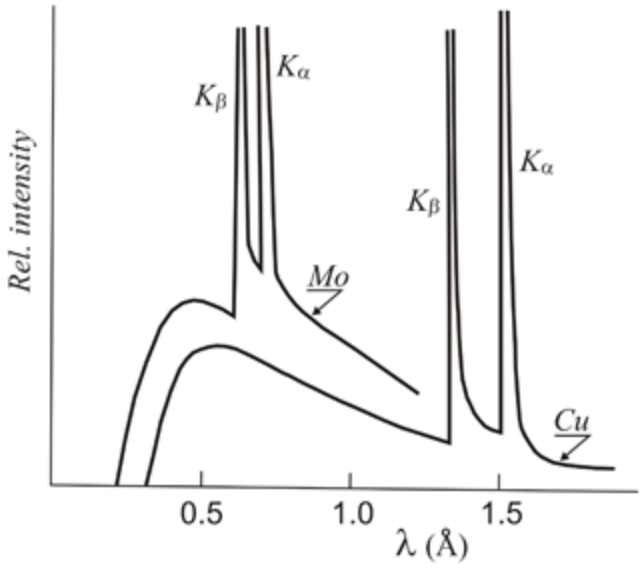

Figure 2.3. Distribution of X-ray wavelengths produced in a conventional X-ray tube where the anode material is copper (Cu) or molybdenum (Mo). The characteristic K-alpha (K_α) and K-beta (K_β) signals are shown.[3]

Crystalline solids are composed of atoms, ions or molecules with interatomic spacing represented by planes. X-rays are scattered by arrays of atoms present inside crystals, making spherical waves scattered from the electrons. This type of phenomenon is known as elastic scattering. When the waves scattered from different atoms meet other waves they can cancel or reinforce each other due to interference effects. Constructive interference can happen only in a few specific directions. In a crystal section, interplanar spacing d_{hkl} separate Miller indices when a parallel beam of monochromatic X-rays occurs. In order to obtain constructive interference, the reflected beams have to reinforce each other (*i.e.* arrive in phase), and so the path lengths of the interfering beams must be different by whole numbers of wavelengths from each other (Figure 2.4, Equation 2.1).

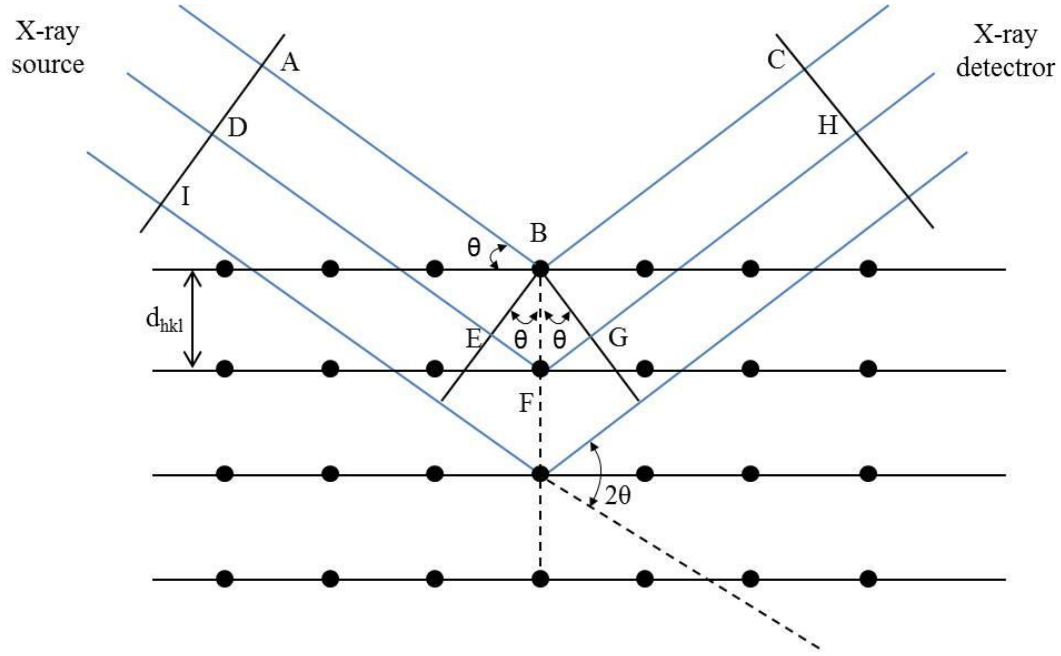

Figure 2.4. The Bragg's law for X-ray diffraction.

In particular,

$$\overline{EF} = \overline{FG} = d_{hkl} sin\theta_{hkl} \qquad \text{Eq. 2.1}$$

The difference in path length must be equal to a whole number of wavelengths (n=1, 2, 3, *etc.*) with λ being the X-ray wavelength:

$$Difference\ in\ path\ length = \overline{EF} + \overline{FG} = 2\, d_{hkl} sin\theta_{hkl} = n\lambda \qquad \text{Eq. 2.2}$$

The incident electromagnetic radiation (X-rays) must possess a wavelength of the same order of magnitude as d (~ 10^{-10} m).

For n=2 and *hkl* the set of planes, then the reflections are of second order and can be described in Equation 2.3:

$$2\lambda = 2\, d_{hkl} \sin\theta_{hkl}$$

$$\lambda = 2\frac{d_{hkl}}{2} \sin\theta_{hkl} \qquad \text{Eq. 2.3}$$

Which is actually equal to a first order reflection (n = 1) with $d_{hkl}/2$ interplanar spacing. This is equivalent to saying that the Miller indices are $2h$, $2k$, $2l$ and the equation becomes equal to:

$$\lambda = 2\, d_{hkl} \sin\theta_{hkl} \qquad \text{Eq. 2.4}$$

In this way it impossible to distinguish between the second order reflection with h, k and l as Miller indices and the first order reflection with $2h$,$2k$,$2l$ as Miller indices.

X-ray diffraction is an established technique for both qualitative and quantitative phase analysis of solids as well as for studying structure and morphology.[1] X-ray diffraction can be performed on both single crystals and polycrystalline (powder) materials.[1] In the case of air-sensitive materials, samples are sealed in a glovebox either between two pieces of polyethylene sheets using vacuum grease or in a glass capillary tubes using non corrosive silicon rubber.

2.2.1 Single crystal X-ray diffraction (SXD)

Single-crystal X-ray diffraction is the first discovered and most precise method used for crystallographic studies.[1]

With this technique it is possible to measure in a very accurate way the intensity and positions of the *hkl* reflections of a single crystal and therefore determine the unit cell dimensions, the space group and the atomic positions. X-rays are scattered by the electrons in the atoms, therefore, the number of electrons that are present in a crystal influences the interaction between the crystal and the X-rays. In particular, the higher the number of electrons in an atom, the more the X-rays will be scattered. How much effective in scattering X-rays an atom is defined by the atomic scattering factor (f_0), which depends not only on the atomic number but also on the Bragg angle (θ) and the wavelength of the X-rays used. The atomic electron distribution has a finite size compared to the X-ray wavelength, so an increase in the scattering angle (θ values) would result in the X-rays scattered by the electrons to be more out-of-phase compared with the ones scattered in another part of the atom, leading to destructive interference (Figure 2.5).

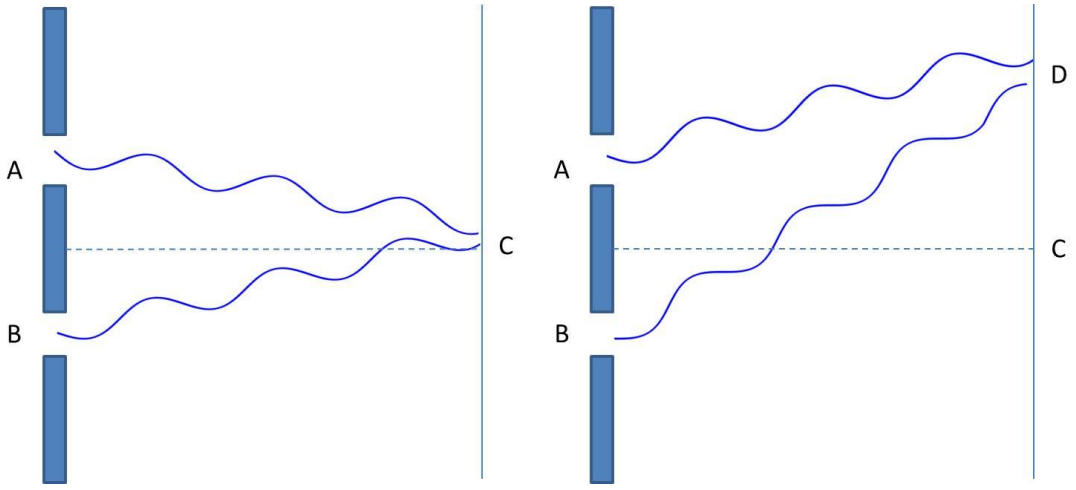

Figure 2.5. Constructive (left) and destructive (right) interference.

The structure factor F_{hkl}, which depends on each atom position and its scattering factor f_0, can be defined by the sum of all the waves scattered by all the atoms in the unit cell

for a particular set of *hkl* planes we can define. For *j* atoms in a unit cell, the structure factor formula can be written as in Equation 2.5.

$$F_{hkl} = \sum_j f_j e^{2\pi i(hx_j + ky_j + lz_j)} \qquad \text{Eq. 2.5}$$

The *fj* is the scattering factor of the j^{th} atom, characterised by x_j, y_j and z_j fractional coordinates. In the case of centrosymmetric crystals, the structure factor equation can be simplified to the Fourier series:

$$F_{hkl} = 2\sum_n f_n cos2\pi(hx_n + ky_n + lz_n) \qquad \text{Eq. 2.6}$$

where *n* is the number of the unique atoms present in the unit cell. Therefore, the diffraction pattern is, in mathematical terms, the Fourier transform of the crystal structure (*i.e.* electron density distribution in the unit cell). What crystallographers aim to determine in the diffraction experiment is to find the electron density distribution from the measured diffraction pattern. This is expressed by modified Fourier transform reported in Equation 2.7.

$$\rho(x,y,z) = \frac{1}{V}\sum_h \sum_k \sum_l F_{hkl} e^{-2\pi i(hx+ky+lz)} \qquad \text{Eq. 2.7}$$

where $\rho(x,y,z)$ is the electron density considering a position (x,y,z) in the unit cell characterised by a volume *V*. Hence, the electron density can be defined as the Fourier

transform of the structure factor and *viceversa*, and the electron density and atomic positions in the unit cell can be calculate when the structure factors are known.

There is also a relationship between the value of *hkl* reflection intensity (I_{hkl}), unique for a particular crystal, and the structure factor. In particular,

$$I_{hkl} \propto {F_{hkl}}^2$$

$$|F_{hkl}| \propto \sqrt{I_{hkl}} \qquad \text{Eq. 2.8}$$

the structure factor and the intensity depend on the atom position and its scattering factor, and they can be calculated using the Equations 2.5 or 2.6, knowing the types and the positions of the atoms. The reverse of this calculation is possible but, because the modulus of the structure factor can be obtained only from the square root of the intensity, it is possible to know only the magnitude but not the sign of the structure factor. This means that the information related to the phase of F_{hkl} is lost and, therefore, the electron density distribution cannot be calculated and so the atomic positions. Nowadays, the solution of this issue, known as phase problem, has become a routine, by using statistical methods, so it is generally straightforward to obtain reliable crystal structures from good quality single crystal X-ray diffraction data.

SXD instrumentation and Data collection

An X-ray diffractometer is composed by three main elements: the X-ray tube, where the X-rays are generated, the sample holder and the X-ray detector (Figure 2.6). The generation of X-rays is a very inefficient process. The vast majority of the power used in generating X-rays results in the collision of accelerated electrons with valence

electrons of the target material producing heat. A small fraction of the energy applied to the tube actually produces the characteristic radiation used in diffraction experiments.

There are two types of X-ray tube configurations. The first type is a sealed-tube X-ray generators using a stationary anode. The power that can be applied to these tubes is limited by the amount of heat that can be dissipated through the water cooling system. In order to increase the heat dissipation, and therefore increase the X-ray beam intensity, rotating anode X-ray tubes can be used. In these tubes the anode is rotated in order to have the beam of electrons continually hitting a new region of the anode. These rotating anode generators are more efficient than the sealed tube generators and for this reason they are the most commonly used in modern instruments. However, rotating anode generators require a considerable amount of maintenance in order to replace filaments, repair/replace the anode, the vacuum and the water systems. The filament is subjected to high temperature and, in order to avoid burning, it needs to be kept under high vacuum conditions, and the anode, with its constant flow of cooling water, needs to be rotated continuously at speeds of 6000 rpm or more. On the other hand, sealed tube systems need minimal maintenance and are often used for intense beams and routine small molecule investigation.

The filament is usually made of tungsten and the most common target materials used for single crystal X-ray diffraction are molybdenum, with K_α radiation ~ 0.71 Å, and copper, with K_α radiation ~ 1.54 Å. The X-rays produced in this way are collimated and directed onto the sample, being afterwards detected and converted in X-ray signal by the detector.

Another way to produce X-rays is by using a synchrotron, which is more powerful and is able to produce and emit a much stronger beam. Synchrotrons produce polychromatic beams with high energy, and therefore short wavelength. Very high resolution can be achieved by judicious collimation of the beam.

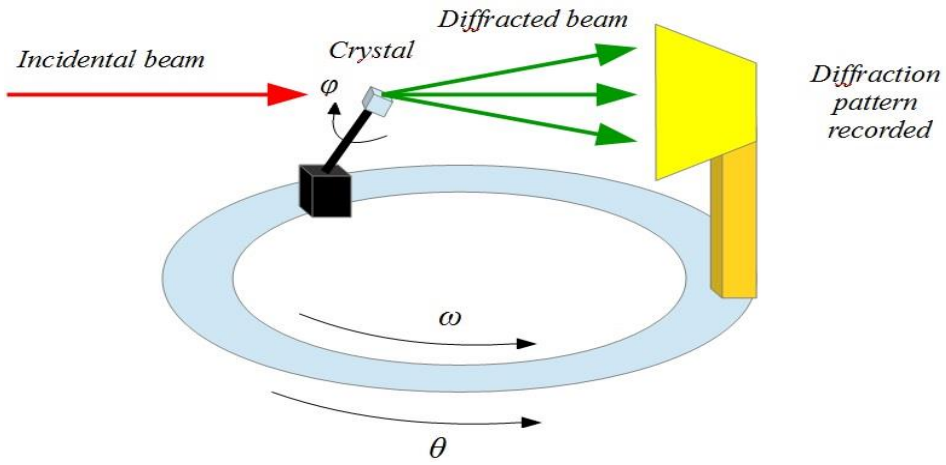

Figure 2.6. Single crystal X-ray diffraction measurement.

In order to obtain a good dataset of reflections it is important to isolate an adequate crystal of the material under study. In particular the crystal should be sufficiently large (typically larger than 0.01 mm in all three dimensions), pure in composition and regular in structure, with no significant internal imperfections such as cracks or twinning.

After mounting and centring the crystal on a goniometer, the sample quality is determined by a preliminary rotation of the sample. If this qualitative check is successful, then it is possible to set the diffractometer in order to obtain an automatic rotation of the sample in all three dimensions and collect data about the unit cell. Different rotations give different 2D pictures, which are converted into a 3D model of electron density using the Fourier transform techniques and a chemical knowledge of the sample.

All single crystal data reported in this PhD thesis were collected using a Rigaku SCX mini desktop diffractometer and a Rigaku Mercury CCD diffractometer both in-house facilities. These two diffractometers are equipped with graphite monochromated Mo K_α radiation and area detectors to speed up data collection times through collection of multiple diffraction intensities in a single image scan. In order to improve data quality, the Rigaku SCX mini desktop diffractometer collects all images twice to help minimise any undesired reflections. Firstly, six image frames are collected in order to check both the diffraction quality and intensity of the crystal scattering and to calculate approximate unit cell parameters. This step is also useful in order to ensure the correct orientation of the crystal with respect to the beam and to determine an adequate scan time to produce spots with sufficient intensity before starting the full data collection.

When the full dataset has been collected, it is then integrated into a 3D model of related spots, that can be described as reflections with *hkl* values assigned to each set of related spots in the pattern. These values can be used to identify systematic absences and to assign a space group to the crystal structure.

By using a series of complex calculations, it is possible to obtain a 3D map of the electron density and therefore information related to the atom types and their position. In this way, it is possible to overcome the loss of phase information typical of the physical measurement process known as the phase problem.

Data analysis and results

The determination of the crystal structure can be difficult for large and complex unit cell. In fact, relative simple compound usually give crystals with less than 100 atoms in their asymmetric unit and therefore are usually well resolved. In contrast,

macromolecules often involve tens of thousands of atoms in the unit cell and are generally less well resolved with the atoms and chemical bonds appearing as tubes of electron density, rather than of discrete atoms. Single-crystal X-ray diffraction is a non-destructive analytical technique which can provide a lot of detailed information about the internal lattice of crystalline substances like unit cell dimensions, bond-lengths and bond-angles.

It is possible to solve crystal structures creating a set of trial phases for the structure factors. This is possible by using two main methods. The first is the Patterson method based on the assumption that there is at least one heavy atom in the unit cell. The second method, called direct methods, is typically used when the atoms in the structure have similar scattering behaviour. In particular, direct methods calculate the probabilities related to each phase and hence the electron density map of the unit cell (Equation 2.7).

After the attribution of location to the atoms in the structure, the observed structure factors dataset (F_{obs}) is used to create a calculated set of structure factors (F_{cal} or F_c) and least-squares methods are used to refine the atoms position, by minimising the differences between F_{obs} and F_{cal}.

The displacement of the atoms around their equilibrium position is called thermal motion and it depends on the temperature, the mass of the atom and the strength of the bond between the atom and the neighbouring atoms. When the temperature is increased, this vibration increases and the electron density of the atom occupies a larger volume, effectively weakening its scattering behaviour.

The electron density can be modelled as a sphere based on an isotropic displacement parameter (*B*) or as an ellipsoid around its nucleus using an anisotropic displacement parameter.

The residual index, called R factor, is the difference between the observed and the calculated structure factors, and therefore it can be used as a useful measure of the quality of the structure refinement. It can be described as reported in Equation 2.9.

$$R = \frac{\sum|(|F_o| - |F_c|)|}{\sum|F_o|} \qquad \text{Eq. 2.9}$$

In general, the lower the R value, the higher quality of the structure determination. For small molecule structures it is conventional to consider well-defined structures as the ones with *R* values significantly below 0.1 (10%).

The SHELXL-2013structure refinement package has been used to refine structures from single crystal data reported in this PhD thesis.[6] The weighting scheme is reported in Equation 2.10.

$$w = \frac{1}{\delta^2(F_o^2)+(aP)^2+bP'} \qquad \text{Eq. 2.10}$$

P is a summation used in order to reduce bias, and *a* and *b* are adjustable parameters in order to keep the goodness of fit close to 1.0, providing that the model used is adequate.

The *R* factor can be also written related to F^2 as reported in Equation 2.11.

$$wR_2 = \sqrt{\frac{\sum[w(F_0^2 - F_c^2)]^2}{\sum w[F_o^2]^2}} \qquad \text{Eq. 2.11}$$

The *R* factor related to *F* is given in Equation 2.12.

$$wR_1 = \frac{\sum[w(|F_o| - |F_c|)]^2}{\sum w|F_o|^2} \qquad \text{Eq. 2.12}$$

The goodness of the fit between the observed and the calculated structure is based on F^2 and it is described by Equation 2.13.

$$GOF = S = \sqrt{\left\{\frac{\sum[w(F_o^2 - F_c^2)]^2}{n-p}\right\}} \qquad \text{Eq. 2.13}$$

The number of reflection is given by *n* and *p* is the number of refined parameters. When the values of wR_2 (eq. 2.11) deviate from a range two to three times the values of wR_1, a problem with the refinement may be present. For instance, the chosen space group may be wrong or an incorrect crystal system may have been assumed during the integration process. This may mean that the data must be integrated again. On the other hand, in cases where the correct weighting schemes are used, the refinement is significantly improved and wR_1 and wR_2 show low values.

The WinGX software package has been used in this work[7]. This package incorporates the Shelxl routines to solve and refine the crystal structures with a versatile user interface.

Application, strengths and limitation of SXD

When it is possible to obtain suitable crystals, single crystal X-ray diffraction is the most powerful technique to obtain accurate and precise information regarding the unit cell, the atomic positions, bond lengths, *etc*. It is also usually a non-destructive measurement and needs only a really small quantity of sample to obtain a wealth of data. However, single crystal X-ray diffraction shows also some limitations. It requires a single, pure and stable crystal sample with a size generally between 20 and 200 μm. Also, twinned samples can be difficult to handle.

2.2.2 Powder X-Ray diffraction technique (PXRD)

Alternative crystallographic technique is represented by powder X-Ray diffraction (PXRD). In contrast to single crystal X-ray diffraction, this technique allows the sample to be a finely ground crystalline powder, containing a large number of small crystals, called crystallites.[1] Each of these crystallites is randomly orientated with respect to the others, so the diffraction of the monochromatic X-ray beam will come from any crystallites with planes orientated with the correct angle in order to satisfy the Bragg conditions. The angle between the incident and the diffracted beam is equal to 2θ and, due to the random orientation of crystallites, the reflections occur on the surface of the cones that have their semi-apex angle equal to 2θ (Figures 2.7 and 2.8).

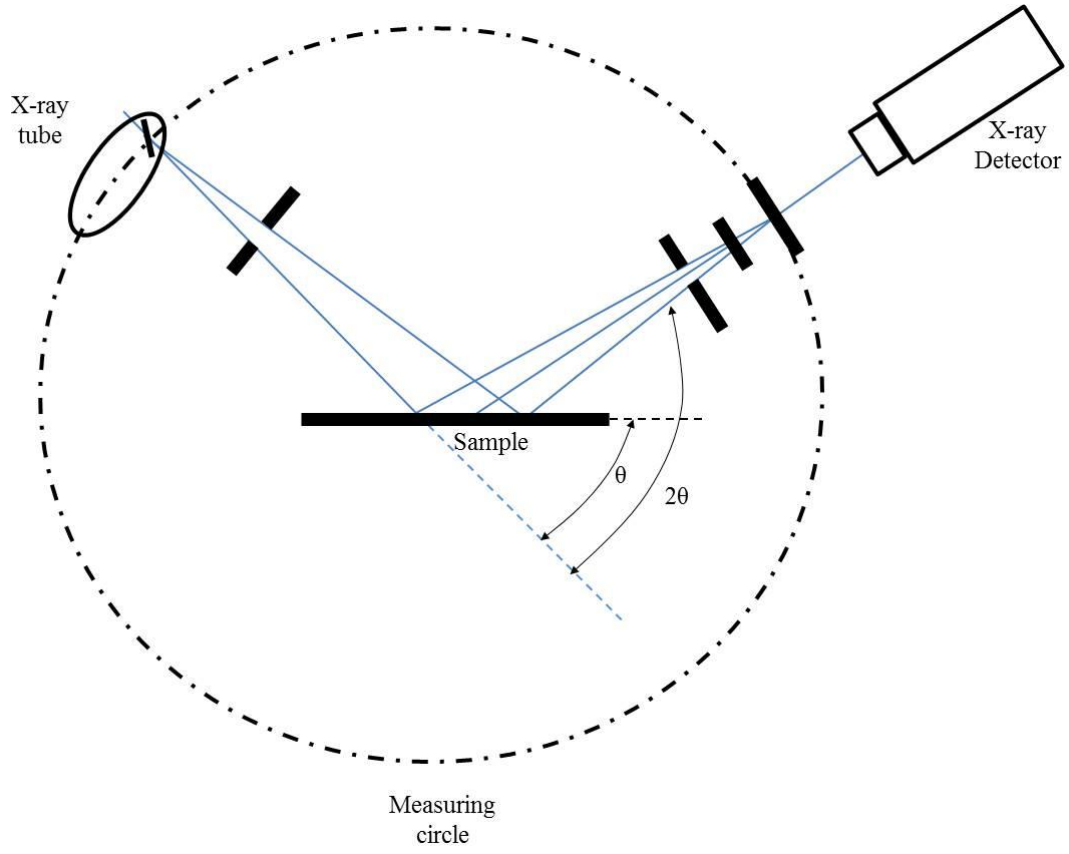

Figure 2.7. Powder X-ray diffraction measurement.

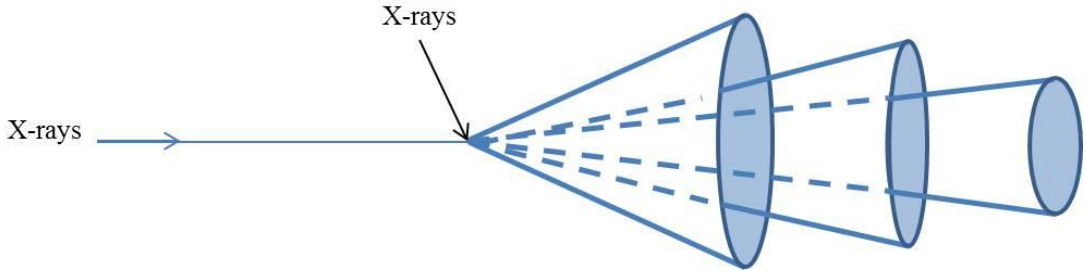

Figure 2.8. Cones produced by a powder diffraction experiment.

In general, the powder patterns are collected at values of 2θ between 5° to 70° using Cu Kα_1 radiation (Figure 2.9).[8]

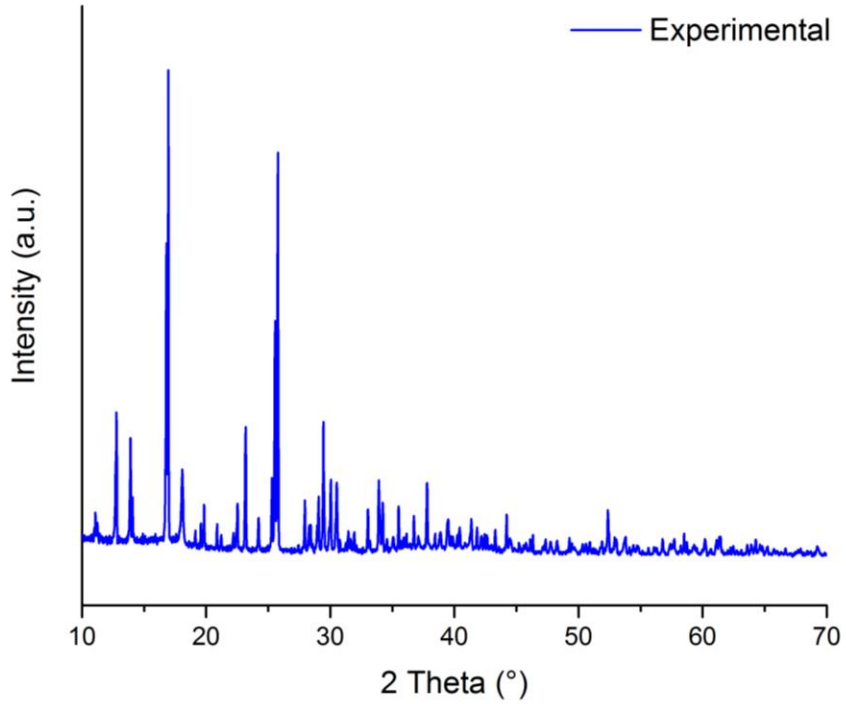

Figure 2.9. Example of X-ray powder diffraction pattern.

Instrumentation and Data collection

The sample has to be a finely ground homogeneous powder. The two different ways to run a powder sample are in reflection and the transmission mode. In the reflection method, the powder sample is mounted in a steel disc. If the amount of the powder sample is too small to fill the well, it can be helpful to use a Teflon disc (available in the 1 mg and 0.5 g size) to reduce the volume of sample needed for the measurement (Figure 2.10). As for SXD, the diffracted X-rays and their intensity are recorded by a detector in a continuous way during the rotation of the sample, but in this case the pattern is only unidimensional and is described as a function of the scattering angle 2θ only (Figure 2.9). Each material has a unique *d*-spacing set and it is possible to identify an unknown sample using a database, such as the International Centre for Diffraction Data Powder Diffraction File (ICDD-PDF).[1]

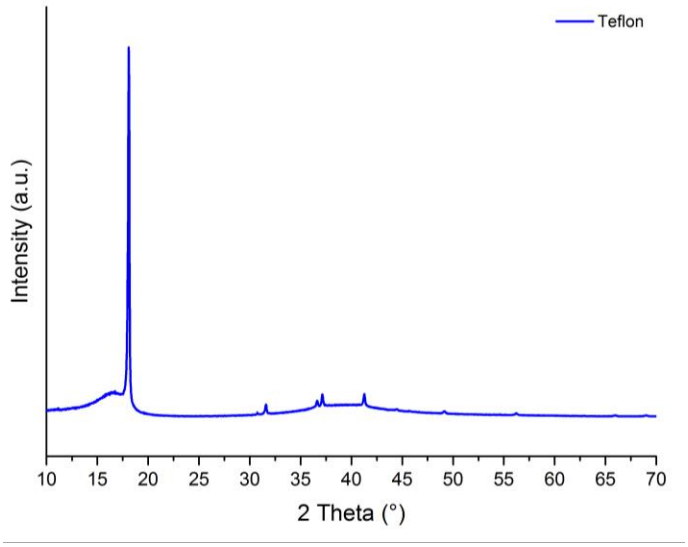

Figure 2.10. PXRD of the blank Teflon sample mounting.

During the course of this project, PXRD were studied in order to investigate the sample purity in comparison with the simulated patterns from single crystal X-ray diffraction data, to compare the powder patterns with known materials to determine if they were new therefore minimising the submission of identical samples for single crystal X-ray diffraction. PXRD patterns were collected on a Panalytical XPert powder diffractometer using a monochromated X-ray beam with a copper anode (Cu $K_{\alpha 1}$ = 1.5406 Å).

Application, strengths and limitation of PXRD

PXRD is a very useful and rapid technique, however the pattern is only unidimensional and is a function of the scattering angle 2θ only. Instead, single crystal X-ray diffraction pattern is three-dimensional and it is a function of three different rotation angles (φ, ω, θ). For this reason, PXRD is a less powerful measurement than single crystal X-ray diffraction. Nevertheless, PXRD is a fast technique with the potentiality to obtain data and so to identify an unknown material in less than twenty minutes using the new

techniques available (*i.e.* Miniflex desktop X-ray diffracometer). Generally, this technique is also able to give an unambiguous material determination using a small amount of sample. Because of the operative advantages in terms of time for PXRD studies, it is often used to identify unknown materials, to collect data about unit cell dimensions or to determine the purity of a sample, whereas single crystal X-ray diffraction is preferred for a full structure determination of a new material.

As in single crystal X-ray diffraction, PXRD is based on constructive interference of monochromatic X-rays by a crystalline sample. In order to obtain all possible diffraction directions of the lattice, the powdered sample is scanned by X-ray through a range of 2θ angles. In particular, it is possible to collect all possible diffraction directions of the lattice with the random orientation of the powdered material. The diffraction peak positions are converted to *d*-spacings and, because *d*-spacings are unique for each material, they are used to identify the chemical nature of the measured sample.

The difficulty in powder diffraction data analysis is to understand which planes are responsible for each observed peak, a process known as indexing reflections, in which the correct *hkl* index is assigned to each reflection. This process is facilitated for samples with high symmetry level but very difficult for large and less symmetrical unit cells.

2.3 Bond valence sum method

The bond valence sum method is a technique to help determine whether the final crystal structure obtained by SXD or another method is correct.[9] It is based on the calculation of the formal oxidation state of the atoms concerned and may also show whether there is any atomic disorder.[9]

The bond valences (*S*), of each bond surrounding a metal centre are summed together, with the total being close to the hypothesised valence state of the metal atom (Equation 2.14).[9]

$$s_1 = e^{\left[\left(\frac{R_0 - R}{B}\right)\right]}$$

$$BVS = \sum_{i=1}^{b} s_1 \qquad \text{Eq. 2.14}$$

S is the bond valence, *R* is the bond length, *Ro* and *B* are bond valence parameters that depend on the two atoms forming the bond (typically, *B* has a fixed value of 0.37 Å).[9] Bond valence sums were carried out for all the structures described in this thesis using the VaList program, written by Andrew Wills.[10]

2.4 Electron microscopy: scanning electron microscopy (SEM) and energy-dispersive X-ray spectroscopy (EDX)

Electron microscopy is a technique largely used in order to characterise solids in terms of structure, morphology, crystallinity, presence of defects and distribution of elements.[5] An electron microscope works in a similar way to an optical microscope, but it uses an accelerated electron beam instead of visible light. Electrons of high energy behave as rays of short wavelength (λ) leading to a high microscope resolution.[5]In order to calculate the electron wavelength, we need to consider the voltage (V) necessary to accelerate the electron.[5] The kinetic energy of the electron is reported in Equation 2.15.

$$\frac{1}{2}mv^2 = eV \qquad \text{Eq. 2.15}$$

In this equation, *e* is the charge of the electron, *m* is its mass and *v* the velocity. Considering the momentum of the electron (*p*), it is possible to rewrite the velocity and so the kinetic energy as in equation 2.16.

$$v = \frac{p}{m}$$
$$\frac{p^2}{2m} = eV \qquad \text{Eq. 2.16}$$

Using the Broglie relation where *h* is the Planck's constant (Equation 2.17) and rearranging it, the kinetic energy of the electron is represented by Equation 2.18.

$$p = \frac{h}{\lambda}$$
$$\frac{h^2}{\lambda^2} = eV \qquad \text{Eq. 2.17}$$

$$\frac{h^2}{\lambda^2} = \frac{p^2}{2m}$$
$$\lambda = \frac{h}{\sqrt{2meV}} \qquad \text{Eq. 2.18}$$

The electron beam can be produced by heating a filament of tungsten or a lanthanum hexaboride (LnB_6) crystal or using a field emission gun (FEG) where tungsten or zirconium oxide are used as cathode material. The beam produced in these ways is then passed through a magnetic coil magnet to be focussed in a high vacuum on to a fine

spot. The vacuum is used in order to avoid any interactions between the beam and extraneous particles. After passing through the sample, the beam is detected by a scintillation counter.[5]

Scanning electron microscopy (SEM) is a technique that allows investigation of the morphology, texture and topography of samples of up to tens or hundreds of nanometres using the field emission electron microscope (FESEM). In this technique, a potential of 1-30 kV is used in order to generate the high energy monochromated electron beam that passes across the surface of the sample. The beam interacts with the sample forming an emission of electrons and electromagnetic radiation (X-Rays) collected by the detector. In particular, the beam ejects electrons from the core energy levels, allowing the high energy electrons to drop down to lower energy levels, thus emitting X-ray radiation. The detected electromagnetic radiation can provide information regarding the elemental composition of the sample; this is known as Energy-dispersive X-ray spectroscopy (EDX). The EDX sensor is capable of detecting and discriminating the energy of the X-ray radiation emitted. The energy of the X-ray emission is specific to the constituent elements. Non-conductive samples require to be coated with an ultrathin layer of electrically-conducting material (usually gold or graphite) to prevent build-up of charge during the scan, while no special preparation is needed for conductive samples.[5] For the work of this thesis, samples were examined using a JEOL JSM-5600 with an accelerating voltage of 5 kV (SEM) and 30 kV (EDX).

2.5 Thermogravimetric analysis (TGA)

Thermogravimetric analysis (TGA) is one of a range of thermal analysis techniques, useful to investigate the properties of solids as function of a change in temperature. In

particular, TGA is useful to investigate decomposition and changes in mass upon heating and cooling. The sample is placed in an alumina crucible and heated at a controlled, uniform rate under a gaseous flow (usually nitrogen) in order to prevent oxidation or other undesired reactions. The change in mass of the sample is recorded during the whole duration of the experiment and can be useful to provide information regarding the degradation temperature and the stability of the sample against the temperature.[5]

All Thermogravimetric Analysis (TGA) data reported in this thesis were carried out on a Stanton Redcroft STA-780 series instrument heating the sample up to 500 °C.

2.6 Fourier transform infrared spectroscopy (FTIR)

Infrared spectroscopy uses the infrared region of the electromagnetic spectrum, characterised by lower frequency and longer wavelength compared to visible light. There are three main parts of the infrared region: the near (14000-4000 cm^{-1}, 0.8-2.5 μm), the mid (4000-400 cm^{-1}, 2.5-25 μm) and the far-infrared (400-10 cm^{-1}, 25-1000 μm). The mid-infrared region is the most commonly used because it is related to the fundamental vibration states of a specific sample.[5] Infrared spectroscopy is based on the concept that materials have specific frequencies of vibration, and the vibration is related to discrete energy levels. In order to vibrate, and therefore to be active to infrared spectroscopy, the sample has to change its permanent dipole state.[5]

For the purpose of this thesis a Shimadzu IRAffinity-1S instrument was used. In this instrument, there is a mirror able to move in order to change the infrared light distribution, that then passes through the interferometer. The recorded signal represents the light output as a function of the mirror position and it is turned into the final

spectrum (light output versus infrared wavelength or wavenumber) using a Fourier transform method. Prior to each experiment a reference spectrum was recorded, in order to correct the final spectra background noises.

2.7 Electrochemical characterisation

2.7.1 Basic principles of electrochemical energy storage and conversion

The different oxidation states allow atoms to accept or donate electrons in the presence of an electrolyte, leading to an electrochemical reaction. In order to have a continuous transfer of electrons and to respect the principle of the electroneutrality, a second electrochemical reaction needs to take place in the opposite direction. This is the main principle for electrochemical cells, devices able to convert chemical energy into electrical energy.[11,12]

The electromotive force (emf) of the cell defines the potential difference across the terminals of an electrochemical cell when no current is passing through the cell or the circuit is open. It is a quantitative way to measure the tendency of the cell to have internal reactions. It is possible to apply a voltage E by a potentiometer in order to stop the cell reaction when no current is passing through the cell.[12] For a cell reaction expressed in Equation 2.19, the emf can be expressed by the Nernst equation for galvanic cell as reported in Equation 2.20.[12]

$$v_A A + v_B B + \ldots \longrightarrow v_P P + v_Q Q + \ldots \qquad \text{Eq. 2.19}$$

$$E = E^{\theta} - \frac{RT}{nF}\, ln\left[\frac{[P]^{v_P}[Q]^{v_Q}\ldots}{[A]^{v_A}[B]^{v_B}\ldots}\right] \qquad \text{Eq. 2.20}$$

E^o is the standard emf of the cell and represents the equilibrium voltage when all the cell parameters are in their standard states (solution species expressed in molar concentration, gasses with 1 bar as pressure and solid phases in their more stable form), v_i is the stoichiometric number, R is the universal gas constant (R = 8.314472 J K^{-1} mol^{-1}), F is the Faraday constant representing the number of coulombs per mole of electrons (F = 9.64853399×10^4 C mol^{-1}) and z is the number of moles of electrons transferred in the cell reaction.[12]

The quantity of chemical species reduced or oxidised during an electrochemical process depends on the total electric charge transferred through the interfaces between the metal and the solution where an electrical double layer and a difference of potential is formed. The relative equilibrium difference of potential (ΔE) between the two electrodes is reported in Equation 2.21.[11,12]

$$\Delta E = -\frac{\Delta G}{nF} \qquad \text{Eq. 2.21}$$

ΔG is the variation of the Gibbs free energy for the entire cell reaction, n is the number of equivalents involved in the process and F is the Faraday's constant (96487 C mol^{-1}). This relationship between the quantity of chemical species reduced or oxidised during an electrochemical process and the total electric charge transferred through the

interfaces is regulated by the Faraday's law, that gives the amount of electrical charge transferred in an electrochemical reaction (Equation 2.22).[11,12]

$$Ox + ze^- \leftrightarrows Red$$

$$Q = zF\frac{m}{M} \qquad \text{Eq. 2.22}$$

$$m = \frac{QM}{Fz}$$

Q is the total electric charge generated during the reaction, m is the mass of the substance involved in the electrochemical process, M is the molecular weight of the substance, F is Faraday's constant (96487 C mol^{-1}, 26.8 Ah mol^{-1}) and z is the valence number (the number of electrons transferred per mole of substance). There is a proportional relationship between the amount of substance required to transfer a certain amount of charge during the redox reaction and the equivalent mass of the substance.[11,12] In particular, in order to maximise the amount of charge transferred per unit mass (Q) a material with low molar mass (M) and high equivalent number (z) would be desiderable.[11,12] The total amount of charge transferred per unit mass of electrode material during the time required for discharge and charge cycle is known as specific capacity (Q_{sp}) and it is mathematically represented in Equation 2.23.[11,12]

$$Q_{sp} = I\frac{t}{m} \qquad \text{Eq. 2.23}$$

I is the current, m is the unit mass of the electrode and t is the time required for a complete charge and discharge cycle.

Modern batteries are investigated in order to obtain materials with high specific charge and a high potential difference between the two electrodes (anode and cathode).[11,12] The total amount of energy that can be stored in a battery material per unit of mass is known as specific energy (W_e) and its theoretical maximum value can be calculated from the Equation 2.24.[11,12]

$$W_e^{th} = \frac{\Delta G}{\sum_i n_i M_i} \qquad \text{Eq. 2.24}$$

The reactant involved in the process is represented by i, n_i are the moles of the reactant and M_i its molar mass. In practice, the specific energy of a battery does not reach the theoretical value and the specific energy for a redox process running at constant potential can be reported as in Equation 2.25.[11,12]

$$W_e = Q_{sp} V \qquad \text{Eq. 2.25}$$

The weight of the reactant contributes to the total weight of the battery system, having consequences on its portability. For this reason, it is important to use the smallest amount of reactant when it is possible.[11,12]

The amount of energy which can be stored in a battery system can be expressed also in terms of unit volume, known as energy density (W_{dens}), using the Equation 2.26.[11,12]

$$W_{dens} = W_e \rho \quad \text{Eq. 2.26}$$

Commonly, a C-rate of 1 C is known as a one-hour discharge, a 0.5 C (or C/2) is a two-hour discharge and 0.2 C (or C/5) is a 5-hour discharge. Ideally battery materials should provide high energy, high capacity and high power working at a high discharge current regime. This means that the charge needs to be supplied by the electrode material also at rates more than 1 C, when the fully charged battery rated at 1 Ah should provide 1 A for one hour. If the same battery has been discharged at 0.5 C, it should provide 500 mA for two hours, and at 2 C it releases 2 A for 30 minutes. The applications of a battery system not only depend on the performance described above but also on the rate at which a battery can be discharged. This is affected by the movement of ions during the process. In order to respect the electroneutrality principle, the diffusion of ions and charge has to be equal to the number of electrons passing in the external circuit. In most battery materials, intercalation is the rate limiting step due to the low mobility of ions.[11,12]

2.7.2 Electrode fabrication and cell assemble

All the materials synthesised during this PhD project and reported in this thesis were investigated mainly for applications as cathode materials in rechargeable sodium batteries.

After the synthesis and the physical characterisation steps, carried out using the techniques described above, electrochemical cells were assembled using the active material as an electrode and they were tested using the galvanostatic cycling technique.

Two main methods were used to prepare the electrodes: pellet form or tape casting. Using the first method, the active material was hand ground, adding carbon powder (Super S and/or Ketjenblack) and a binder (PTFE or Kynar). The resultant material was then pressed into a self-supporting pellet of 13 mm diameter. Alternatively, in the tape casting method, the same mixture was suspended in a solvent (usually tetrahydrofuran) in order to dissolve the binder and form a homogeneous slurry. This was then cast onto aluminium foil using a doctor blade and then dried in oven at 80 °C overnight. The aluminium foil with the dried cathode material was then cut in order to obtain circles of 13 mm diameter ready to be inserted into cells. Typical electrode active material loadings were 3-5 $mgcm^{-2}$. Electrodes were incorporated into coin cells (CR2325 type, supplied by National Research Council of Canada) with a sodium metal counter electrode, and with an electrolyte solution composed of 1M $NaClO_4$ in propylene carbonate, containing 3% fluoroethylene carbonate as an additive (Figure 2.11). Electrochemical measurements were carried out at room temperature using a Biologic MacPile II system in the potential ranges 1.5-4.2 V and 1.7-4 V at various C-rates.

The samples for *ex situ* measurements (PXRD) were prepared by extracting the cathode material from the coin cells and washing it with dry dimethyl carbonate (DMC), that was then removed and the material allowed to dry. The materials were loaded in 0.5 mm quartz capillaries and PXRD patterns were collected on a Stoe STADI/P diffractometer operating in capillary mode, with Fe $K_{\alpha 1}$ radiation (λ = 1.936 Å) in order to eliminate Fe fluorescence, from an overnight run. Construction of coin cells and preparation of the samples for *ex situ* measurements (PXRD) were performed in an Ar-filled glovebox.

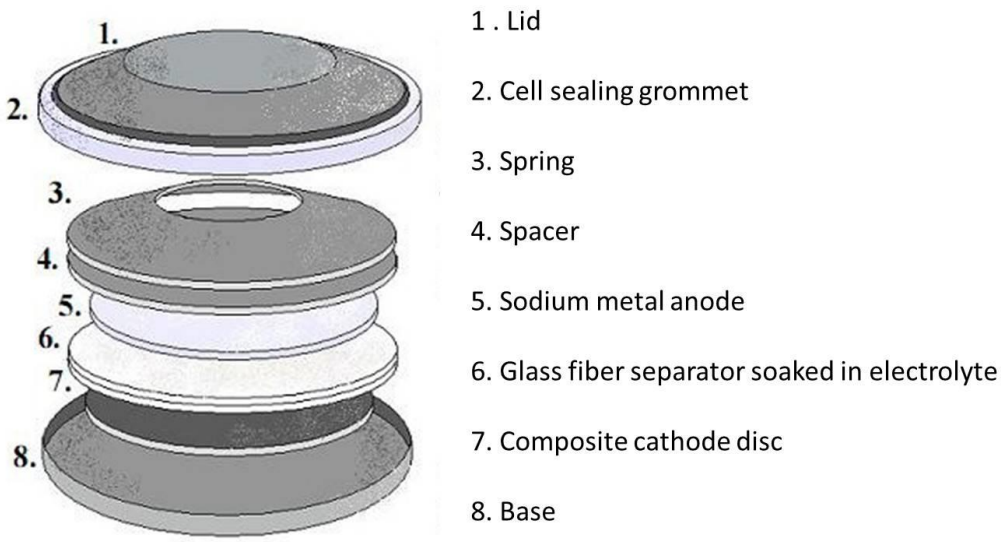

Figure 2.11. Expanded view of a coin cell.

2.7.3 Galvanostatic cycling

Galvanostatic cycling is an important technique used to investigate the behaviour of battery materials, whereby a constant current is applied between the working and counter electrodes and the resulting difference of potential is measured as a function of time. During the charge process, a positive current is applied to the system oxidising the working electrode until the defined upper potential limits are reached. On the other hand, during the discharge process, a negative current is applied causing the reduction of the working electrode until the lower potential limit is achieved. The fixed and investigated voltage range has to be wide enough in order to contain the potential values at which the redox process of sodium ions insertion and removal occur. However, it has to be narrow enough in order to avoid oxidation and reduction of the electrolyte.[12]

A voltage plateau is typical of a process where sodium ion intercalation or de-intercalation occurs as a two-phase process. Instead, for a single-phase solid solution process a sloping voltage profile is typically observed.[5]

During the electrochemical testing, several charge and discharge cycles are carried out in order to investigate the efficiency of a battery material. In theory, these different profiles should coincide. However, in practice this does not happen due to different phenomena such as the electrolyte resistivity and structural changes occurring within the electrode material.

The most typical resulting plots after the galvanostatic cycling experiment are the ones showing the relationship between the cell voltage (V) and the specific capacity (Q_{sp}) and the ones comparing the capacity and the cycle number. Both of them are key information for a successful material. The maximum theoretical capacity value (Q), for a cathode material (M) when a process of intercalation or deintercalation is happening can be calculated with Equation 2.27.

$$Na_xM + \Delta xNa^+ + \Delta e^- \leftrightarrows Na_{X+\Delta x}M$$

$$Q = \frac{nF}{M3.6}$$

Eq. 2.27

The number of electrons exchanged during the process is represented by n, F is Faraday's constant (96485 C mol^{-1} or 26.801 Ah mol^{-1}) and M is the molecular mass (g mol^{-1}).

2.8 Magnetic characterisation

All the magnetic measurements reported in this PhD project were carried out at either the University of Edinburgh, the Moscow State University or the University of Tokyo.

Measurements carried out in Edinburgh were performed on a Quantum Design MPMS SQUID magnetometer by Dr Lucy Clark, while thermodynamic property measurements

in Moscow were studied by measurements of ac-magnetic susceptibility χ (10G, 10 kHz), dc-magnetisation M, and specific heat C_p in the temperature range T = 2-300 K using various options of the Quantum Design Physical Properties Measurements System PPMS-9T, by Professor Alexander N. Vasiliev and his research group. Measurements carried out in Tokyo were performed by Dr Hajime Ishikawa on SQUID magnetometer (MPMS3, Quantum Design).

2.8.1 Magnetisation (M) and superconducting quantum interference device (SQUID)

The superconducting quantum interference device (SQUID) is a very sensitive magnetometer used to measure extremely weak magnetic field. It is sensitive enough to measure fields as low as 5 x 10^{-18} T with few days needed for the measurement. In this technique the sample is placed at the centre of a coil and then removed to a large distance (the typical scan length is ~ 4 cm) (Figure 2.11).[13] This movement induces a flow of electrons and so a voltage V in the coil. A magnetic field is applied and oriented parallel to the sample with the sample slowly and in small increments moving through the field.[1,5,13] The current flow passing through the coil of the wire that is surrounding the sample changes as the sample passes though. The magnetic flux (Φ) produced by the sample and detected in this way is represented in Equation 2.28.

$$\Phi = \int V \, \mathrm{d}t \qquad \text{Eq. 2.28}$$

Usually there are two counter-wound coils in the magnetometer, placed in order to cancel the voltages due to the changes in the applied field and so only the signal of the sample is detected (Figure 2.12).[1,5,13]

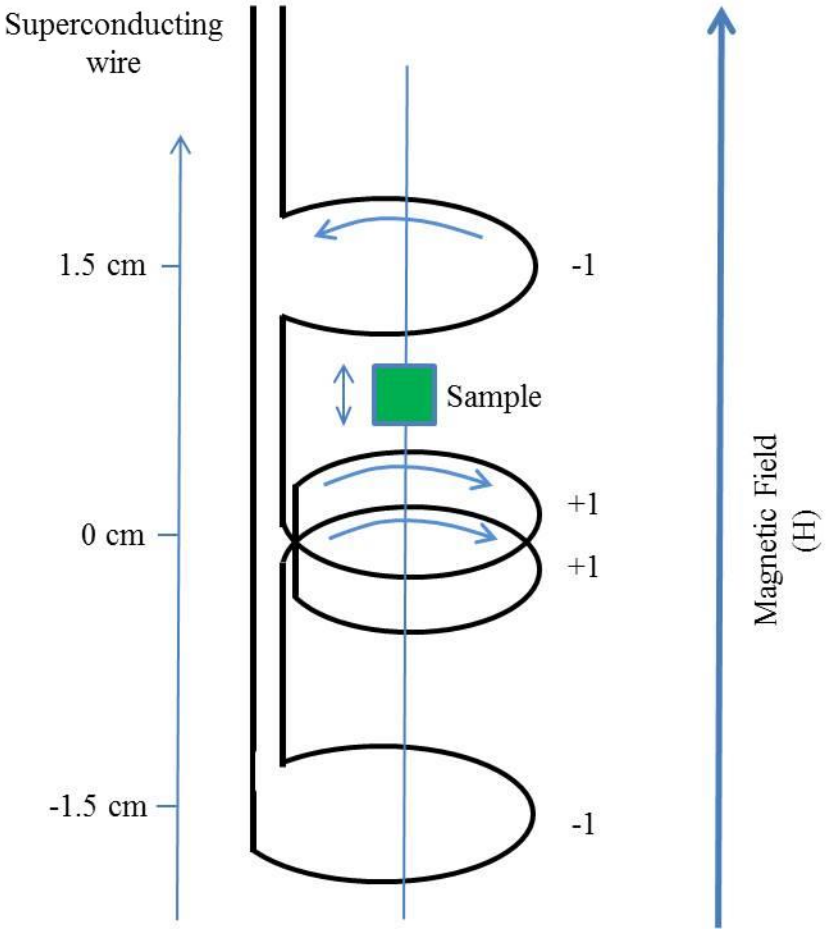

Figure 2.12. Schematic diagram of a SQUID Magnetometer.

When a sample is passed through the coils in the SQUID, the persistent current induced is proportional to the magnetisation of the sample. The magnetisation, *M*, is the magnetic moment per unit volume. In a magnetic solid measured in the SQUID in an applied field, the relationship between the magnetisation and the applied field is represented in Equation 2.29.

$$M = \chi H \qquad \text{Eq. 2.29}$$

The field is represented by H and χ is the magnetic susceptibility. Thus the magnetic susceptibility is given by dividing the measured magnetisation by the applied field. This means that the magnetic susceptibility represents the magnetic moment induced by a magnetic field per unit volume. However, more often the molar magnetic susceptibilities are used. The magnetic susceptibility is useful as it gives a measure of the atomic magnetic moments in the sample through the Curie Law represented in Equation 2.30.

$$\chi = \frac{C}{T} \qquad \text{Eq. 2.30}$$

The Curie constant is represented by $C \sim (8\mu_{eff})^{0.5}$ and μ_{eff} is the effective magnetic moment. However, the Curie law describes paramagnetic systems in which there are no interactions between neighbouring spins, which is not often the case in magnetic solids. Therefore, the modified Curie-Weiss law is often used to take these magnetic interactions into account following the Equation 2.31.

$$\chi = \frac{C}{T-\theta} \qquad \text{Eq. 2.31}$$

The Curie constant is represented by C, T is absolute temperature and θ is the Weiss constant. At $T = \theta$, there is a singularity in the susceptibility and below this temperature the ferromagnet shows a spontaneous magnetisation.

2.8.2 Specific heat (C_p)

The specific heat at constant pressure can be expressed in terms of energy and temperature, in conditions of constant magnetic field as in Equation 2.32.[13]

$$C_p = \left(\frac{\partial \vec{E}}{\partial T}\right)_B \qquad \text{Eq. 2.32}$$

The specific heat has a broad maximum close to the Schottky anomaly as represented by Equation 2.33.[13]

$$K_B T \sim \mu_B B \qquad \text{Eq. 2.33}$$

The Bolzmann constant is represented by K_B, T is the temperature, μ_B is the Bohr constant and B is the magnetic field. This behaviour is due to the fact that at this temperature it is possible to obtain transitions between the two states of the system if thermally excited. However, both at low and at high temperature it is difficult to change the orientation of the spins due to energy issues. In particular, at low temperature, there is not enough energy to excite transitions from the ground state and all the spins are aligned with the magnetic field. Instead, at high temperature both states are equally occupied. Between low and high temperatures, there is a middle stage where there is a maximum of the system with peaks in the value of the heat capacity, useful indicators that something interesting may be happening, such as a phase transition (Figure 2.13).[13]

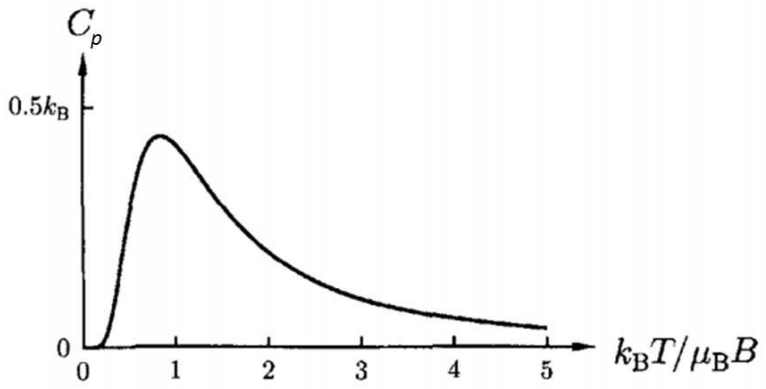

Figure 2.13. Specific capacity (C_p) behaviour at constant applied magnetic field.

2.9 Synthetic procedures

During the course of this PhD project, 1387 reactions were carried out using hydrothermal or solvothermal techniques. In both cases, the experiments were undertaken in Teflon-lined steel autoclaves.

A general reaction scheme is as follows: a metal source along with a source of potassium/oxyfluoride and fluorine is added to an autoclave. The reaction was carried out with or without having the addition of a solvent and of HF to the mixture, as HF is a fluorine source as well as acting as a mineralising agent. Water was used as a solvent in order to maintain an environmental friendly approach to the synthesis. Other solvents, such as methanol, ethanol, acetone, butanol, ethylene glycol and mixtures of them were also used, in order to test their efficacy in producing crystalline samples. The quantity of solvent used to carry out the reactions was up to 5 ml per autoclave. Different transition metal sources were used during the PhD duration, specifically iron, molybdenum, cobalt or manganese.

The autoclaves (volume equal to 40 ml) were sealed and heated at an appropriate temperature (between 100 °C and 190 °C) for a maximum of 15 days. Once the vessel

had cooled to room temperature, the contents were filtered, washed with water, or with the solvent used in the reaction, and dried at 60 °C in air.

In most cases, the same product was formed regardless of solvent choice; sometimes no crystalline material formed at all.

Initially the reactions were carried out at 100 °C, with variation of the reagent ratios and the type and the amount of solvent(s). The same reaction was repeated at different temperatures with or without the addition of HF. In this semi-systematic way it has been possible to carry out a lot of reactions and to compare the outcomes, indicating the effect of the type/amount of chemicals and solvent used, plus the effect of the temperature and the presence of HF.

2.10 References

1. A. R. West, *Basic Solid State Chemistry*, John Wiley & Sons, Chichester, 1991.
2. R. A. Laudise, *Chemical and Engineering News*, 1987, **65**, 30.
3. University of Madrid, Department of Crystallography and structural biology website: http://www.xtal.iqfr.csic.es/Cristalografia/parte_02-en.html
4. A.R. West, *Solid State Chemistry and its Applications*, John Wiley & Sons, Singapore, 2005.
5. P. W. Atkins, *Physical Chemistry*, Oxford University Press, Oxford, 9th Edition edn., 2009.
6. G. M. Sheldrick, *Acta. Cryst.*, 2008, **64**, 112.
7. L. J. Farrugia, *J. Appl. Cryst.*, 2012, **45**, 849.
8. R. Jenkins, R. Snyder, *Introduction to X-Ray Powder Diffractometry*, Wiley, New York, 1996.
9. N. E. Brese, M. O'Keeffe, *Acta. Cryst.*, 1991, **B47**, 192.
10. A.S. Wills, I. D. Brown. "VaList." CEA, France (1999).
11. M. Winter, R.J. Brodd, *Chem. Rev.*, 2004, **104**, 4245.
12. C.A. Vincent, B. Scorsati, *Modern Batteries, 2nd Edition*, Arnold Publ. Ltd., London, 1997.
13. S. Blundell, *Magnetism in Condensed Matter*, Oxford University Press, Oxford, 2001.

Chapter 3

$NaFe_3(HPO_3)_2[(H,F)PO_2OH]_6$: a New Cathode Material for Sodium Batteries

3.1 Introduction

The addition of fluoride into the structure of a potential cathode material increases the possibilities to create 3D framework structures. Therefore, the presence of fluoride can provide a stable host with low volumetric change and enhanced voltage during sodium ions insertion and extraction.[1-4]

This aspect is particularly useful for sodium ion batteries where a large volumetric change occurs when sodium ions are intercalated into the structure. The large ionic size of sodium (ionic radii 1.02 Å) leads to poor cycle life for sodium ions batteries.[1-4]

Fluoride anions are considered a key element for battery materials also due to their inductive effect, larger than oxide-based ligands, which leads to a naturally higher working potential for the hosting battery.[5,6]

Even if fluorine shows all these potential advantages, fluorine-containing compounds based on phosphite functional groups (HPO_3^{2-}, FPO_3^{2-}, *etc.*) have not been studied

before as battery materials compared to the more commonly studied phosphate-based compounds.[1-3,7-13]

The aim of this chapter is to report the structural and electrochemical properties of a new potential cathode material for sodium batteries, $NaFe_3(HPO_3)_2[(H,F)PO_2OH)_6]$ (hereinafter abbreviated "**Fe-1**"), based on the fluorophosphite group.

3.2 Material synthesis

Fe-1 was synthesized through hydrothermal synthesis with reaction of NaF (1 mmol), Fe_2O_3 (1 mmol) and H_3PO_3 (0.122 mmol), without the addition of any solvent. This mixture was sealed in a Teflon-lined stainless steel autoclave and heated to 140 °C for 3 days. The mixture was cooled to room temperature and pink air-stable prismatic crystals were recovered by filtration from a minor aqueous phase.

3.3 Structural characterisation

Fe-1 crystals are well-faceted prismatic blocks with a particle size of 200 μm as shown in the SEM images (Figure 3.1).

a)

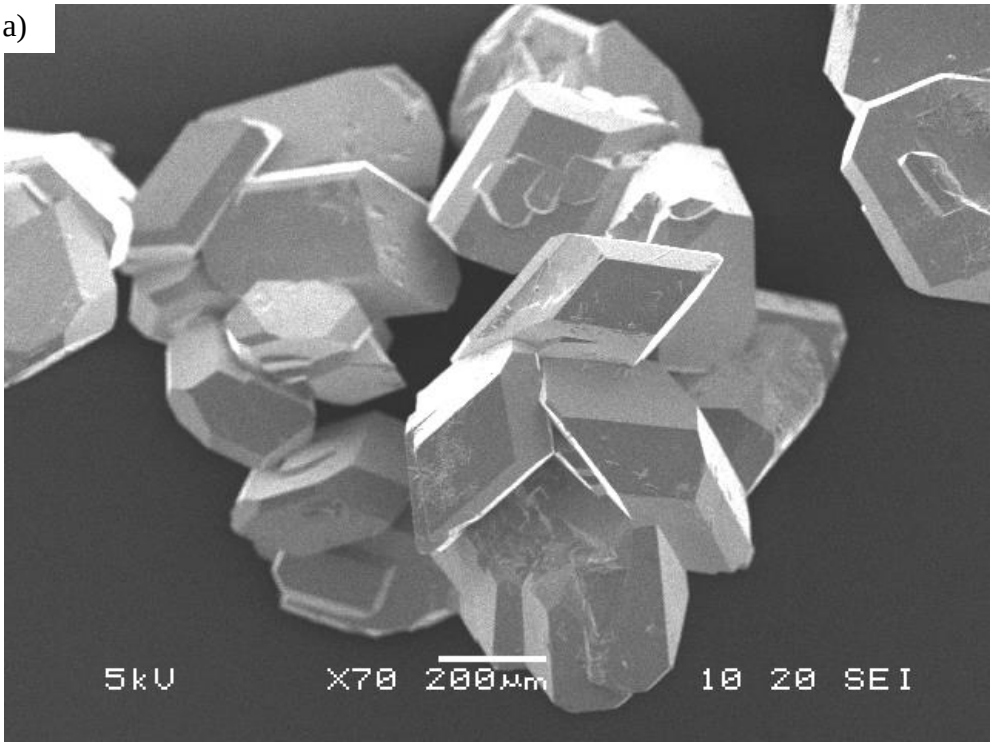

b)

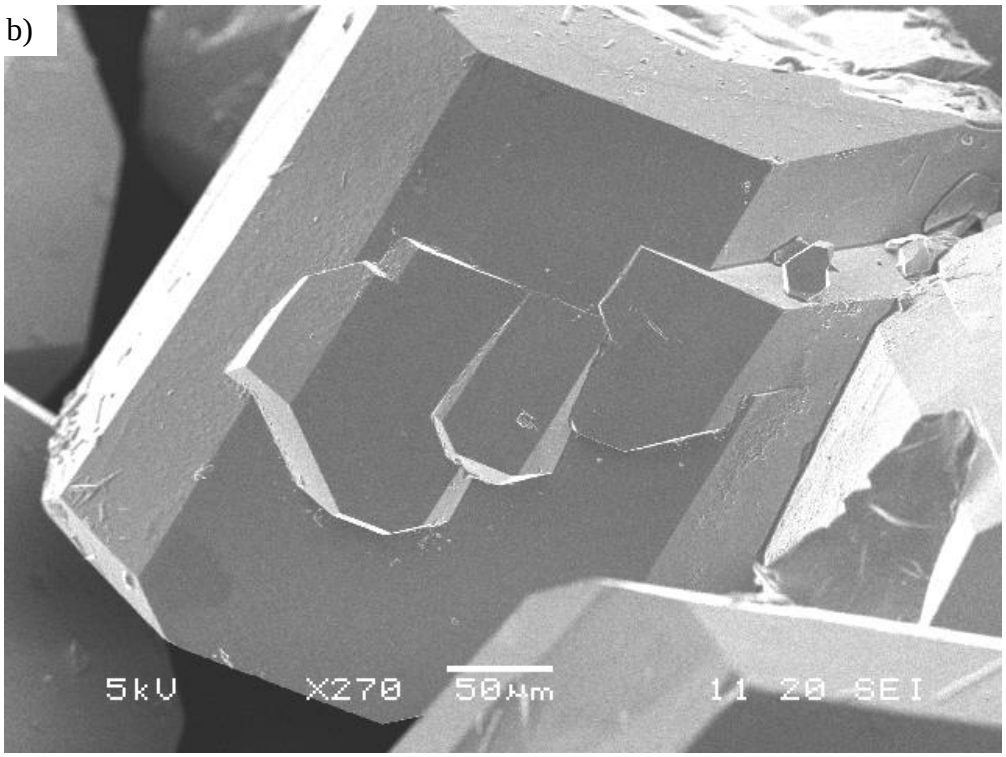

Figure 3.1. a) SEM picture and b) zoom-in of typical **FE-1** crystals.

The analysis of the single crystal X-ray diffraction data shows **Fe-1** adopting a triclinic crystal structure in the $P\bar{1}$ centrosymmetric space group (Table 3.1).

Table 3.1. Crystallographic data for **Fe-1**.

Molecular formula	**$NaFe_3(HPO_3)_2((H_{0.93}F_{0.07})PO_2OH)_6$**
Formula Mass (amu)	843.61
Crystal system	Triclinic
Space group	P -1
a	7.5302(4) Å
b	9.1696(3) Å
c	9.4732(11) Å
α	118.063 (5)°
β	101.274(12)°
γ	101.192(12)°
V (A^3)	534.25 (8)
Z	1
ρ (calcd) (g/cm^3)	2.622
Temp (K)	173 (2)
F (000)	418.0
μ (mm^{-1})	2.747 (calculated)
R_{int}	0.0594
R_1, wR_2 (I >4σ)	0.0272, 0.0812
R_1, wR_2 (all data)	0.0284, 0.0832
Reflections number gt	1798
Reflections number total	1950
GOF on F^2	0.654

Fe-1 exhibits a novel 3D framework crystal structure with FeO_6 octahedra corner-sharing with HPO_3 and HPO_2OH tetrahedra (Figures 3.2-3.4). The structure has a low

symmetry and two crystallographic distinct Fe sites (one at an inversion centre), four P sites and one Na site (at an inversion centre) are present in the asymmetric unit. Open channels are present in the structure and run along all three principal directions of the lattice. Sodium ions reside inside the open channels and are coordinated to six different HPO_2OH groups *via* the oxygen atoms of the P-O-H moieties. The net result is a complex and quite open framework amenable to several distinct ionic migration pathways for sodium ions. The distance between iron atoms surrounding the 3D channels is in the range of 9.16-10.17 Å whereas the Na-Na distance is in the range of 7.53-9.16 Å (Figures 3.2-3.4).

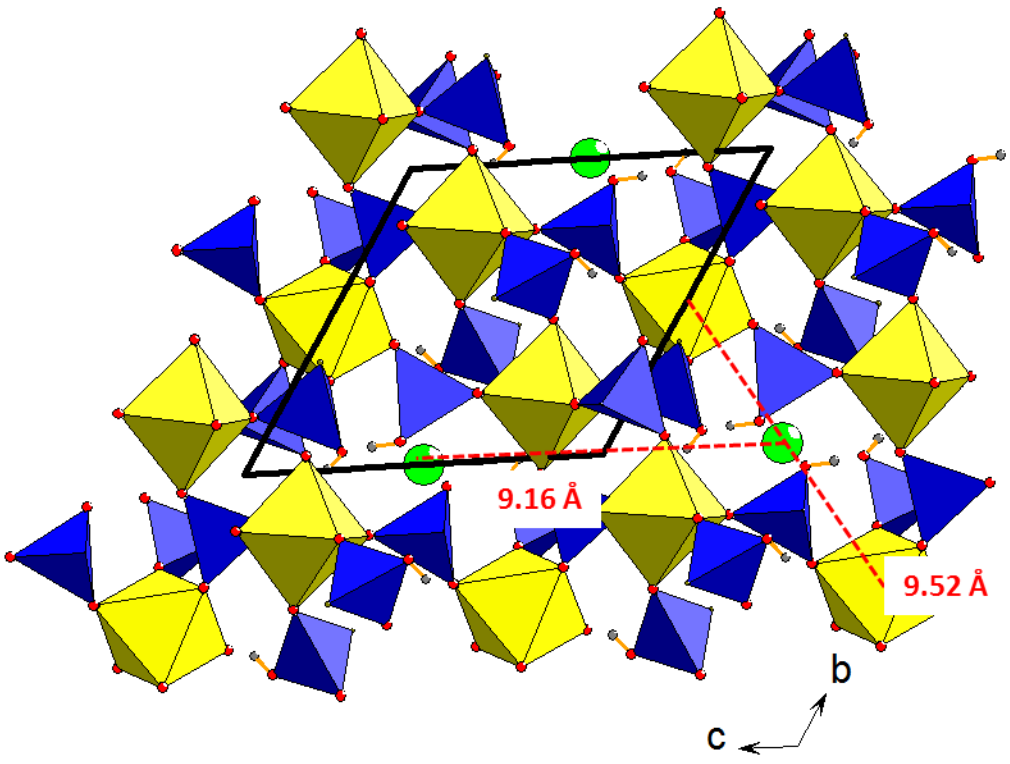

Figure 3.2. Polyhedral representation of the **Fe-1** crystal structure along the *a*-axis. FeO_6 octahedra in yellow, phosphite tetrahedra in blue, sodium ions in green, oxygens in red, hydrogens in grey.

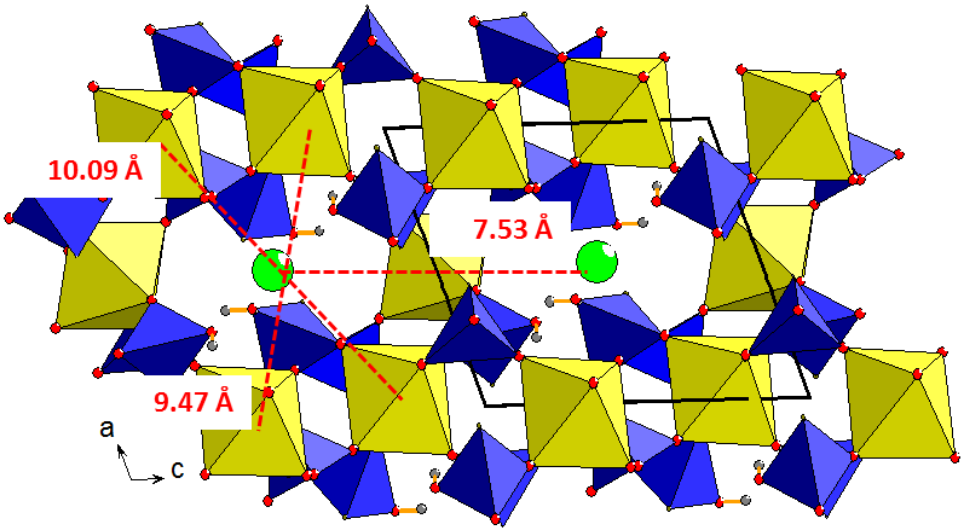

Figure 3.3. Polyhedral representation of the **Fe-1** crystal structure along the *b*-axis. FeO_6 octahedra in yellow, phosphite tetrahedra in blue, sodium ions in green, oxygens in red, hydrogens in grey.

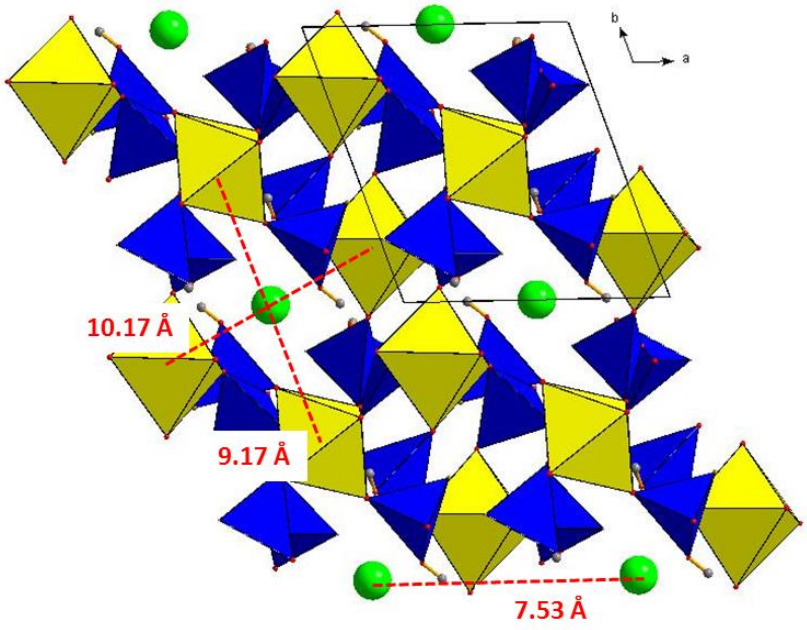

Figure 3.4. Polyhedral representation of the **Fe-1** crystal structure along the *c*-axis. FeO_6 octahedra in yellow, phosphite tetrahedra in blue, sodium ions in green, oxygens in red, hydrogens in grey.

The single crystal data were analysed refining all non-H atoms. All H-atoms were located by Fourier methods and refined without constraints. However, two of the P-H moieties showed significantly enhanced electron density (1-2 e $Å^{-3}$) at the 'H' sites, suggesting the possible presence of heavier atoms. In order to investigate further this aspect, Energy-dispersive X-ray spectroscopy (EDX) was carried out. The qualitative EDX analysis confirmed the presence of oxygen, sodium, phosphorous and iron in the **Fe-1** compound. However, the data also showed the presence of fluorine in the compound (Figure 3.5).

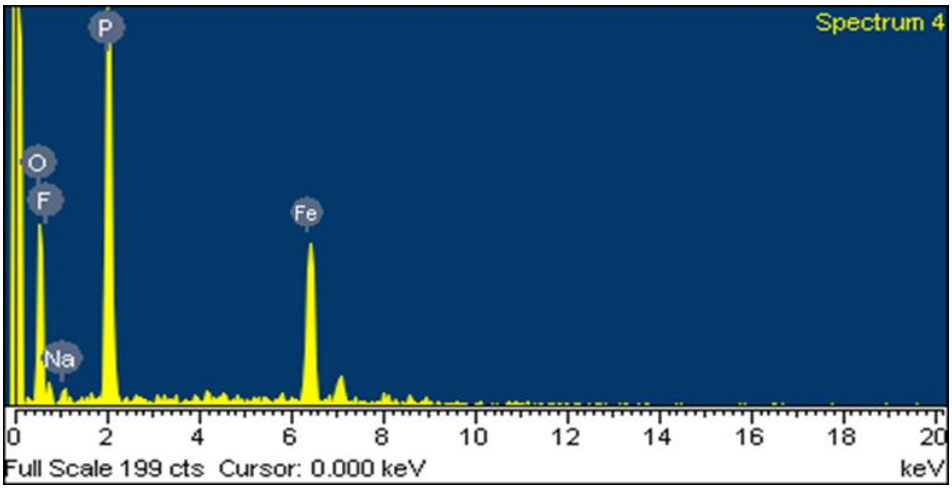

Figure 3.5. EDX spectrum for **Fe-1**.

In particular, fluorine atoms replace the hydrogen atoms directly bonded with the phosphorus in the $(HPO_2OH)^-$ groups. Taking into account this fluorine contribution, the final refinement suggests $NaFe_3(HPO_3)_2[(H_{0.93},F_{0.07})PO_2OH]_6$ as the approximate final composition.

Both of the iron sites are occupied by Fe^{3+} with octahedral coordination and bond lengths in the normal range for Fe^{3+} (1.974 – 2.026 Å).[14-18] No direct Fe-O-Fe linkages were observed in the structure. In order to confirm the iron oxidation state and the

location of OH groups, Bond Valence Sum (BVS) calculations were carried out. The Bond Valance parameters relate the bond valances and the bond lengths (see Chapter 2, Section 2.3). The data obtained from the BVS calculations for **Fe-1** using the Bond Valance parameters reported in literature for the Fe-O bond (1.759 Å), the HP-O bond (1.626 Å) and the Na-O bond (1.80 Å) are in good agreement with the hypothesised valence state of the iron (3+) and the HP group (4+). Moreover, the difference between the hypothesised valance state and the BVS calculations is negligible, allowing to consider of minimal size the disorder and the partial occupancy effects in the **Fe-1** structure (Table 3.2).[19,20]

Table 3.2. Selected bond lengths and bond valence sums for **Fe-1**.

		Bond length (Å)	Bond valence
Fe1	O3 x2	1.9884(18)	0.538
	O4 x2	1.9822(17)	0.547
	O8 x2	2.0259(18)	0.486
			∑ **3.142**
Fe2	O2	1.9948(18)	0.529
	O6	1.9744(19)	0.558
	O7	2.0210(18)	0.492
	O9	1.9883(18)	0.538
	O10	1.9953(18)	0.528
	O12	1.9778(18)	0.553
			∑ **3.198**
H2P1	O1	1.571(2)	1.160
	O2	1.4999(19)	1.406
	O3	1.5065(19)	1.381
			∑ **3.947**
H3P2	O4	1.4957(18)	1.452
	O5	1.574(2)	1.150
	O6	1.488(2)	1.452
			∑ **4.054**
H5P3	O7	1.5350(19)	1.279
	O8	1.5290(19)	1.300
	O9	1.5191(2)	1.335
			∑ **3.914**
H6P4	O10	1.4994(18)	1.408
	O11	1.576(2)	1.145
	O12	1.5022(19)	1.400
			∑ **3.953**
Na1	O1 x2	2.5022(19)	0.151
	O5 x2	2.349(2)	0.229
	O11x2	2.504(2)	0.151
			∑ **1.062**

The purity of the sample was verified by Powder X-ray diffraction (PXRD) experiments. The good match of the patterns suggests a good level of purity of the

sample. Extra peaks at 17° and 33° are typical observed for the Teflon support used to carry out the powder diffraction measurements (Figure 3.6).

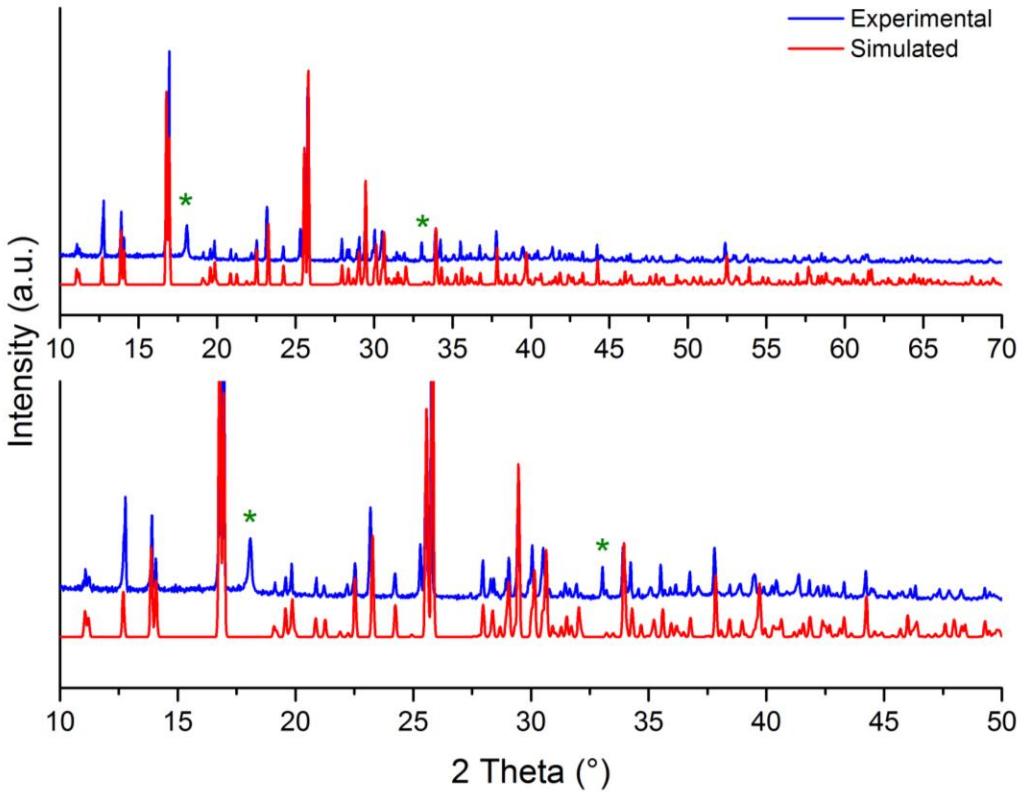

Figure 3.6. Observed and simulated PXRD pattern for **Fe-1**: Experimental patterns in blue and calculated patterns from single crystal data in red; full pattern on the top, zoom-in of low angle region on the bottom. Peaks arising from the Teflon sample mounting are marked with an asterisk.

Infrared spectroscopy (IR) was used to determine the presence of P-H bonds in the structure. The IR spectrum of **Fe-1** mainly consists of strong absorption peaks corresponding to the P-H and the P-O bonds of the phosphite moiety in the structure. The data show a typical P-H stretching signal at 2450 cm^{-1} and a strong PO_3 stretching peak in the range of 950-1150 cm^{-1} confirming the presence of P-H and P-O bonds in the crystal structure (Figure 3.7).[21]

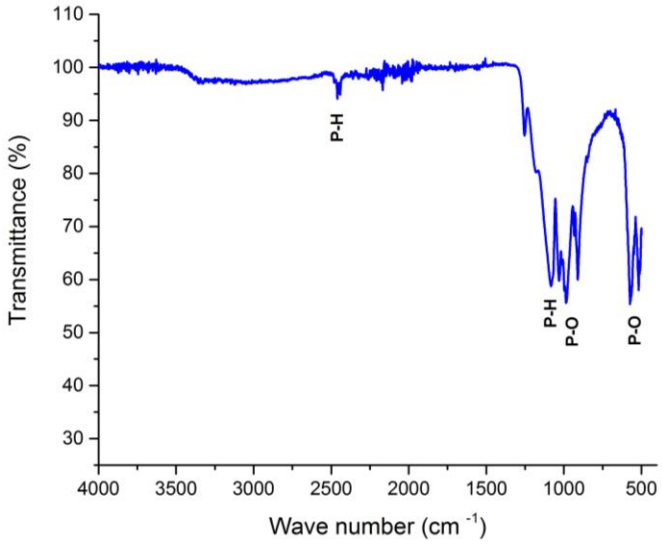

Figure 3.7. IR spectrum for **Fe-1**.

Batteries are subject to temperature increase during their lifetime, in particular due to the charge and discharge process. These changes in temperature conditions can drastically affect the performance of the battery materials, therefore it is important to understand how robust a potential battery material is under temperature stress. Thermogravimetric analysis (TGA) was carried out in order to assess the thermal stability of **Fe-1**. No weight loss was observed until 250 °C with a total weight loss of 7.3% up to 500 °C, confirming the potential use of **Fe-1** as a cathode material (Figure 3.8).

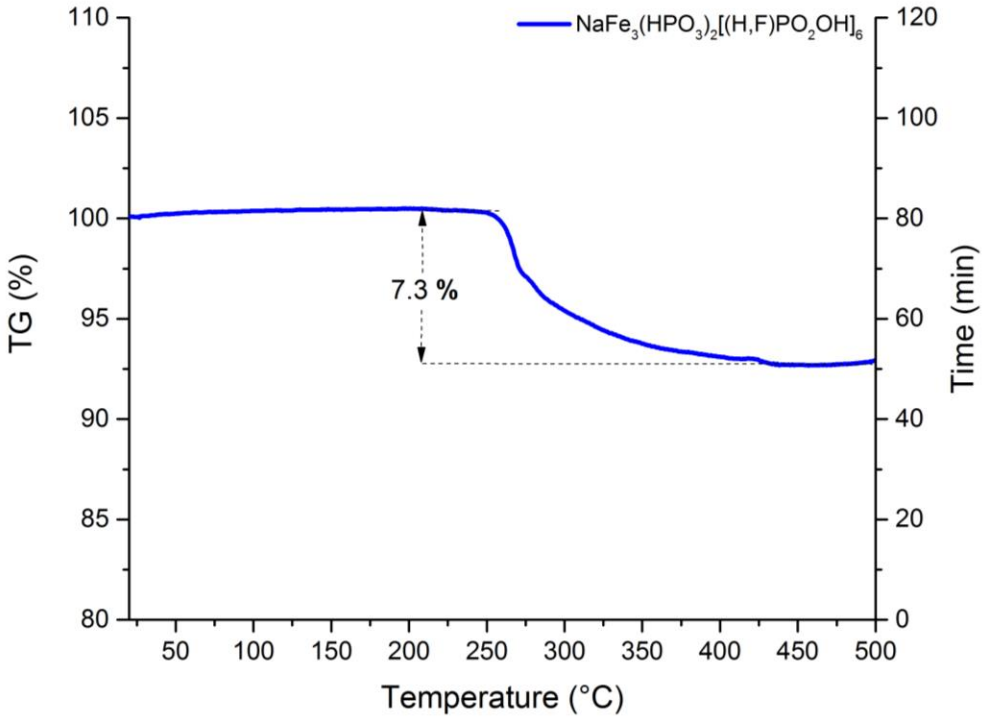

Figure 3.8. TGA curve for **Fe-1**.

3.4 Electrochemical characterisation

Phosphites are receiving considerable attention as alternative cathode materials for rechargeable batteries due to their good stability, safety and inclination to form 2D and 3D framework structures, promoting the intercalation and extraction of ions.[19-22]

Fe-1 displays a 3D framework with open channels running along all three principal directions where sodium ions reside. The net result is a complex and quite open framework, amenable to several distinct ionic migration pathways for sodium ions, suggesting good potential electrochemical performance for this material.

In order to evaluate the electrochemical activity of **Fe-1**, composite electrodes were prepared by mixing **Fe-1** with super S and Ketjen black carbons in the weight ratio 60:15:15. These chemicals were mixed for 3.5 h using a Fritsch Pulverisette 7 mill.

Then, a solution of Kynar Flex 2801 in N-methyl-2-pyrrolidone (NMP) was added as binder. The slurry obtained in this way was cast on aluminium foil using a doctor blade. The final ratio of active material, conducting carbon and binder used in the composite electrodes was 60:30:10.

The coin cell batteries built with this procedure were then subject to galvanostatic cycling tests carried out in the potential ranges of 1.7-4 V and 1.5-4.2 V at various C-rates. The load curves correspond to sodium insertion and extraction and were obtained at a rate of 10 $mAhg^{-1}$ (C/10). The data show the presence of sloping potential with an average discharge voltage of 2.5 V *vs* Na^{+}/Na for both of the potential ranges. In the 1.7-4 V range, the material reaches capacity values close to the theoretical capacity (99 $mAhg^{-1}$) over the wider voltage window and the shape on cycling is almost constant, with Coulombic efficiency close to 100%. At higher charge and discharge rates (1C, 100 $mAhg^{-1}$) there is a little reduction in capacity compared with lower rates but the cycling stability remains high (Figure 3.9, 3.10). These results indicate the stability of the **Fe-1** crystal structure and the reversible nature of sodium ions insertion.

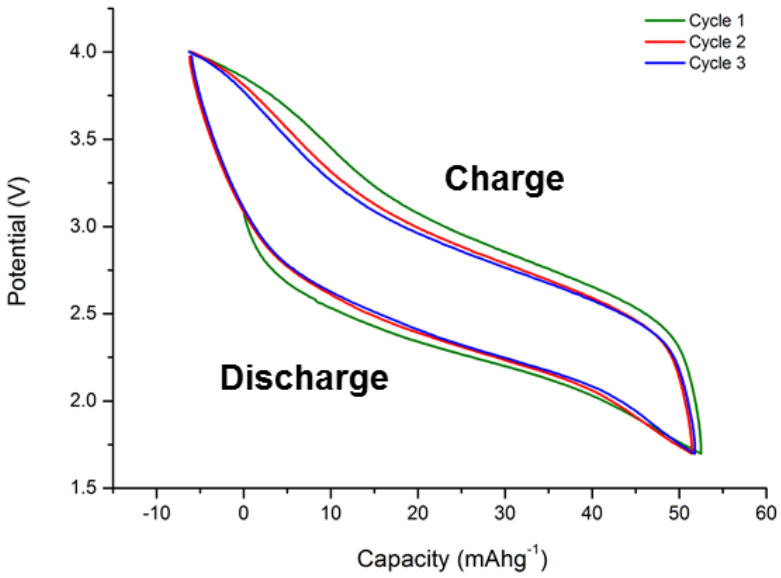

Figure 3.9. Load curves at a rate of C/10 (10 $mAhg^{-1}$) and a potential range 1.7-4 V.

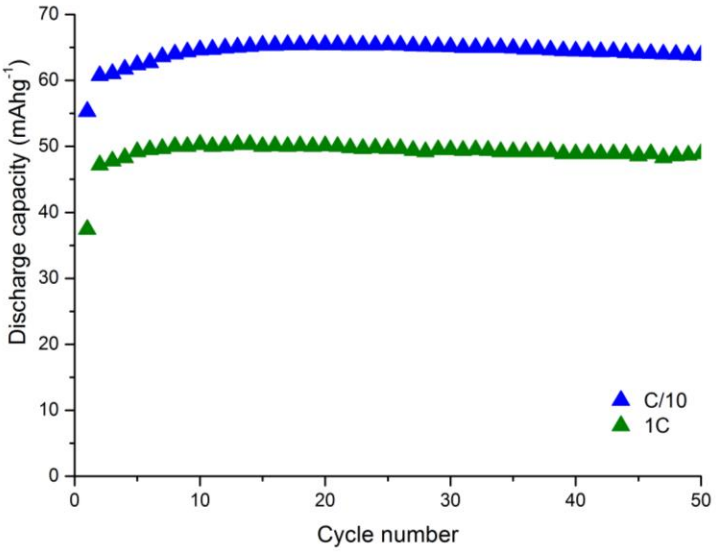

Figure 3.10. Discharge capacity *vs* cycle number for **Fe-1** at a rate of C/10 (in blue) and at a rate of 1C (in green) over the potential window 1.7-4.0 V).

In the 1.5-4.2 V voltage range, the data suggest a potential conducting carbon additive effect for some of the capacity over the larger potential range.[23] In particular, this effect can be observed in the first charge capacity that exceeds the discharge, implying the formation of Fe^{4+}. Experimental results were compared to blank experiments performed with electrodes containing only carbon black already reported in the literature. This allowed us to conclude that the additional capacity observed did not involve the formation of Fe^{4+} but was related to electrolyte/carbon black activity. Indeed, the formation of Fe^{4+} is expected at very high potentials where also significant decomposition of the electrolyte is expected.[24]

The shape on cycling is almost constant after the first cycle with capacity reaching the value of 72 $mAhg^{-1}$ over the 1.5-4.2 V voltage range (Figures 3.11). The Coulombic efficiency obtained over this voltage range shows values in the range of 70-97 $mAhg^{-1}$ (Figures 3.12) that are higher compared to the values around 52-65 $mAhg^{-1}$ obtained over the 1.7-4 V range (Figures 3.13).

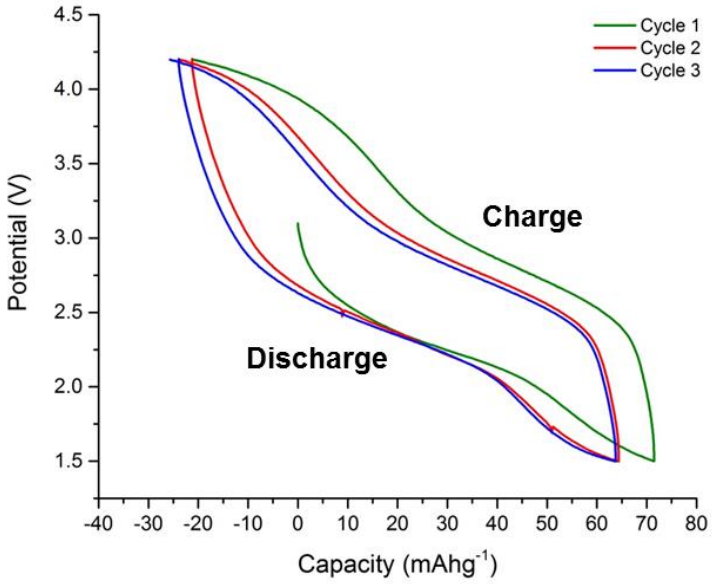

Figure 3.11. Load curves at a rate of C/10 (10 $mAhg^{-1}$) and a potential range 1.5-4.2 V.

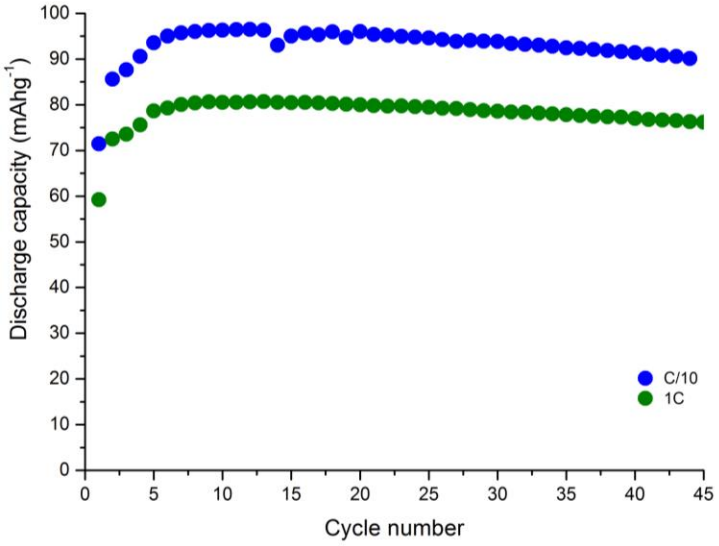

Figure 3.12. Discharge capacity *vs* cycle number for **Fe-1** at a rate of C/10 (in blue) and at a rate of 1C (in green) over the potential window 1.5-4.2 V).

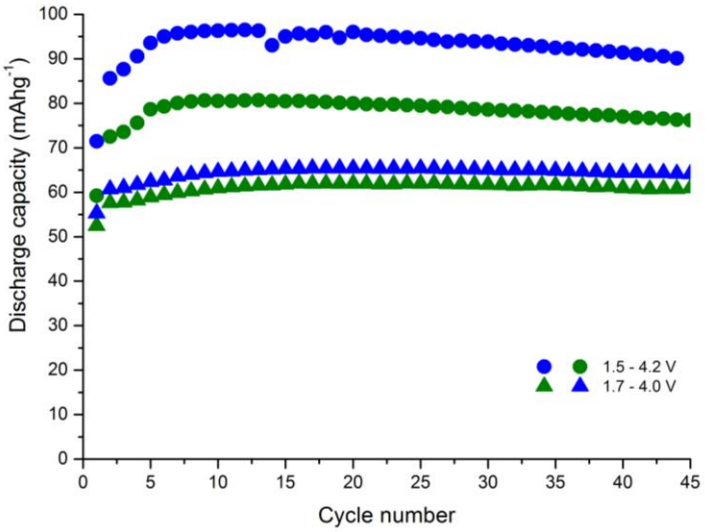

Figure 3.13. Discharge capacity *vs* cycle number for **Fe-1** at a rate of C/10 (in blue) and at a rate of 1C (in green) over the potential window 1.5-4.2 V and 1.7-4.0 V.

The stability and the structural integrity of **Fe-1** after electrochemical cycling was tested by *ex situ* powder XRD on materials obtained at the end of discharge and subsequent recharge. The powder patterns of **Fe-1** extracted from the cell after the end of charge

and end of discharge show a good fitting with the ball milled sample, confirming that the structure of **Fe-1** is stable upon sodium insertion/extraction and the 3D interconnected channel system promotes the diffusion of sodium ions without blockage, resulting in high capacity retention and good cycling stability (Figure 3.14).

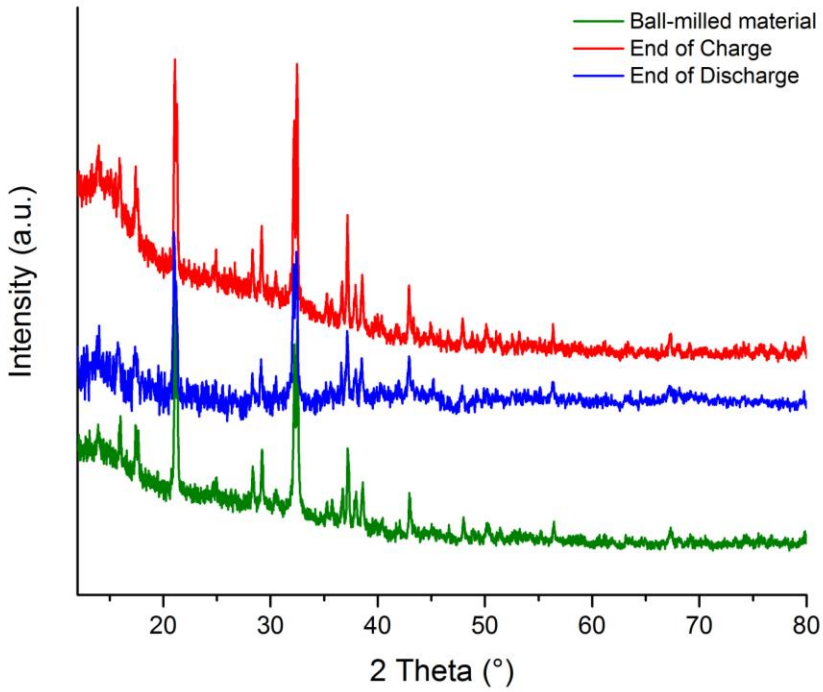

Figure 3.14. Powder X-ray diffraction patterns for **Fe-1** at various states of charge. The pattern of the ball milled material (in green) was compared with the material obtained from two different cells: one cell (in blue) was discharged to 1.7 V at a rate of 10 $mAhg^{-1}$ and the other one (in red) was discharged to 1.7 V at a rate of 10 $mAhg^{-1}$ and then recharged to 4.0 V. Initial charge at 4.0 V.

3.5 Magnetic characterisation

Magnetic super-exchange is an important mechanism through which magnetic coupling between two neighbouring cations can occur by passing through a non-magnetic

intermediate anion.[25,26,27] Super-exchange is therefore often referred to as an indirect magnetic exchange mechanism where it occurs through multiple oxygen atoms.[25-27]

In order to investigate whether super-exchange pathways are present in **Fe-1**, and given the complexity of the crystal structure, it is useful to represent the structure focussing the attention only on the key structural elements such as the framework connectivity of the Fe-P polyhedral units and the near-neighbour Fe-Fe pathways. In particular, one key structural element is a chain composed of FeO_6 octahedra. Within each chain there are two non-equivalent iron sites, both of which are octahedrally coordinated. The octahedral iron centres are connected to each other *via* corners through the bridges created by the P(3) and P(4) phosphite tetrahedral groups creating a chain repeat unit that runs along the [011] direction (Figure 3.15).

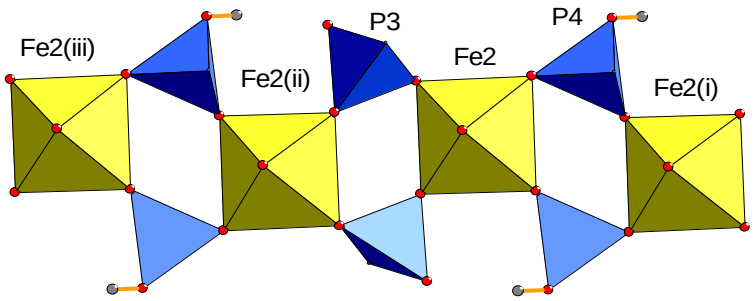

Figure 3.15. Corner-linked Fe(2)-phosphite chain. Fe-Fe distances alternate: *via* P(3) bridge 4.82 Å, *via* P(4) bridge 4.94 Å. FeO_6 octahedra in yellow, phosphite tetrahedra in blue, oxygens in red, hydrogens in grey.

Along the chains running into the [011] direction, **Fe-1** is characterised by short Fe-Fe distances (4.82-4.94 Å) compared to the rest of the structure where the Fe-Fe distance is longer, with values of 5.62 Å for Fe(2)-Fe(1) and 7.53 Å for Fe(1)-Fe(1). The iron-phosphorus distances are in the range 3.2-3.4 Å in agreement with literature (3.30 Å).[28]

Due to the short distances along the [011] direction, the iron atoms form a pathway running all through the crystal structure. This pathway is composed of chains of Fe(2)-Fe(1) atoms forming corner-linked and edge-linked triangles extended in two directions, approximately orthogonal to the Fe(2)-P chains, therefore creating in this way a super exchange network (Figure 3.16).

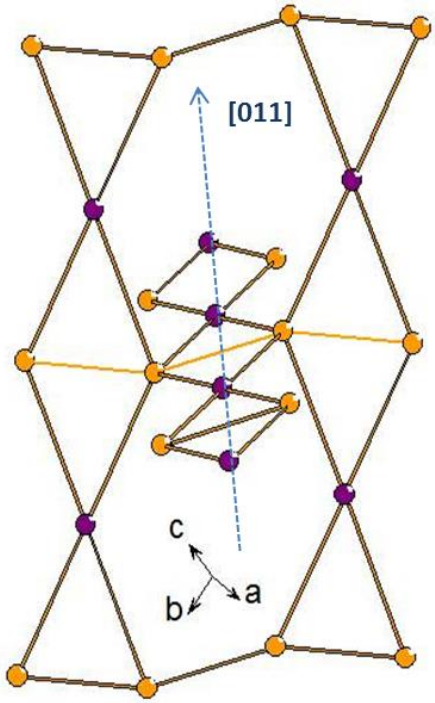

Figure 3.16. Fe-Fe sublattice showing 'diamond-like' chains extending in two dimensions. Fe(2) sites orange, Fe(1) sites purple.

In order to investigate the magnetic properties of **Fe-1** further, several measurements were performed in collaboration with Professor Alexander N. Vasiliev and co-workers at the Faculty of Physics of the Moscow State University. In particular, measurements of the susceptibility (χ), magnetization (M) and specific heat (C_p) were conducted in the temperature range of 2-300 K in order to understand the magnetic behaviour of this material as function of temperature.

The zero field cooled (ZFC) magnetic susceptibility measured in an applied field of 1 T exhibits a sharp upturn at T_C = 9.4 K, revealing the formation of a magnetically ordered state below this temperature (Figure 3.17).[29]

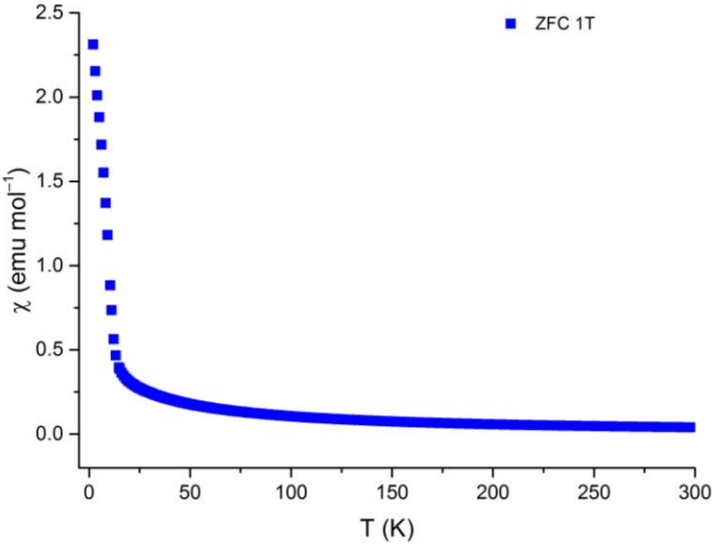

Figure 3.17. Susceptibility plot of **Fe-1** between 25 and 300 K.

It is possible to model the inverse magnetic susceptibility with a modified Curie-Weiss law over the range 40-300 K represented in Equation 3.1.

$$\chi = \chi_0 + \frac{C}{T - \Theta} \qquad \text{Eq. 3.1}$$

The temperature-independent term is represented by χ_0 and it is equal to -5 x 10^{-4} emu/mol. The Curie constant (C) and the Weiss temperature (Θ) show values of 12.6 emu K/mol and -22 K, respectively (Figure 3.18).

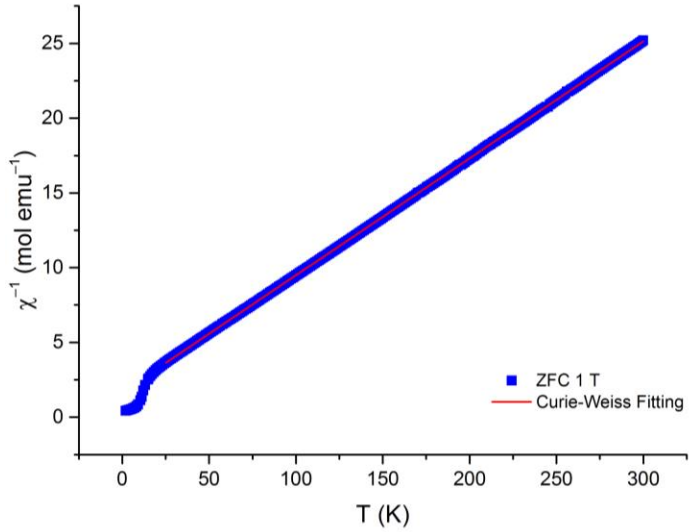

Figure 3.18. Inverse susceptibility plot of **Fe-1** with red line indicating the Curie-Weiss fit between 25 and 300 K.

The Curie constant is proportional to the number of magnetic ions, *n*, via the expression represented in Equation 3.2.

$$C = ng^2S(S+1)\mu_B{}^2N_A/3k_B \qquad \text{Eq. 3.2}$$

The Bohr, Avogadro and Boltzmann constants are represented by μ_B, N_A and k_B. The effective magnetic moment obtained from the above *C* value (μ_{eff} = 10.04 μ_B) compares well with the theoretical estimation according to the formula represented in Equation 3.3.

$$\mu_{theor}{}^2 = ng^2\mathrm{S(S+1)}\mu_B{}^2 \qquad \text{Eq. 3.3}$$

This results in $\mu_{theor} \approx 10.22\ \mu_B$ for three high-spin S = 5/2 Fe^{3+} ions per formula unit with average value g = 1.993.

The negative sign of the Weiss temperature indicates the dominance of antiferromagnetic exchange interactions. The low-temperature peak of the magnetic susceptibility is the sign of a spontaneous magnetisation in **Fe-1** at temperature below the T_c value of 9.4 K. Also, the value of the Curie constant is consistent with the g factor (with g~ 2) for 3 Fe^{3+} ions per formula unit in the S=5/2 high spin state and the negative value of the Weiss temperature indicates the predominance of antiferromagnetic exchange interactions in this system. On the other hand, the zero field heat capacity data show a sharp peak at T_c consistent with the magnetic susceptibility, which again indicated a magnetic transition at ~ 9 K. Below this temperature, the heat capacity follows a linear temperature dependence typical for a two-dimensional ferromagnetic behaviour.[30]

In contrast with the behaviour of the susceptibility which shows a sharp peak at T_c, the specific heat (C_p) shows a broad distribution at T_c when a weaker magnetic field is applied (B = 3, 6, 9 T), suggesting a redistribution of magnetic entropy over a wide range of temperature upon application of the magnetic field. Indeed, when a magnetic field equal to B = 3, 6 and 9 T is applied the data measured are basically very similar, reflecting the persistence of the magnetic state of **Fe-1** at the plateau. This means that the magnetic ordered state is spread out by the application of an external magnetic field, a typical behaviour for ferromagnetic or ferrimagnetic systems (Figure 3.19).[30]

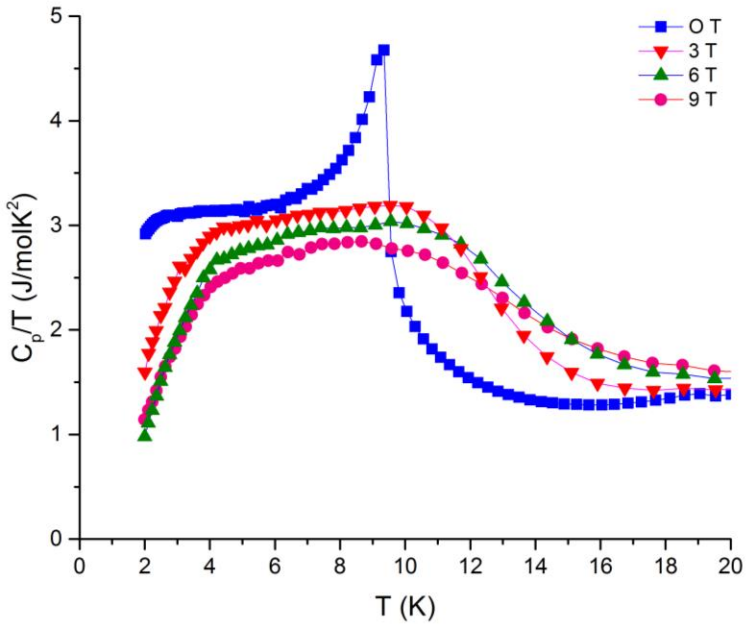

Figure 3.19. The magnetic specific heat C_p/T at different magnetic fields for **Fe-1**.

If a magnetic material is placed in a magnetic field, this can lead to an increase or decrease in terms of the flux density. For example, diamagnetic materials reduce the density of lines of force whereas paramagnetic materials increase the flux density. The field of the sample is called magnetisation (*M*) and its contribution to the magnetic flux density (*B*) have been investigated in static magnetic field up to B = 9 T and in pulsed magnetic field up to B = 30 T at T = 2 K. The magnetisation values rapidly reach a plateau of 4.3 μ_B at 1.8 T that continues until 8 T and reaches saturation of 13 μ_B at 27 T. Noticeably, the magnetisation as a function of the field shows mostly linear behaviour between 8 T and 27 T (Figure 3.20).

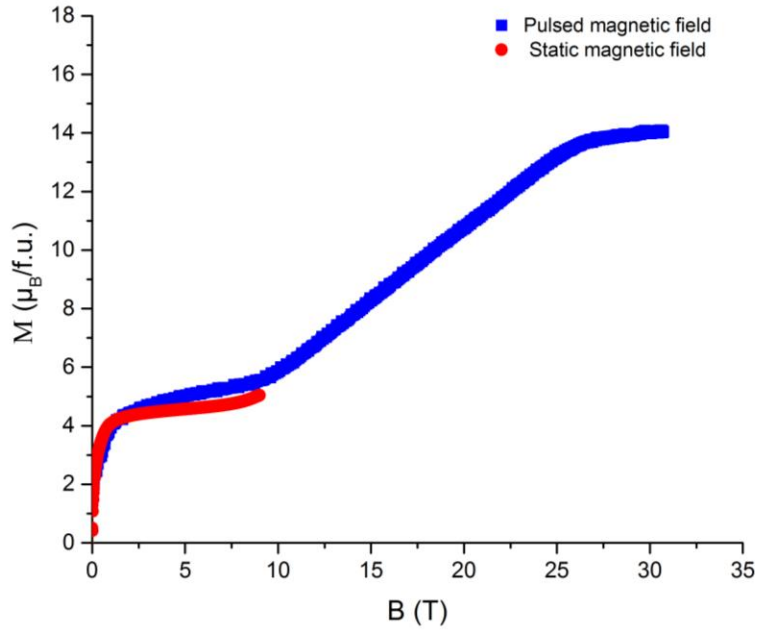

Figure 3.20. The field dependencies of the magnetisation *M* in static and pulsed magnetic field at T = 2 K for **Fe-1**.

The conventional response of a magnetic material in an applied field is related to the increase of its magnetisation as a function of the field. When the magnetisation reaches its saturated value, M_s, all the spins in the system are aligned with the field. Therefore, the linear behaviour seen in the field dependence of the magnetisation data between 8 T and 27 T is quite common and the slope of the linear part gives a measure of the magnetic susceptibility in that field range. In addition, in **Fe-1** it is possible to notice a pronounced plateau in the magnetisation up to ~ 8 T. The magnetisation of the sample in that plateaued state is equal to 4.3 μ_B, which is approximately 1/3 of the fully saturated magnetic moment reached at higher fields. Therefore, the system demonstrates an unusual 1/3 magnetisation plateau. This behaviour can arise from a ferrimagnetic ordering of the spins in a material that is stabilised by the applied field. However, as the field strength continues to increase, it will become more and more favourable for the

spins to align themselves with that field. In the case of **Fe-1**, the ferrimagnetic plateau state likely arises from the very complex interplay of six different exchange couplings that compete with each other. Such ferrimagnetic magnetisation plateaus are quite common in magnetic systems with competing exchange interactions (frustrated magnets), but what sets this system apart is that the zero field ground state also appears to be ferrimagnetic. So the 1/3 plateau is essentially a manifestation of frustrated nature of the magnetic interactions in this system. Further evidence for this frustration is that the ferrimagnetic ordering transition T_N ~ 9.5 K is somewhat lower in energy that the energy scale for antiferromagnetic exchange set by the Weiss constant $|\theta|$ ~ 22 K.

In order to confirm magnetic super-exchange couplings and obtain a more precise crystal structure in terms of positions for the hydrogen atoms, it was useful to obtain computational (DFT) calculations conducted by Professor A. Tsirlin and co-workers based on the experimentally determined CIF and a structure optimisation. This resulted in more realistic O-H bond lengths since H atoms are notoriously tricky to see with X-rays. The resulting O-H distances have values around 1.0 Å, compared to the values of 0.73-0.78 Å that have been reported experimentally and the P-H bonds have uniform values of 1.40 Å in the HPO_3 groups (Table 3.3).

Table 3.3. Hydrogen positions in **Fe-1** obtained from DFT. The last column shows the P and O atoms linked to hydrogen atoms.

	x/a	*y/b*	*z/c*	
H1	0.92517	0.35044	0.95535	P3
H2	0.63676	0.46346	0.44432	P4
H3	0.55411	0.83333	0.92131	P2
H4	0.99043	0.75964	0.32566	P1
H5	0.77954	0.94086	0.30216	O9
H6	0.43336	0.43748	0.73360	O11
H7	0.74926	0.96581	0.76451	O12

The DFT optimised structure has been used also to identify and calculate different exchange coupling pathways (*Ji*) running through the **Fe-1** crystal structure. All of them are antiferromagnetic because all $Fe^{3+}O_6$ octahedra are connected to each other by non-magnetic phosphite groups and the exchange couplings involve multiple oxygen atoms (Table 3.4).

Table 3.4. Isotropic exchange couplings (*Ji*) in **Fe-1**.

	z_{Fe1}, z_{Fe2}	Fe-Fe distance (Å)	J_i (K)	J_i (K), rescaled
J_1	0, 1	4.821	0.6	0.4
J_2	0, 1	4.943	2.4	1.6
J_3	2, 1	5.620	2.2	1.5
J_4	1, 1	5.788	2.0	1.3
J_5	2, 2	5.926	0.4	0.3
J_6	2, 2	6.317	2.3	1.5

Looking at the values of the super-exchange couplings, it is possible to distinguish four stronger couplings (2.0 K in J_2, J_3, J_4, J_6) and two weaker couplings (0.5 K in J_1 and J_5).

The four stronger ones form magnetic planes along the [101] direction and the two weaker ones connect these planes to each other, forming a 3D lattice (Figure 3.21 and Figure 3.22).

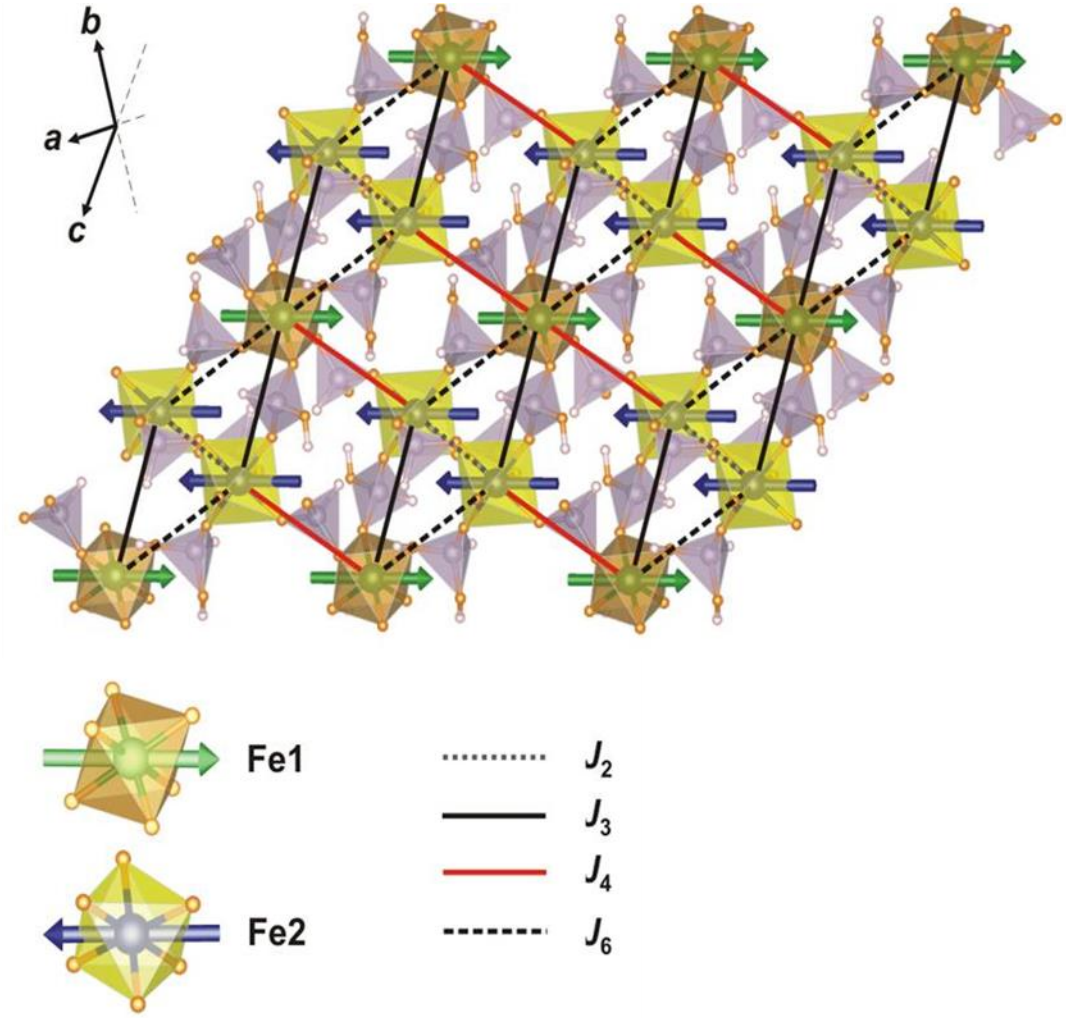

Figure 3.21. Microscopic magnetic model of **Fe-1**, showing magnetic planes formed by the four stronger couplings J_2, J_3, J_4, and J_6; Fe(1) octahedra in brown, Fe(2) octahedra in yellow, phosphite tetrahedra in grey.

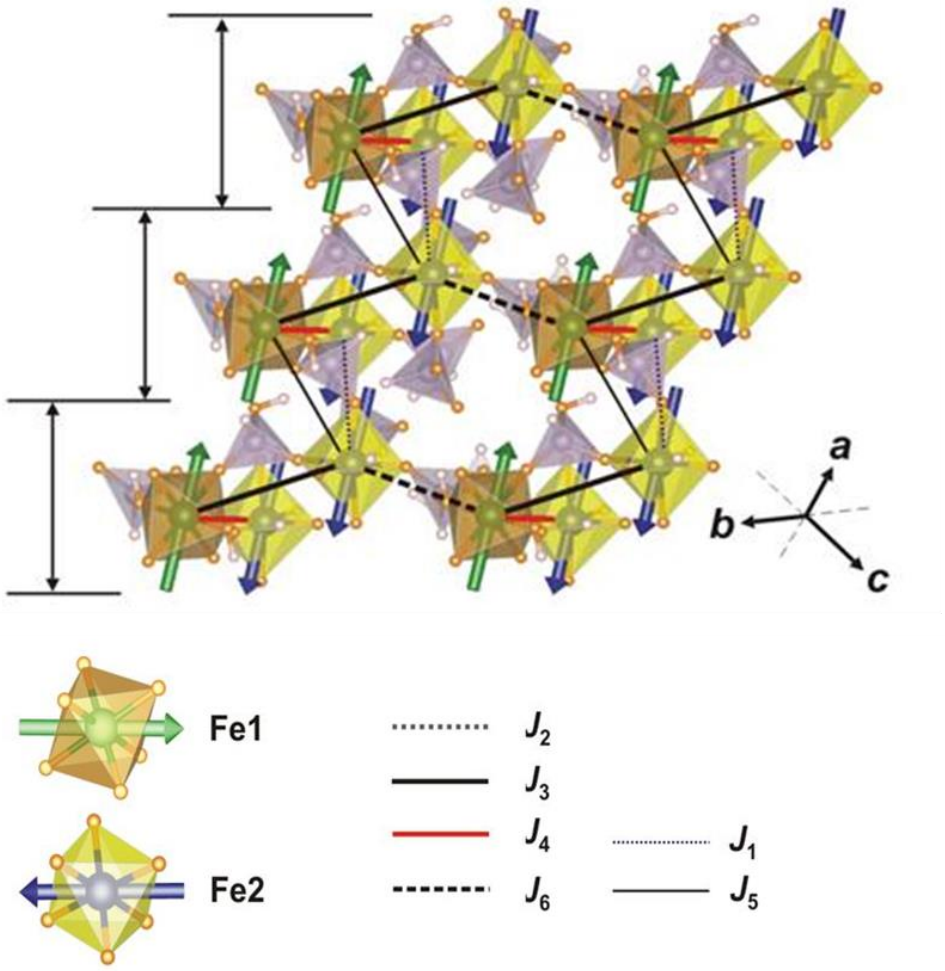

Figure 3.22. Microscopic magnetic model of **Fe-1**. The VESTA software was used for crystal structure visualization;[31] Fe(1) octahedra in brown, Fe(2) octahedra in yellow, phosphite tetrahedra in grey.

Three of the stronger couplings (J_2, J_3, J_6) form triangular units in the microscopic magnetic model of **Fe-1** and show frustrated behaviour. In contrast with what is typically reported in literature about frustrated triangular units, where the two strongest couplings work in order to stabilise antiparallel spins and the weakest coupling is left with the parallel spin arrangement, **Fe-1** shows a different behaviour.[29] In particular, the magnetic order is stabilised by the weaker couplings of the triangular unit (J_3 and J_6),

resulting in a ferrimagnetic order within the plane with parallel spins inside each of the Fe-O sublattice and antiparallel ones between the Fe-O sublattices.

Also, the weaker interplane couplings (J_1 and J_5) together with the remaining stronger intraplane coupling (J_4) form triangular loops and show frustrated behaviour. In this case the magnetic order is stabilised by the interplane coupling J_5, which is weaker than J_1 but it is twice as abundant within the structure, giving a large contribution in terms of stabilisation energy. In particular, J_5 is working diagonally in the structure in order to stabilise ferrimagnetic order between the planes.

These exchange couplings have been used to run a Monte-Carlo simulation of the magnetisation and susceptibility data, which is in agreement with the susceptibility data and confirms the macroscopic ferrimagnetic configuration characterised by 1/3*M* total magnetisation. If the magnetic order was instead stabilised by the weaker J_1 coupling, the net moments of the neighbouring layers could cancel each other, resulting in an overall antiferromagnetic order.

3.6 Chapter conclusions

In this chapter a novel iron fluorophosphite compound of formula $NaFe_3(HPO_3)_2[(H,F)PO_2OH)_6]$ has been described. The phase has been synthesised by a dry, low-temperature and cheap synthetic route. This novel crystal structure exhibits an interesting 3D framework with FeO_6 octahedra corner-sharing with HPO_3 and HPO_2OH tetrahedra. Partial replacement of some hydrogen positions by fluorine atoms has been confirmed by EDX analysis and single crystal refinements. Open channels are present in the structure and run along all three dimensions, with the sodium ions residing inside the open channels coordinated to six different HPO_2OH groups *via* the oxygen atoms of

the P-O-H moieties. One of the repeated key structural elements is the chain of $Fe(2)O_6$ octahedra that is linked *via* corners through bridging phosphite groups (P(3) and P(4)). These chains run along the [011] direction and are linked via P(1) and P(2) phosphite groups.

Fe-1 shows interesting electrochemical properties. It is stable upon sodium insertion/extraction and the 3D interconnected channel system promotes sodium ions diffusion without blockage, reaching the observed high capacity retention, good cycling stability and Coulombic efficiencies close to 100%. In addition, **Fe-1** shows an average discharge voltage of 3 V and an experimental capacity of 60 $mAhg^{-1}$ close to the theoretical value.

Fe-1 is also characterised by unusual magnetic properties for iron-based structures. The 1/3*M* plateau observed in the magnetisation is typical for ferrimagnetic phases stabilised by an external magnetic field. The thermodynamic measurements reveal a typical ferrimagnetic transition at T_c = 9.4 K. Its magnetic subsystem, represented by Fe^{3+} ions in two crystallographical inequivalent positions in a triangular arrangement, exhibits both three-dimensional and one-dimensional trends in the paramagnetic state ($T > T_c$) and spontaneous magnetization in the magnetically ordered state ($T < T_c$).

In conclusion, **Fe-1** is a new 3D framework structure with both interesting electrochemical and magnetic properties. The relatively simple synthesis, more economically available materials, high capacity retention and efficiency of this cathode material could open the way for applications in the second generation sodium battery systems.

The entire work and more detailed measurements have been accepted for publication in *Inorganic Chemistry* and *Physical Review B*:

1. **I. Munaò**, E. A. Zvereva, O. S. Volkova, A. N. Vasiliev, A. R. Armstrong, P. Lightfoot, *Inorg. Chem.*, 2016, **55**, 2558.

2. A. N. Vasiliev, O. S. Volkova, E. A. Ovchenkov, E. A. Zvereva, **I. Munaò**, L. Clark, P. Lightfoot, E. L. Vavilova, S. Kamusella, H.-H Klauss, J. Werner, C. Koo, R. Klingeler, A. A. Tsirlin, *Phys. Rev. B*, 2016, **93**, 134401.

3.7 References

1. P. Young-Uk, S. Dong-Hwa, Seo, K. Hyungsub, K. Jongsoon, L. Seongsu, K. Byoungkook, K. Kisuk, *Adv. Funct. Mater.*, 2014, **24**, 4603.
2. P. Young-Uk, S. Dong-Hwa, K. Hyung-Soon; Byoungkook, K. Jongsoon, K. Haegyeom, K. Inkyung, Y. Han-Ill, K. *J. Am. Chem. Soc.*, 2013, **135**, 13870.
3. P. Young-Uk, S. Dong-Hwa, K. Byoungkook, H. Kun-Pyo, K. Hyungsub, L. Seongsu, Lee; R.A. Shakoor, K. Miyasaka, J.M. Tarascon, K. Kang, *Sci. Rep.*, 2012, **2**, 704.
4. P. Serras, V. Palomares, J. Alonso, N. Sharma, J.M. López del Amo, P. Kubiak, M.L. Fdez-Gubieda, T. Rojo, *Chem. Mater.*, 2013, **25**, 4917.
5. P. Serras, V. Palomares, A. Goñi, I. Gil de Muro, P. Kubiak, L. Lezama, T. Rojo, *J. Mater. Chem.*, 2012, **22**, 22301.
6. P. Serras, V. Palomares, A. Goñi, P. Kubiak, T. Rojo, *J. Power Sources*, 2013, **241**, 56-60.
7. R.K.B. Gover, A. Bryan, P Burns, J. Barker, *Solid State Ionics*, 2006, **177**, 1495.
8. J. Barker, R.K.B. Gover, P. Burns, A. Bryan, M.Y. Saidi, J.L. Swoyer, *Journal of Power Sources*, 2005, **146**, 516.
9. J.M. Le Meins, M.P. Crosnier-Lopez, A. Hemon-Ribaud, G. Courbion, *J. Solid State Chem.*, 1999, **148**, 260.
10. L.A. Groat, B. C. Chakoumakos, D.H. Brouwer, C.M. Hoffman, C. A. Fyfe, H. Morell, A.J. Schultz, *Am. Miner.*, 2003, **88**, 195.
11. Y. Makimura, L.S. Cahill, Y. Iriyama, G.R. Goward, L.F. Nazar, *Chem. Mater.*, 2008, **20**, 4240.

12. T.N. Ramesh, K.T.Lee, B.L. Ellis, L.F. Nazar, *Electrochem. Solid-State Lett.*, 2010, **13**, 43.
13. B.L. Ellis, W.R.M. Makahnouk, W.N. Rowan-Weetaluktuk, D.H. Ryan, L.F. Nazar, *Chem. Mater.*, 2010, **22**, 1059.
14. R.E. Morris, M.P Attfield, A.K. Cheetham, *Acta Crystallogr. C*, 1994, **50**, 473.
15. R. Gond, G. Shinde, P. Barpanda., Abstract MA2016-02 720, ECS Meeting abstracts, 2016.
16. X. Lin, Y. Zhao, Y. Dong, Q. Kuang, Z. Liang, D. Yan, X. Liua, *Materials Science and Engineering B*, 2015, **197**, 58.
17. J. Ensling, P. Gutlich, R. Schmidt, R. Kniep, *Inorg. Chem.*, 1994, **33**, 3595.
18. M. Sghyar, J. Durand, L. Cot, M. Rafiq, *Acta Crystallogr. C*, 1991, **47**, 2515.
19. N.E.Brese, M. O'Keeffe, *Acta Crystallogr.B.*, 1991, **47**, 192.
20. J. Loub, *Acta Crystallogr.B.*, 1991, **47**, 468.
21. K.Nakamoto, *Infrared and Raman Spectra of Inorganic and Coordination Compounds Part A*, John Wiley &Sons, 2009.
22. T. Rojo, J.L. Mesa, J. Lago, B. Bazan, J.L. Pizarro, M.I. Arriortua, *J. Mater. Chem.*, 2009, **19**, 3793.
23. E.K. Sichel, *Carbon black-polymer composites: the physics of electrically conducting composites.* Vol. 3. Marcel Dekker Inc, 1982.
24. J. Nava-Avendano, M.E. Arroyo-de Dompablo, C. Frontera, J.A. Ayllòn, M.R. Palacìn, *Solid State Ion.*, 2015, **278**, 106.
25. T. Moriya *Phys. Rev.*, 1960, **91**, 120.
26. P. W. Anderson, *Phys. Rev.*, 1959, **2**, 115.

27. U. Bossek, K. Wieghardt, B. Nuber, J. Weiss, J., *Angew. Chem. Int. Ed. Engl.*, 1990, **29**, 1055.

28. U. Hoppe, M. Karabulut, E. Metwalli, R.K. Brow, P. Jovari, *J. Phys. Condens. Matter*, 2003, **15**, 6143.

29. S. Blundell, *Magnetism in Condensed Matter*, Oxford University Press, Oxford, 2001.

30. K.M. Ranjith, R. Nath, M. Skoulatos, L. Keller, D. Kasinathan, Y. Skourski, A.A. Tsirlin, *Phys. Rev. B*, 2015, **92**, 094426.

31. K. Momma, F. Izumi, *J. Appl. Crystallogr.*, 2011, **44**, 1272.

Chapter 4

$Fe_2(HPO_3)_3$: a New Potential Cathode Material for Sodium Batteries

4.1 Introduction

A lower number of oxygens, the difference in the oxidation state of the phosphorous atom and a lower charge may lead to phosphite materials as new materials for sodium batteries. Studies of transition-metal phosphites have indicated that interesting and novel structures can be produced using hydrothermal methods, including structures containing channels and cavities, particularly interesting for the intercalation and extraction of sodium ions for electrochemical purposes.[1,2,3]

The iron phosphite compound $Fe_2(HPO_3)_3$ (hereinafter abbreviated "**Fe-2**") reported in this chapter has been synthesised by hydrothermal synthesis and fully characterised. The electrochemical and magnetic properties of **Fe-2** have been studied in depth in order to assess its potential use as a cathode material for a new generation of sodium batteries.

4.2 Material synthesis

Fe-2 was prepared using hydrothermal synthesis reacting NaF (1 mmol) with Fe_2O_3 (1 mmol) and H_3PO_3 (0.122 mmol). A 1:1 ratio of water (0.5 ml, 2.77 x 10^{-2} mol) and methanol (0.5 ml, 1.23 x 10^{-2} mol) was added to the resultant solution. This reaction mixture was sealed in a Teflon-lined stainless steel autoclave and heated to 110 °C for 3 days. The reaction was cooled to room temperature and light blue air-stable prismatic chip crystals were recovered by filtration from a minor aqueous phase.

4.3 Structural characterisation

Fe-2 crystals are well-faceted light blue needle-shaped blocks with a particle size of about 200 μm (Figure 4.1)

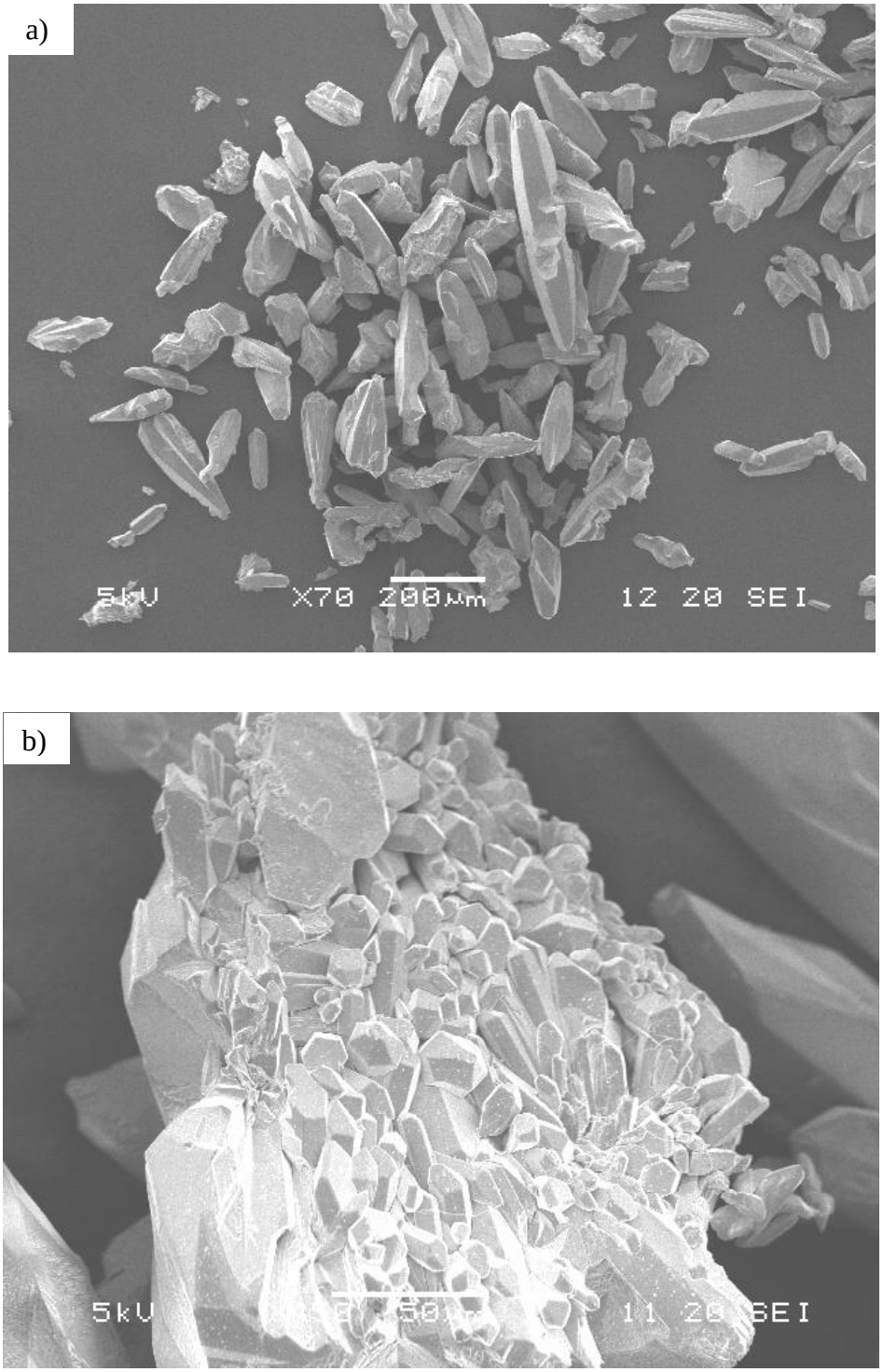

Figure 4.1. a) SEM picture and b) zoom-in of typical **Fe-2** crystals.

Analysing the single crystal diffraction data, **Fe-2** adopts a hexagonal structure in the P 6_3/m space group (Table 4.1).

Table 4.1. Crystallographic data of **Fe-2**.

Molecular formula	**$Fe_2(HPO_3)_3$**
Formula Mass (amu)	351.63
Crystal system	Hexagonal
Space group	P 6_3/m
a	8.027(4) Å
b	8.027(4) Å
c	7.397(4) Å
α	90.000(0)°
β	90.000(0)°
γ	120.000(0)°
V (A^3)	412.76 (4)
Z	2
ρ (calcd) (g/cm^3)	2.150
Temp (K)	173 (2)
F (000)	255
μ (mm^{-1})	3.895 (calculated)
R_{int}	0.0699
R_1/wR_2 (I >2σ)	0.0370, 0.06136
R_1/wR_2 (all data)	0.0427, 0.0690
Reflections number gt	155
Reflections number total	253
GOF on F^2	5.142

This structure is isostructural with the previously reported $M_2(HPO_3)_3$ (M = Fe,[4.5] Sc,[6] Al,[1] Ga[1]) phases. In particular, the **Fe-2** structure has been previously reported by Sghyar *et al.*,[5] where the crystalline compound was obtained by an isothermal slow evaporation from an aqueous solution containing 20% of Fe_2O_3, 30% of H_3PO_3 and 50% of water at 363 K.

Fe-2 exhibits a 3D framework crystal structure with Fe_2O_9 dimer chains running along the *c*-direction. Each Fe_2O_9 dimer is composed of two face-sharing FeO_6 octahedra and each group, composed of two adjacent Fe_2O_9 dimers, is bridged to the next one by three $(HPO_3)^{2-}$ anions forming chains parallel to the *c*-axis. A key aspect of this structure is the hexagonal open channel present along the *c*-axis and in centre of the structure. This channel is surrounded by six groups of face-sharing FeO_6 octahedra and hydrogen atoms of the HPO_3^{2-} anions that are around the 6_3 axis. The net result is a quite open framework structure with a Fe-Fe distance in the 8.03-9.98 Å range (Figure 4.2, Figure 4.3).

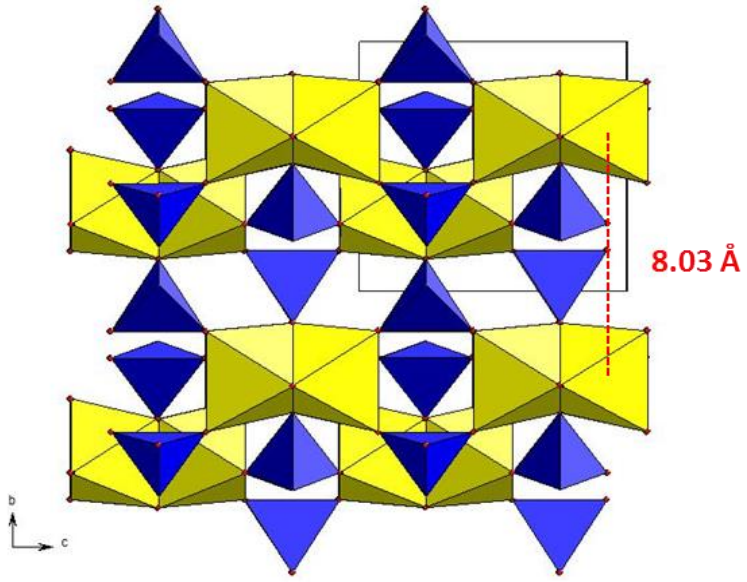

Figure 4.2. Polyhedral representation of the **Fe-2** crystal structure along the *a*-axis. FeO_6 octahedra in yellow, phosphite tetrahedra in blue. Fe-Fe distance equal to 8.03 Å.

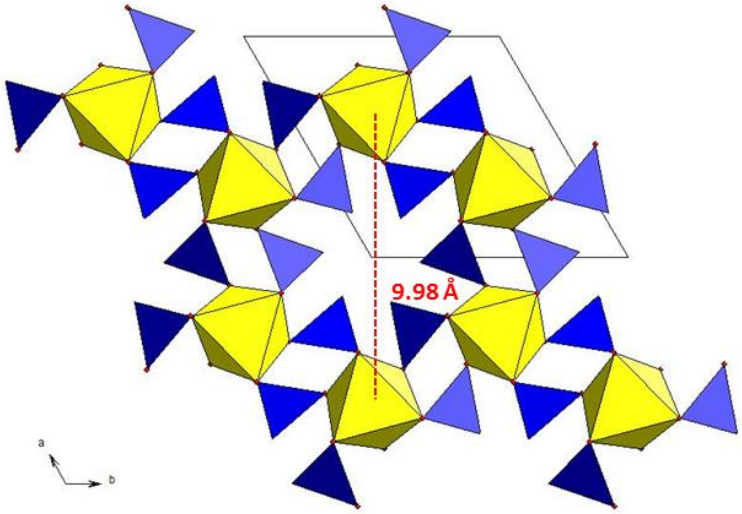

Figure 4.3. Polyhedral representation of the **Fe-2** crystal structure along the *c*-axis. FeO_6 octahedra in yellow, phosphite tetrahedra in blue. Fe-Fe distance equal to 9.98 Å.

The single crystal data were analysed refining all non-H atoms. All H-atoms were located by Fourier methods and refined without constraints. In order to investigate the

chemical composition and exclude the presence of any fluorine in the final structure solution, Energy-dispersive X-ray spectroscopy (EDX) was carried out. The qualitative EDX analysis confirmed the presence of oxygen, sodium, phosphorous and iron in the **Fe-2** compound (Figure 4.4).

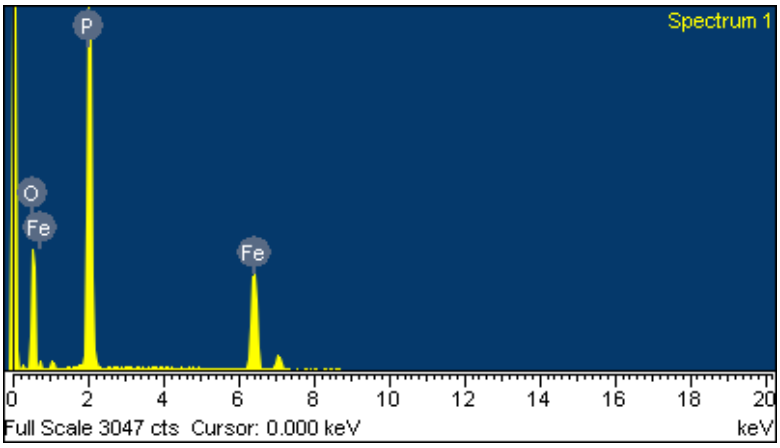

Figure 4.4. EDX spectrum for **Fe-2**.

The iron site is occupied by Fe^{3+} with octahedral coordination and bond lengths in the normal range for Fe^{3+} (1.912 -2.173 Å).[1-5] There are no long-range Fe-O-Fe links and the dimers are connected three-dimensionally *via* phosphite groups. In order to confirm the iron oxidation state and the location of OH groups, Bond Valence Sum (BVS) calculations were carried out. The Bond Valance parameters relate the bond valances and the bond lengths (see Chapter 2, Section 2.3). The data obtained from the BVS calculations for **Fe-2** using the Bond Valance parameters reported in literature for the Fe-O bond (1.759 Å) and the P-O bond (1.604 Å) are in good agreement with the hypothesised valence state of the iron (3+) and of the phosphorous (3+) atoms. Moreover, the negligible difference between the hypothesised valance state and the

BVS calculations allows to consider of minimal size the disorder and the partial occupancy effects in the **Fe-2** structure (Table 4.2).[9,10]

Table 4.2. Selected bond lengths and bond valence sums for **Fe-2**.

		Bond length (Å)	Bond valence
Fe1	O1 x3	2.173(3)	0.329
	O2 x3	1.912(4)	0.665
			∑ **2.983**
P1	O1	1.502(4)	1.372
	O2 x2	1.661(4)	0.891
			∑ **3.154**

The sample purity was verified by Powder X-ray diffraction (PXRD) experiments. A good level of purity of the sample is confirmed by the good match of the simulated and experimental pattern. Extra peaks around 17° and 33° are typical of the Teflon support used to carry on the powder diffraction measurement (Figure 4.5).

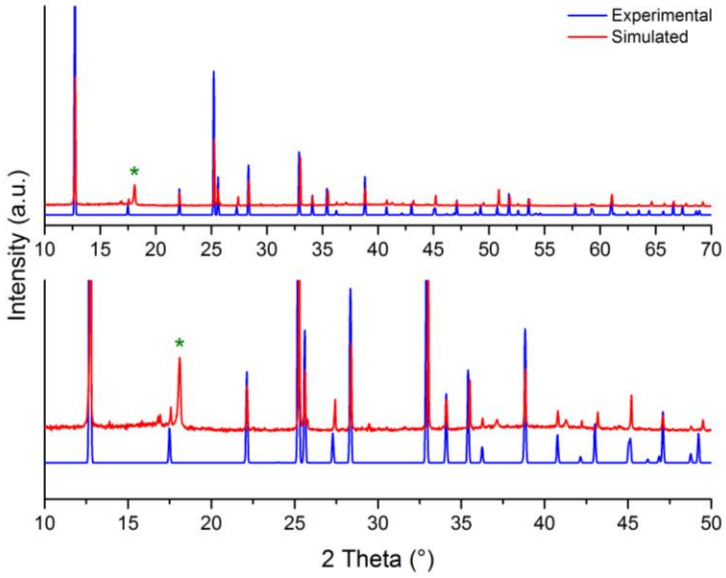

Figure 4.5. Observed and simulated PXRD pattern for **Fe-2**: Experimental patterns in blue and calculated patterns from single crystal data in red; full pattern on the top,

zoom-in of low angle region on the bottom. Peaks arising from the Teflon sample mounting are marked with an asterisk.

The presence of P-H bonds in the structure was analysed by Infrared spectroscopy (IR). The IR spectrum of **Fe-2** mainly consists of strong absorption peaks due to P-H and P-O bonds stretching of the phosphite moiety confirming the presence of P-H bonds in the structure. Typical P-H stretch are present around 2450 cm^{-1} and strong PO_3 stretching modes are situated in the range of 950-1150 cm^{-1} (Figure 4.7).[11]

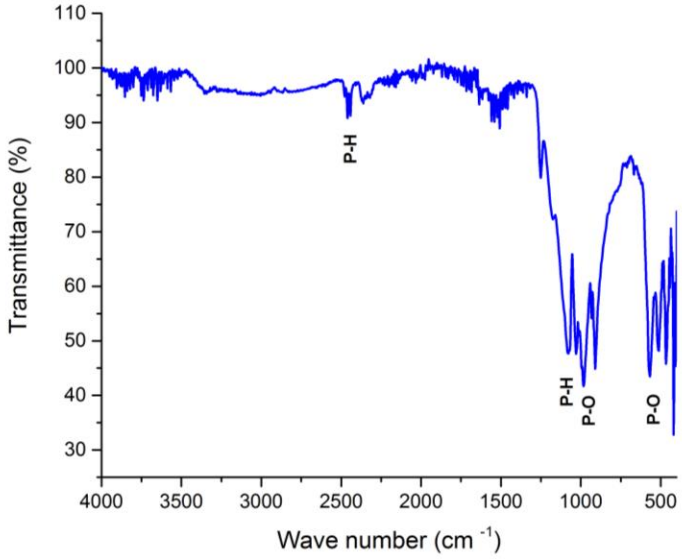

Figure 4.7. IR spectrum for **Fe-2**.

The temperature increase during the lifetime of a battery due to the charge and discharge process can affect the efficiency of battery materials. Thermogravimetric analysis (TGA) was carried out in order to test the performance of **Fe-2** under temperature stress. The data show good stability of the **Fe-2** structure with increase in

temperature, with a weight loss of 2% up to 250 °C and a total weight loss of 9.6% below 500 °C (Figure 4.8).

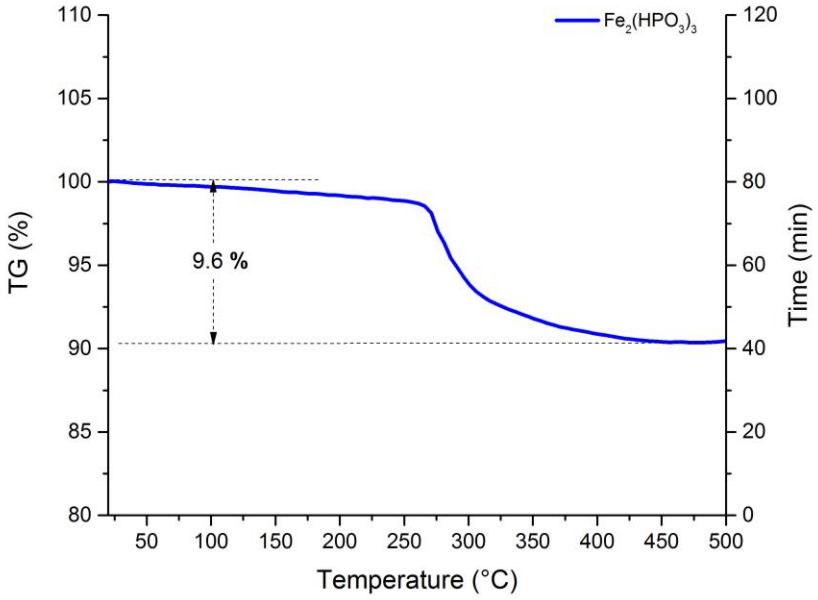

Figure 4.8. TGA curve for **Fe-2**.

4.4 Electrochemical characterisation

Phosphites show good stability, safety and are key components of battery materials by contributing to the formation of 3D framework structures.[12-15]

Fe-2 displays a 3D framework structure with a weak but significant electron density inside the 3 Å diameter hexagonal open channel present along the *c*-axis of the structure suitable for cationic intercalation (Figure 4.3).[8]

In order to evaluate the electrochemical activity of **Fe-2**, composite electrodes were prepared by mixing **Fe-2** with super S carbon and Ketjen black carbon in the weight ratio 60:15:15. These chemicals were mixed for 3.5 h using a Fritsch Pulverisette 7 mill.

A solution of Kynar Flex 2801 in N-methyl-2-pyrrolidone (NMP) was then added as binder. The slurry obtained in this way was then cast on aluminium foil using a doctor blade. The final ratio of active material, conducting carbon and binder used in the composite electrodes was 60:30:10.

The coin cell batteries built with this method were then subject to galvanostatic cycling tests carried out in the potential ranges 2-4 V and 2-4.2 V at various C-rates. The load curves corresponding to sodium insertion and extraction were obtained at a rate of 10 $mAhg^{-1}$ (C/10). The sloping potential suggests an average discharge voltage around 2.5 V *vs* Na^{+}/Na for both of the potential ranges. However, even if the material exhibits good capacity retention, the capacity values reached are far from the theoretical capacity (152 $mAhg^{-1}$) and the Coulombic efficiency is low, being close to 25%, using both of the voltage ranges. Over the potential range 2-4.2 V, the capacity reaches the maximum value of 22 $mAhg^{-1}$ in the first charge and discharge cycle (Figure 4.9) with a value of the discharge capacity between 20 and 30 $mAhg^{-1}$ (Figure 4.10). When the potential range is in the range 2-4.0 V, the capacity shows values of 16-20 $mAhg^{-1}$ (Figure 4.11) with a discharge capacity between 15 and 20 $mAhg^{-1}$ (Figures 4.12 and 4.13). These results indicate a good stability of the **Fe-2** crystal structure and the reversible nature of sodium ion insertion, but also the poor electrochemical activity of this material.

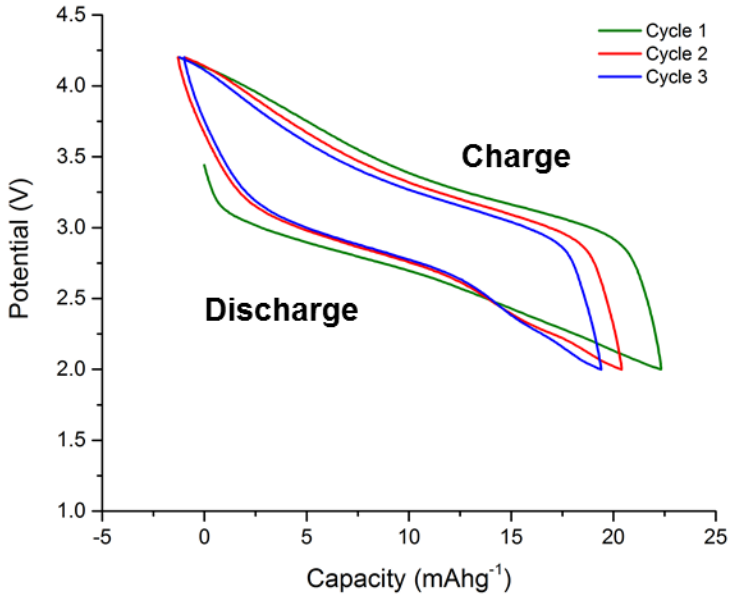

Figure 4.9. Load curves at a rate of C/10 (10 $mAhg^{-1}$) over a potential range 2-4.2 V.

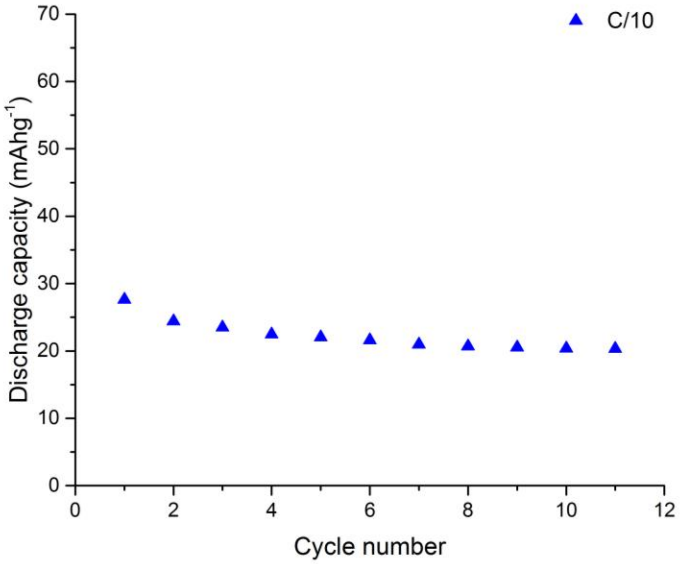

Figure 4.10. Discharge capacity *vs* cycle number for **Fe-2** at a rate of C/10 over the potential window 2-4.2 V.

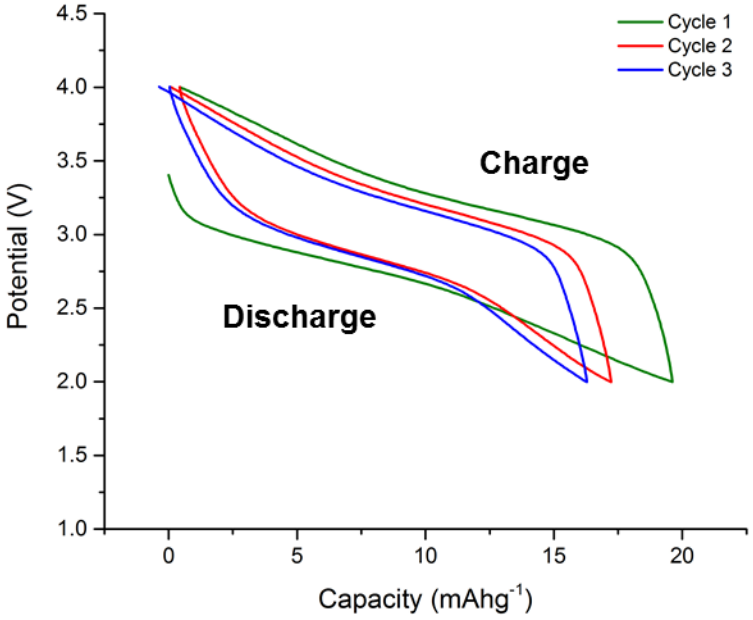

Figure 4.11. Load curves at a rate of C/10 (10 $mAhg^{-1}$) over a potential range 2-4 V.

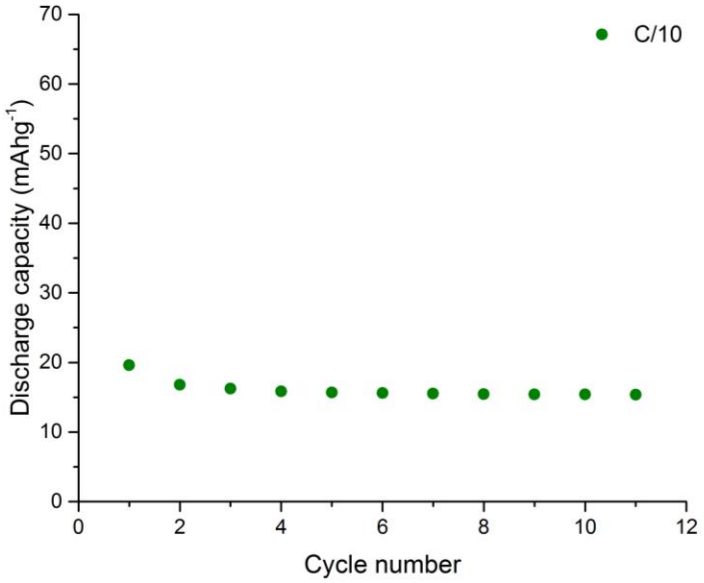

Figure 4.12. Discharge capacity *vs* cycle number for **Fe-2** at a rate of C/10 over the potential window 2-4 V.

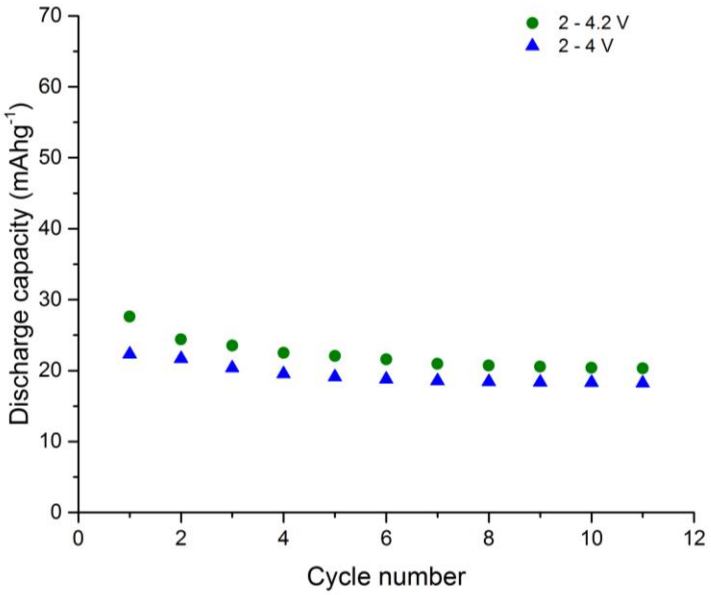

Figure 4.13 Discharge capacity *vs* cycle number for **Fe-2** at a rate of C/10 over the potential windows 2-4 V (in blue) and 2-4.2 V (in green).

4.5 Magnetic characterisation

In order to understand the magnetic properties of **Fe-2**, several measurements were performed in collaboration with Professor Alexander N. Vasiliev and co-workers at the Faculty of Physics of the Moscow State University. In particular, measurements of the susceptibility (χ) were carried out.

The zero field cooled (ZFC) magnetic susceptibility was measured in an applied field of 1 T (Figures 4.14).

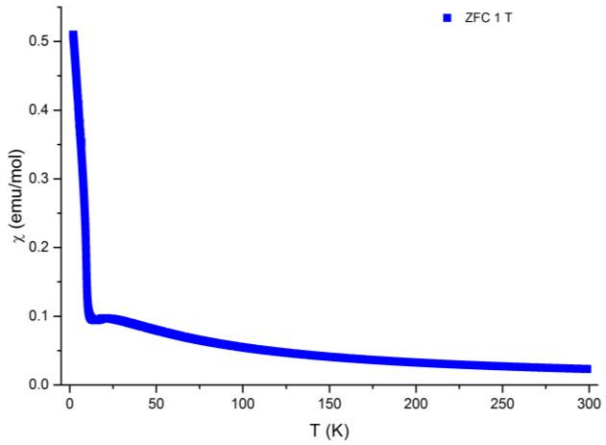

Figure 4.14. Susceptibility plot of **Fe-2**

It is possible to model the inverse magnetic susceptibility with a modified Curie-Weiss law (see Eq. 3.1) over the range 40-300 K to yield a temperature-independent term (χ_0) equal to -0.846 emu/mol as well as a Curie constant and a Weiss temperature value of C = 8.1 emu K/mol and Θ = -49 K, respectively (Figure 4.15).[4,8,16]

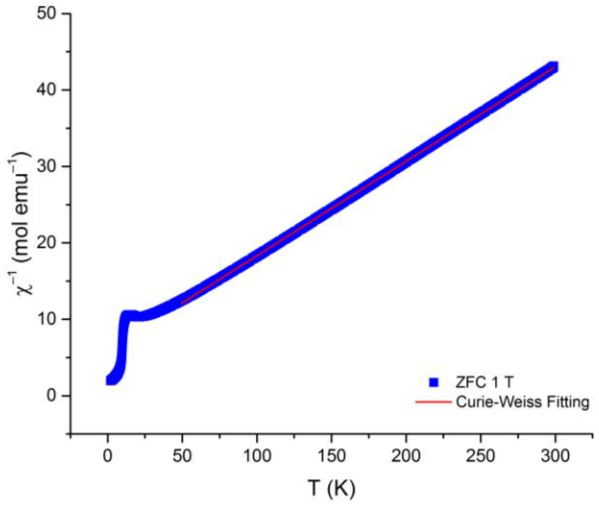

Figure 4.15. Inverse susceptibility plot of **Fe-2** with red line indicating the Curie-Weiss fit between 50 and 300 K.

The negative value of the Weiss constant indicates that the magnetic correlations in the **Fe-2** system are predominantly antiferromagnetic. The transition temperature T_N of the paramagnetic-antiferromagnetic transition has an estimated value of 18.8 K (Figures 4.14, 4.15).[4,8,16]

The effective magnetic moment (μ_{eff}) obtained from the proportional relationship between the Curie constant and the number of magnetic ions, *n* (see Chapter 3, section 3.5) is equal to 6.1 μ_B and compares well with the theoretical estimation (see Eq. 3.3). This results in $\mu_{theor} \approx 8.3\ \mu_B$ for two high-spin $S = 5/2$ Fe^{3+} ions per formula unit with average value $g = 1.993$.

4.6 Chapter conclusions

In this chapter a novel potential cathode material for sodium batteries has been described. **Fe-2** has been synthesised by a low temperature and cheap synthesis route and exhibits a 3D framework crystal structure with Fe_2O_9 dimer chains running along the *c*-direction. Each Fe_2O_9 dimer is composed by two face-sharing FeO_6 octahedra which are bridged to the other ones by three $(HPO_3)^{2-}$ anions forming chains parallel to the *c*-axis. A hexagonal open channel present along the *c*-axis is a key feature of this structure. This channel is surrounded by six groups of face sharing FeO_6 octhahedra and hydrogen atoms of the HPO_3^{2-} anions are around the 6_3 axis. The P-H bonds are pointed toward the axis of the empty channel, meaning that a weak but significant electron density is present into the hexagonal channel, promoting the possibility of ion intercalation.

However, even if the material exhibits good capacity retention, the observed capacity values are far from the theoretical capacity over the wider voltage window, together with a low Coulombic efficiency close to 25%, indicating poor electrochemical activity of this material.

The observed magnitude of the antiferromagnetic exchange coupling is in agreement with the general behaviour of various mono and di-bridged Fe^{3+} complexes. The observed long-range ordering at about 20 K indicates that the phosphorus atoms of the phosphite ligands connect the Fe_2O_9 units magnetically throughout the crystal.

In conclusion, $Fe_2(HPO_3)_3$ is an interesting 3D framework structure and electrochemically active with antiferromagnetic behaviour. Unfortunately, despite the fact that this compound shows a 3D framework structure with holes and channels, the electrochemical capacity showed during the galvanostatic cycling tests carried out is small in size and far from the theoretical capacity under these experimental conditions. This suggests that it may be necessary to change the experimental conditions and/or better optimise the electrochemical testing in order to obtain more interesting results.

4.7 References

1. R.E. Morris, M.P Attfield, A.K. Cheetham, *Acta Crystallogr. C*, 1994, **50**, 473.
2. R. Gond, G. Shinde, P. Barpanda., Abstract MA2016-02 720, ECS Meeting abstracts, 2016.
3. X. Lin, Y. Zhao, Y. Dong, Q. Kuang, Z. Liang, D. Yan, X. Liua, *Materials Science and Engineering B*, 2015, **197**, 58.
4. J. Ensling, P. Gutlich, R. Schmidt, R. Kniep, *Inorg. Chem.*, 1994, **33**, 3595.
5. M. Sghyar, J. Durand, L. Cot, M. Rafiq, *Acta Crystallogr. C*, 1991, **47**, 2515.
6. B. Ewald, Y. Prots, R. Kniep, *Z. Kristallogr.-New Cryst. Struct.*, 2003, **218**, 377.
7. C. Jacoboni, C. Canali, G. Ottaviani, A. Alberigi Quaranta, *Solid State Electron*, 1977, **20**, 77.
8. V.M. Kovrugin, E.E. Gordon, E.E. Kasapbasi, M.H. Whangbo, M. Colomont, O.I. Siidra, S. Colis, S.V. Krivovichev, O. Mentré, *J. Phys. Chem. C*, 2016, **120**, 1650.
9. N.E.Brese, M. O'Keeffe, *Acta Crystallogr.B.*, 1991, **47**, 192.
10. J. Loub, *Acta Crystallogr.B.*, 1991, **47**, 468
11. K.Nakamoto, *Infrared and Raman Spectra of Inorganic and Coordination Compounds Part A*, John Wiley &Sons, 2009.
12. U. Chung, J.L. Mesa, J.L. Pizarro, I. De Meatza, M. Bengoechea, J.R. Fernandez, M.I. Arriortua, T.Rojo, *Chem. Mater.*, 2011, **23**, 4317.
13. H. YaghoobnejadAsl, A. Choudhury, *Inorg. Chem.*, 2015, **54**, 6566.
14. H. YaghoobnejadAsl, K. Ghosh, M.P.V. Meza, A. Choudhury, *J. Mater. Chem. A*, 2015, **3**, 7488.

15. T. Rojo, J.L. Mesa, J. Lago, B. Bazan, J.L. Pizarro, M.I. Arriortua, *J. Mater. Chem.*, 2009, **19**, 3793.

16. L.K. Elbouaanani, B. Malaman, R. Gerardin, *J. Solid State Chem.*, 1999, **148**, 455.

Chapter 5

$NaFe(H_2PO_3)_4$ and $NaFe(HPO_4)(H_2PO_4)_2 \cdot H_2O$: Two Potential Cathode Materials for Sodium Batteries

5.1 Introduction

Three-dimensional frameworks based on polyanions such as $(PO_4)^{3-}$ and $(HPO_3)^{2-}$ may be stable during the charge/discharge process. The phosphite ion, HPO_3^{2-} is structurally similar to phosphate, PO_4^{3-}, both having tetrahedral geometry and so transition-metal phosphites exhibit a similar structural chemistry to phosphates. However, the phosphite group has less charge and a smaller number of oxygens, making clear important differences between phosphite[1-3]and phosphate compounds[4-7]. Studies on metal phosphites have shown that interesting and novel structures can be produced using hydrothermal methods, including structures containing channels and cavities, which are of interest for intercalation and extraction of some alkali ions for electrochemical purposes. [1-3]

In this context, the iron phosphite compounds $NaFe(H_2PO_3)_4$ and $NaFe(HPO_4)(H_2PO_4)_2 \cdot H_2O$ described in this chapter are interesting examples of the variety of atomic arrangements and crystal structures allowed by polyanions.

In order to understand more about the electrochemical properties of the phosphate and the phosphite compounds showing these kinds of framework structures, $NaFe(H_2PO_3)_4$ hereinafter abbreviated "**Fe-3**", and $NaFe(HPO_4)(H_2PO_4)_2 \cdot H_2O$ hereinafter abbreviated "**Fe-4**", have been studied in depth and fully characterised as potential cathode materials for the next generation of sodium batteries. To the best of our knowledge, the structure of **Fe-3** has never been reported in the literature.

5.2 $NaFe(H_2PO_3)_4$

5.2.1 Material synthesis

Fe-3 was synthesised through hydrothermal synthesis by reacting NaF (3 mmol) with Fe_2O_3 (1 mmol) and H_3PO_3 (1.22 mmol), without the addition of any solvent. This mixture was sealed in a Teflon-lined stainless steel autoclave and heated to 140 °C for 3 days. The reaction was cooled to room temperature and colourless prismatic chip crystals were recovered by filtration from a minor aqueous phase.

5.2.2 Structural characterisation

Fe-3 crystals are well-faceted prismatic blocks with a particle size of about 200 μm, as shown in the SEM images (Figure 5.1).

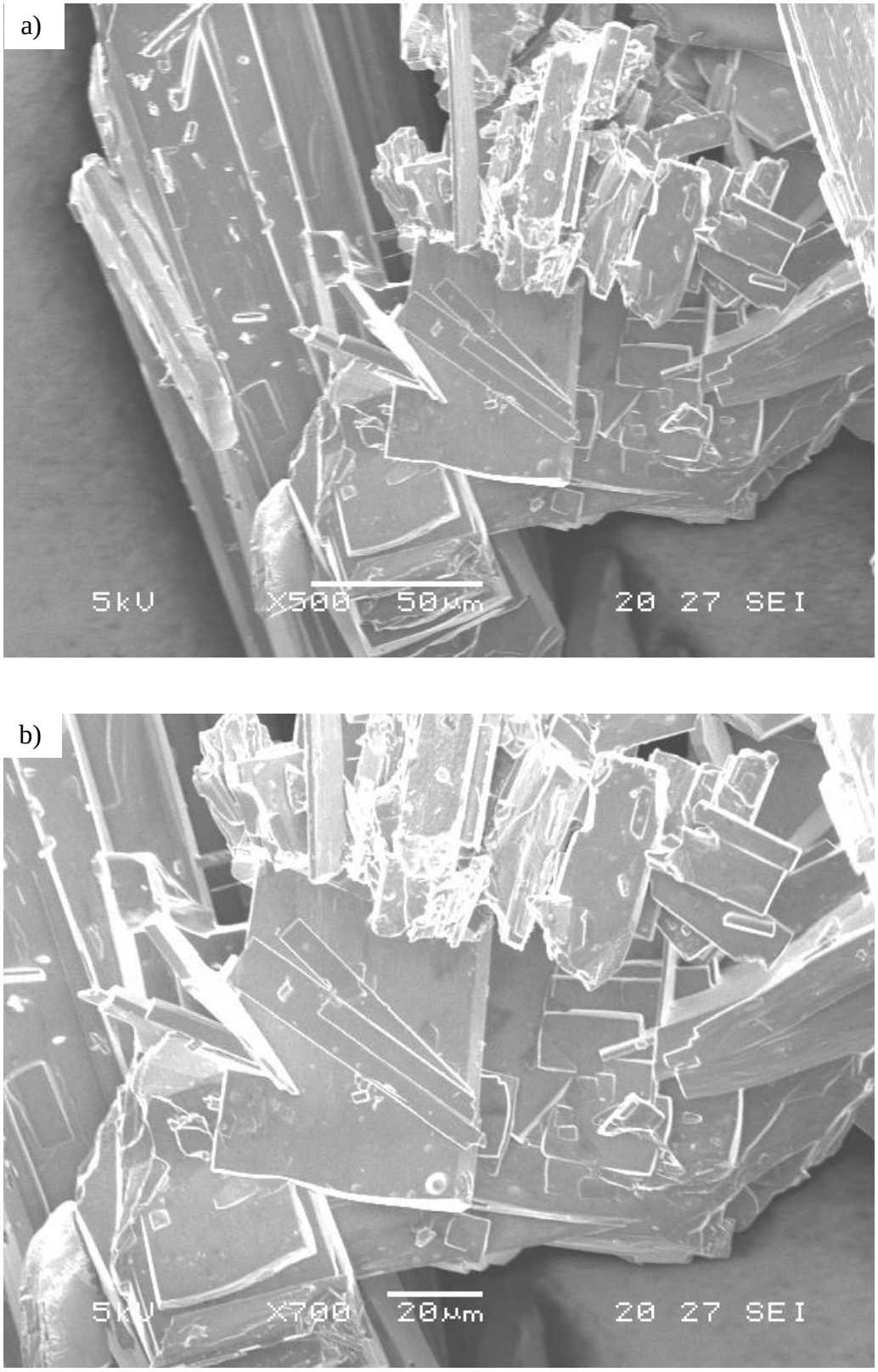

Figure 5.1. a) SEM picture and b) zoom-in of **Fe-3** crystals.

The analysis of the single crystal X-ray diffraction data shows **Fe-3** adopting a monoclinic crystal structure in the P 2/m space group (Table 5.1).

Table 5.1. Crystallographic data for **Fe-3**.

Molecular formula	**$NaFe(H_2PO_3)_4$**
Formula Mass (amu)	245.7
Crystal system	Monoclinic
Space group	P 2/m
a	5.2421(13) Å
b	7.0426(16) Å
c	15.864(4) Å
α	90°
β	93.428(5)°
γ	90°
V (A^3)	584.6 (3)
Z	2
ρ (calcd) (g/cm^3)	1.14
Temp (K)	173 (2)
F (000)	201.0
μ (mm^{-1})	0.965 (calculated)
R_{int}	0.177
R_1,wR_2 (I >2σ)	0.178/0.452
R_1,wR_2 (all data)	0.185/0.456
Reflections number gt	1301
Reflections number total	1099
GOF on F^2	3.337

Initially, **Fe-3** was resolved as $NaFe(PO_3)_4$, but by looking carefully at the P-O bond distances it has been possible to identify P1-O4, P2-O5 and P1-O4 bonds longer than

the relative values reported in literature (1.47 Å and 1.49 Å for P-O and P-O-(H) bonds respectively).[8] According to that, and in order to establish charge balance, two hydrogen atoms have been identified to be bonded to the PO_3 tetrahedra, obtaining in this way $NaFe(H_2PO_3)_4$ as the final structure. Unfortunately, due to the disorder present in the structure, the final model represents only an approximate refinement of the crystal structure.

Fe-3 exhibits a novel 2D framework structure with FeO_6 octahedra bonded with each other by PO3 tetrahedra, with which they share an oxygen atom. Each sodium atom is surrounded by two FeO6 octahedra. (Figures 5.2-5.4). The data quality, the disorder and the R factor do not allow the facility to locate the hydrogens and to represent the complete PO_3 tetrahedra. The overall structure is as reported in the crystal information file (see Supporting Information).

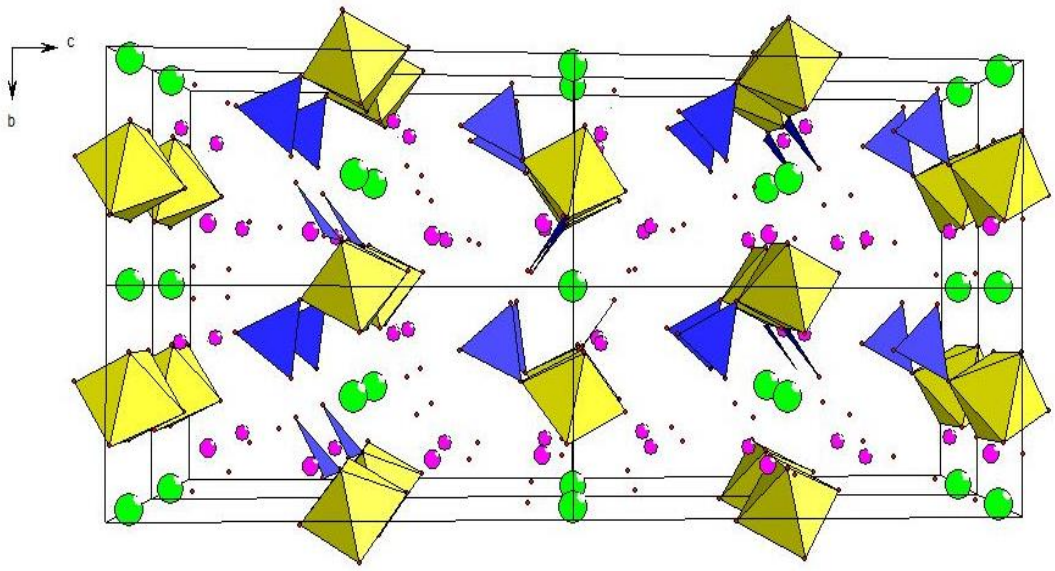

Figure 5.2. Polyhedral representation of **Fe-3** crystal structure along the *a*-axis. FeO_6 octahedra in yellow, phosphorus in pink, PO_3 triangular in blue, oxygens in red, sodium ions in green spheres.

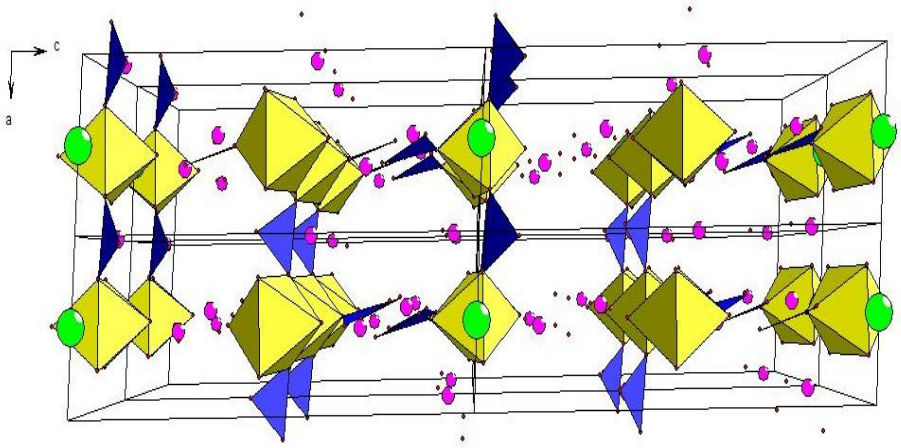

Figure 5.3. Polyhedral representation of **Fe-3** crystal structure along the *b*-axis. FeO_6 octahedra in yellow, phosphorus in pink, PO_3 triangular in blue, oxygens in red, sodium ions in green spheres.

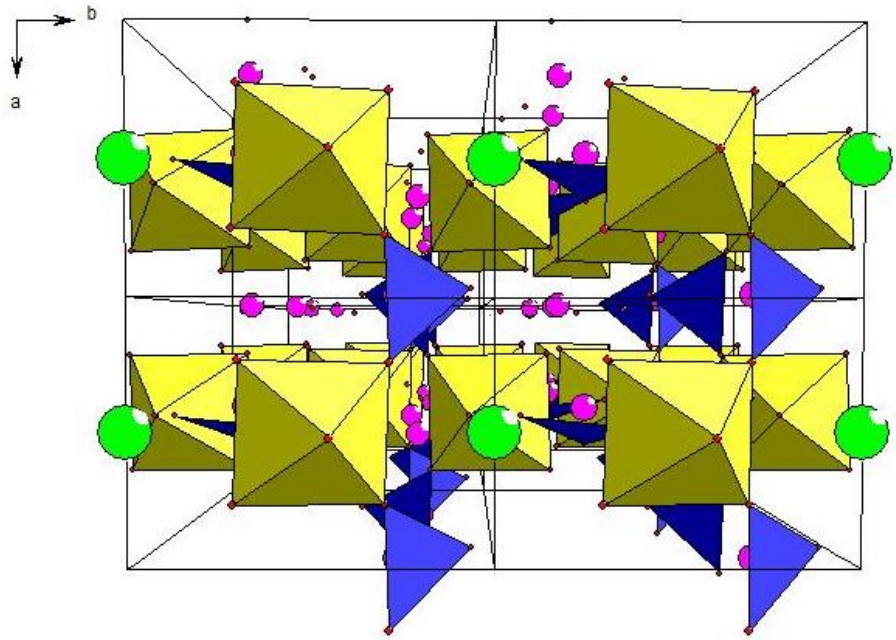

Figure 5.4. Polyhedral representation of **Fe-3** crystal structure along the *c*-axis. FeO_6 octahedra in yellow, phosphorus in pink, PO_3 triangular in blue, oxygens in red, sodium ions in green spheres.

The single crystal data were analysed refining all non-H atoms. In order to investigate further the presence of fluoride, Energy-dispersive X-ray spectroscopy (EDX) was carried out. . The qualitative EDX analysis confirmed the presence of oxygen, sodium, phosphorous and iron in the **Fe-3** compound (Figure 5.5).

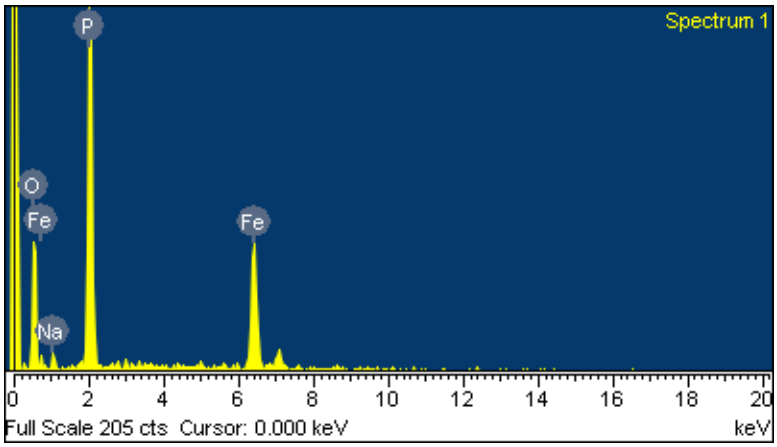

Figure 5.5. EDX spectrum for **Fe-3**.

Both of the iron sites are occupied by Fe^{3+} with octahedral geometry and bond lengths in the normal range for Fe^{3+} (1.711-2.012 Å).[8] In order to confirm the iron oxidation state and the location of OH groups, Bond Valence Sum (BVS) calculations were carried out. The Bond Valance parameters relate the bond valances and the bond lengths (see Chapter 2, Section 2.3). The data obtained from the BVS calculations for **Fe-3** using the Bond Valance parameters reported in literature for the Fe-O bond (1.759 Å) and the HP-O bond (1.626 Å) are in good agreement with the hypothesised valence state of the iron (3+) and suggest the present of the HP group (4+) in the structure (Table 5.2).[9,10] Indeed, the data quality and the disorder present in the structure do not permit to locate the OH and the HP groups in the **Fe-3** structure and to completely represent the PO_3 tetrahedra (Table 5.2).[9,10]

Table 5.2. Selected bond lengths and bond valence sums for **Fe-3**.

		Bond length (Å)	Bond valence
Fe1	O1 x2	1.711(9)	0.564
	O2 x2	2.012(10)	0.505
	O3 x2	1.992(11)	0.533
			∑ **3.204**
P1	O2	1.479(11)	1.452
	O3	1.492(12)	1.402
	O4	1.553(11)	1.189
			∑ **4.042**
P2	O1	1.485(4)	1.429
	O5	1.533(14)	1.255
	O6	1.489(12)	1.413
			∑ **4.097**

The purity of the sample was verified by Powder X-ray diffraction (PXRD) experiments. The good match of the patterns suggests a good level of purity of the sample. Extra peaks at 17° and 33° correspond to the Teflon support used to carry out the powder diffraction measurements (Figure 5.6). A PXRD pattern of a blank Teflon sample mounting is shown for comparison in Figure 5.7.

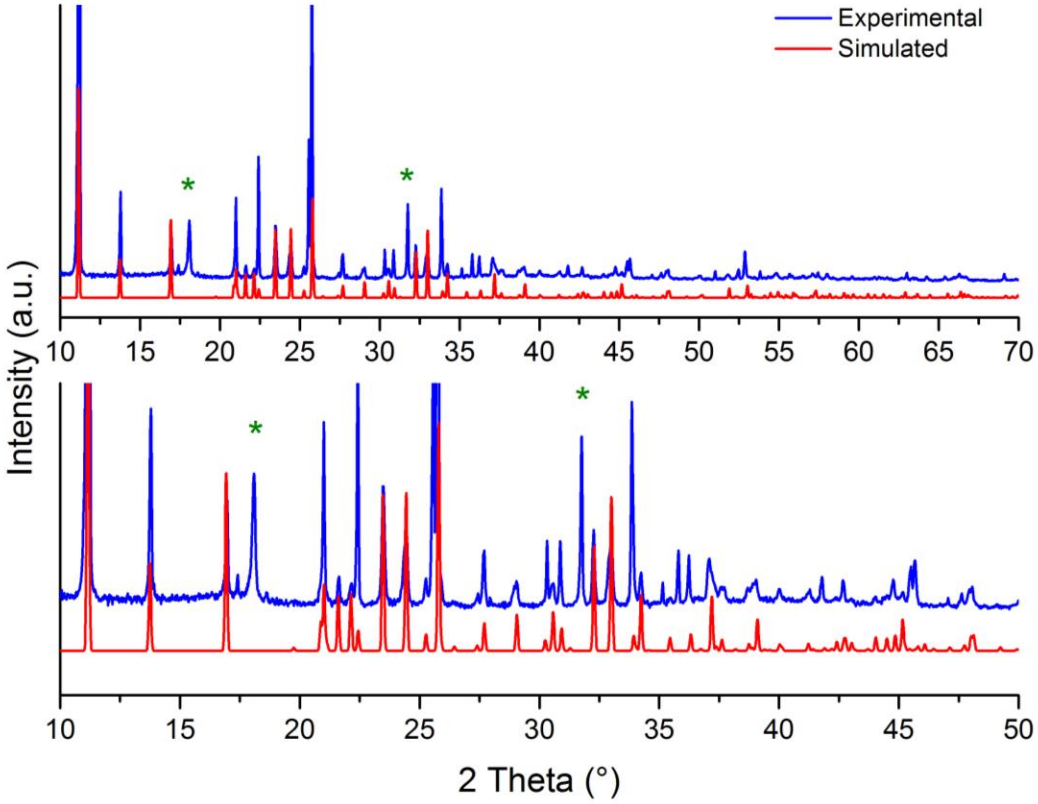

Figure 5.6 Observed and simulated PXRD pattern for **Fe-3**: experimental patterns in blue and calculated patterns from single crystal data in red; full pattern on the top, zoom-in of low angle region on the bottom. Peaks arising from the Teflon sample mounting are marked with an asterisk.

Infrared spectroscopy (IR) was used to determine the presence of P-H bonds in the structure. The IR spectrum of **Fe-3** mainly consists of strong absorption peaks corresponding to the P-H and the P-O bonds of the phosphite moiety in the structure. The data show a typical P-H stretching signal at 2450 cm^{-1} and a strong PO_3 stretching peak in the range of 950-1150 cm^{-1} confirming the presence of P-H and P-O bonds in the crystal structure (Figure 5.7).[11]

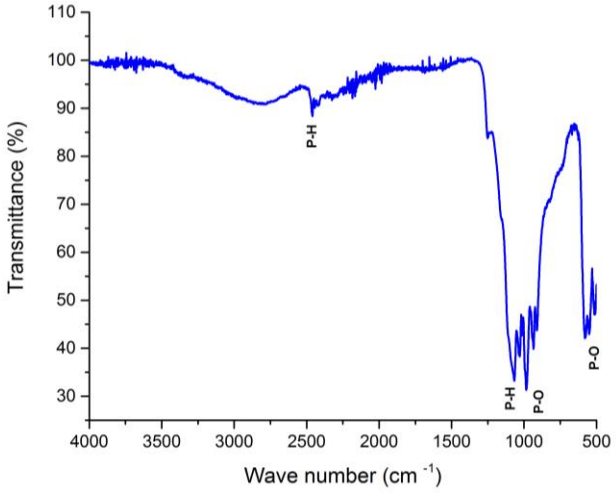

Figure 5.7. IR spectrum of **Fe-3**.

The increase in temperature during the life of batteries due to the charge and discharge process can influence the performance of the battery materials, so it is important to understand how robust a potential battery material is under temperature stress. In order to characterise **Fe-3** from this point of view, Thermogravimetric analysis (TGA) was carried out. **Fe-3** shows good stability and a total weight loss of 8.4% below 500° C, confirming the potential use of **Fe-3** as a cathode material (Figure 5.8).

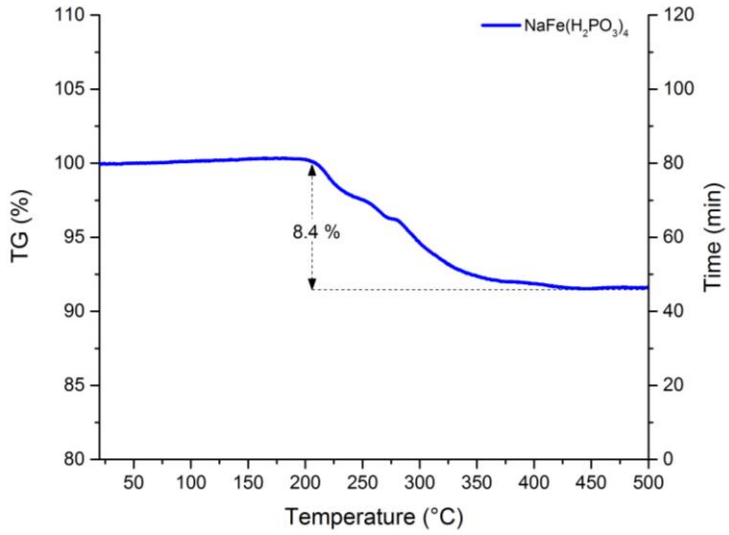

Figure 5.8. TGA curve for **Fe-3**.

5.2.3 Electrochemical characterisation

The interesting properties of phosphite compounds in terms of stability, safety and the promising 2D and 3D framework structures they can form suggest the employment of phosphites as materials for ion batteries.[1-3] In order to evaluate the electrochemical activity of **Fe-3**, composite electrodes were prepared by mixing **Fe-3** with super S carbon and Ketjen black carbon in the weight ratio 60:15:15. These chemicals were mixed for 3.5 h using a Fritsch Pulverisette 7 mill. A solution of Kynar Flex 2801 in N-methyl-2-pyrrolidone (NMP) was then added as binder. The slurry obtained in this way was then cast on aluminium foil using a doctor blade. The final ratio of active material, conducting carbon and binder used in the composite electrodes was 60:30:10.

The coin cell batteries built in this way were then subject to galvanostatic cycling tests carried out in the potential ranges 1.2-4 V at C/10 rate. The load curves correspond to sodium insertion and extraction and were obtained at C/10 (10 $mAhg^{-1}$). The data show the presence of sloping potential with average discharge voltage of 2.7 V *vs* Na^{+}/Na. These results indicate a good stability of the **Fe-3** crystal structure and the reversible nature of sodium ion insertion. However the Coulombic efficiency and the electrochemical activity of **Fe-3** as shown in Figures 5.9 and 5.10 are not comparable with the ones presented by **Fe-1** (see Chapter 3, Section 4).

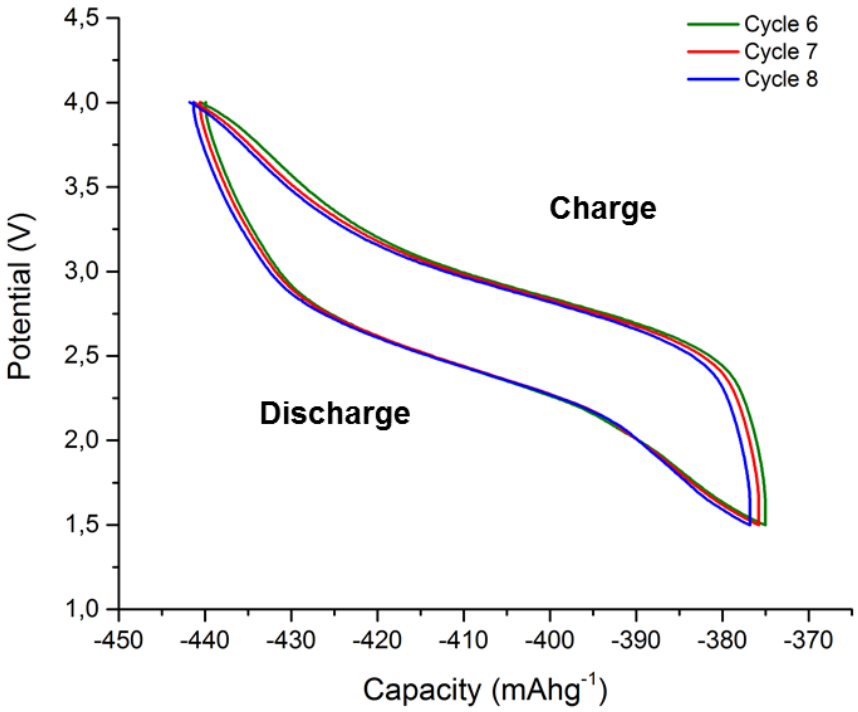

Figure 5.9. Load curves at a rate of C/10 (10 $mAhg^{-1}$) and a potential range 1.2-4 V.

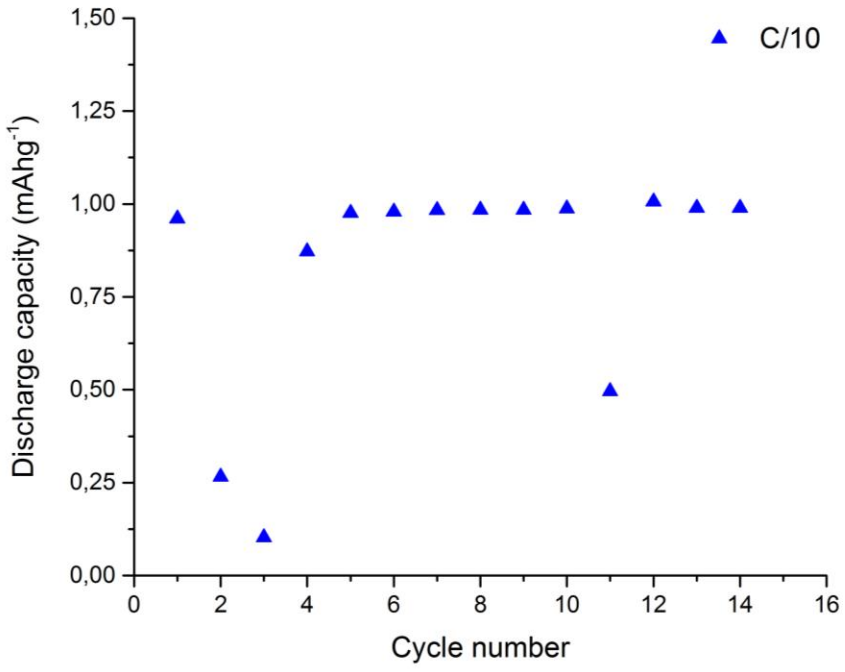

Figure 5.10. Discharge capacity *vs* cycle number for **Fe-3** at a rate of C/10 over the potential window 2-4.2 V.

5.3 $NaFe(HPO_4)(H_2PO_4)_2 \cdot H_2O$

5.3.1 Material synthesis

The compound $NaFe(HPO_4)(H_2PO_4)_2 \cdot H_2O$, abbreviated as **Fe-4**, was synthesised through hydrothermal synthesis with reaction of NaF (1 mmol), Fe_2O_3 (1 mmol) and H_3PO_4 (2 ml), without the addition of any solvent. This mixture was sealed in a Teflon-lined stainless steel autoclave and heated to 100 °C for 3 days. The reaction was cooled to room temperature and colourless prismatic crystals were recovered by filtration from a minor aqueous phase.

5.3.2 Structural characterisation

Fe-4 crystals are well-faceted cubic blocks with particle size about 1500 μm, as shown in the SEM images (Figure 5.11).

a)

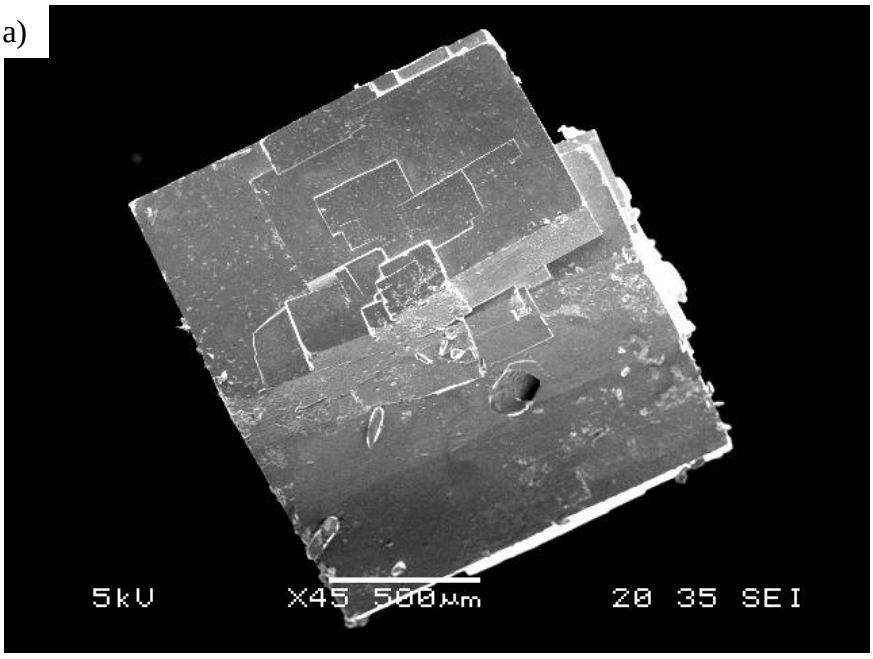

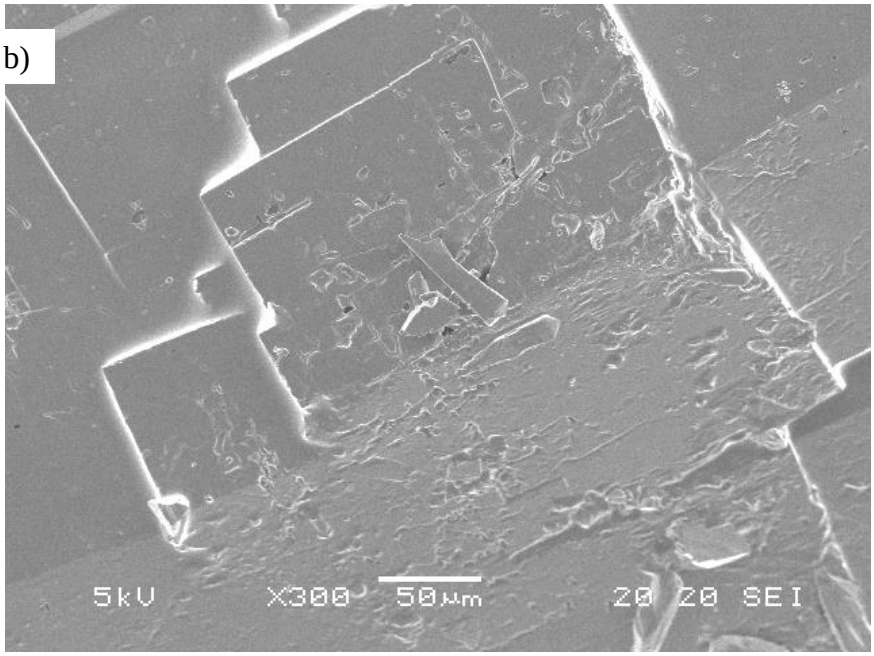

Figure 5.11. a) SEM picture and b) zoom-in of **Fe-4** crystals.

The analysis of the single crystal X-ray diffraction data show **Fe-4** adopting a monoclinic crystal structure at low temperature (173 K) and an orthorhombic geometry at room temperature (293 K), in agreement with what reported in literature (Table 5.3).[12]

Table 5.3 Crystallographic data for **Fe-4**.

Molecular formula	**$NaFe(HPO_4)(H_2PO_4)_2 \cdot H_2O$**	
Formula Mass (amu)	386.81	386.81
Crystal system	Monoclinic	Orthorhombic
Space group	P 2_1/n	P c n b
a	8.7449(8) Å	8.7509(9) Å
b	18.959 (2) Å	18.980 (2) Å
c	12.5253(13) Å	12.5332(13) Å
α	90°	90°
β	90.696(2)°	90°
γ	90°	90°
V (A^3)	2076.47(6)	2050
Z	8	8
ρ (calcd) (g/cm^3)	2.474	2.474
Temp (K)	173 (2)	273
F (000)	1544	1544
μ (mm^{-1})	2.03 (calculated)	2.038 (calculated)
R_{int}	0.0297	0.0831
R_1,wR_2 (I >2σ)	0.029/0.094	0.032/0.104
R_1,wR_2 (all data)	0.030/0.095	0.034/0.105
Reflections number gt	3527	1912
Reflections number total	3818	1761
GOF on F^2	1.000	0.924

Fe-4 exhibits a 3D framework crystal structure with open channels and FeO_6 octahedra, each of them connected to two other FeO_6 octahedra by PO_3 tetrahedra. The net result is a complex and quite open framework amenable to several distinct possible ionic migration pathways for sodium ions (Figures 5.12-5.14).

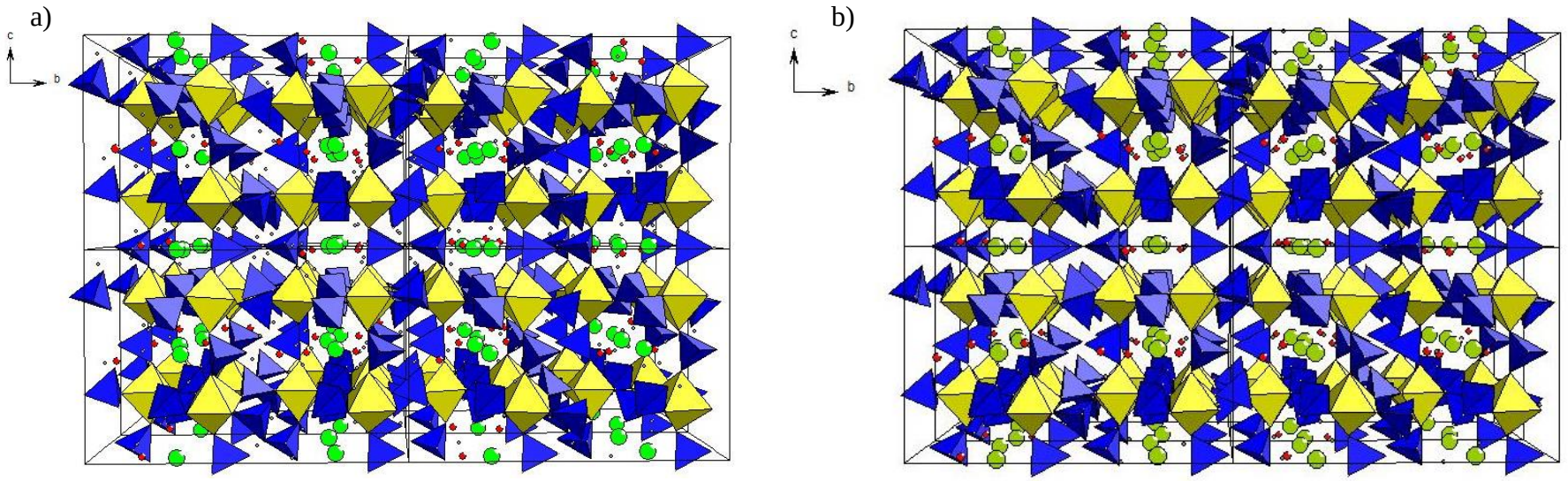

Figure 5.12. Polyhedral representation of **Fe-4** crystal structure along the *a*-axis. a) Monoclinic low temperature (173 K) crystal structure, b) orthorhombic room temperature crystal structure. FeO_6 octahedra in yellow, phosphite tetrahedra in blue, sodium ions in green.

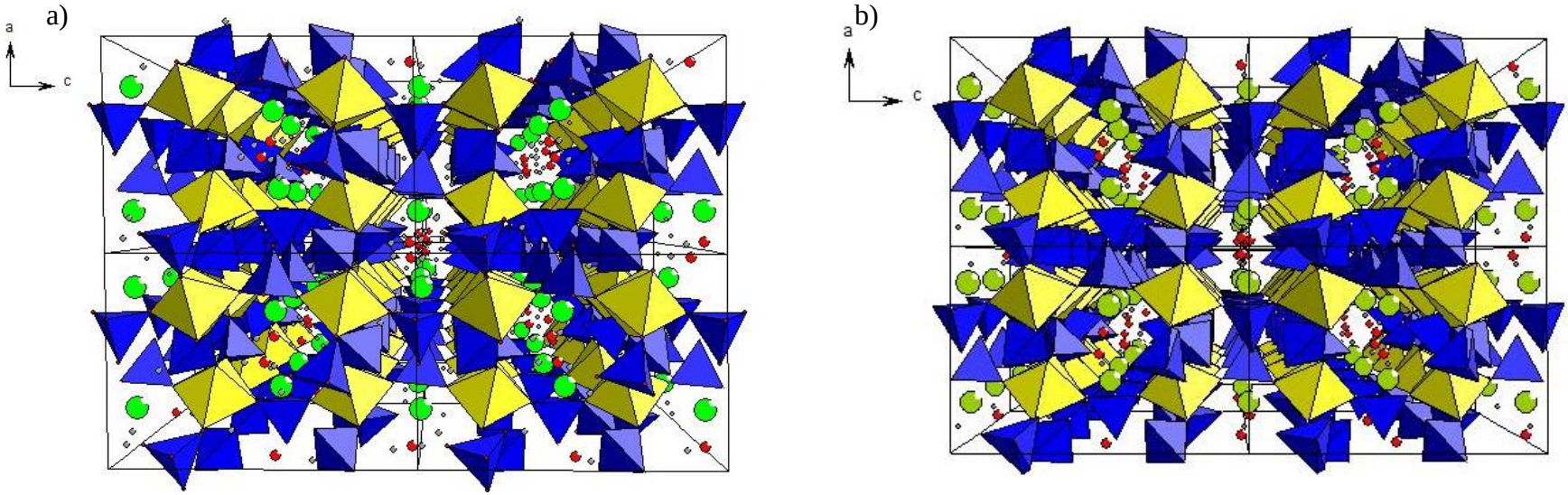

Figure 5.13. Polyhedral representation of **Fe-4** crystal structure along the *b*-axis. a) Monoclinic low temperature (173 K) crystal structure, b) orthorhombic room temperature crystal structure. FeO_6 octahedra in yellow, phosphite tetrahedra in blue, sodium ions in green.

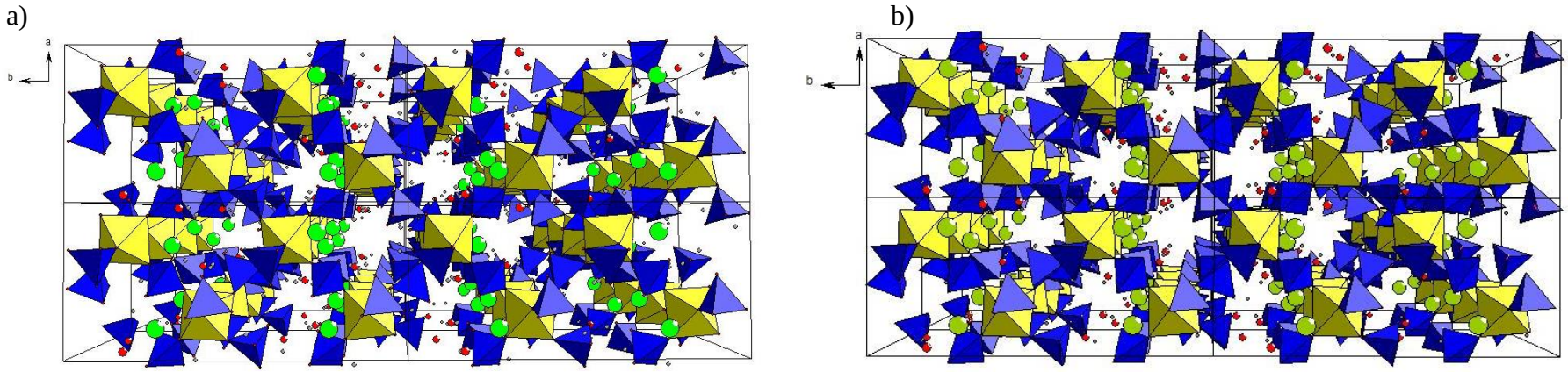

Figure 5.14. Polyhedral representation of **Fe-4** crystal structure along the *c*-axis. a) Monoclinic low temperature (173 K) crystal structure, b) orthorhombic room temperature crystal structure. FeO_6 octahedra in yellow, phosphite tetrahedra in blue, sodium ions in green.

The single crystal data were analysed anisotropically for refining all non-H atoms and at the beginning all H-atoms were located by Fourier methods and refined without constraints. Energy-dispersive X-ray spectroscopy (EDX) was carried out in order to investigate the chemical composition of **Fe-4** further and exclude the presence of any fluorine in the final structure solution. The qualitative EDX analysis confirmed the presence of oxygen, sodium, phosphorous and iron in the **Fe-4** compound (Figure 5.15).

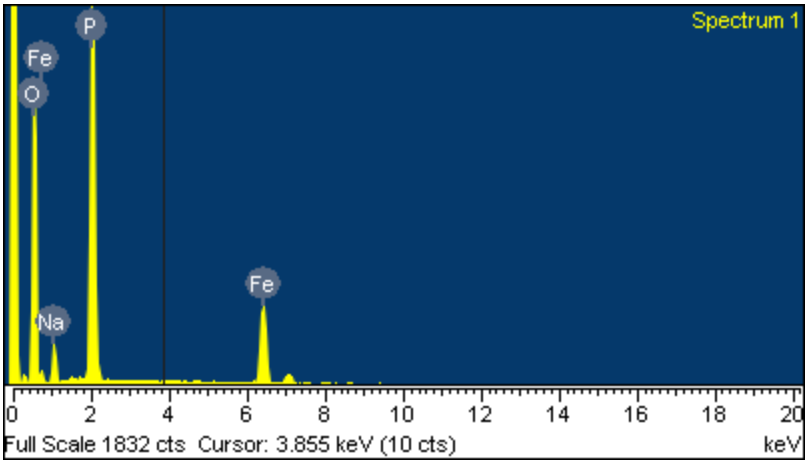

Figure 5.15. EDX spectrum for **Fe-4**.

Both of the iron sites are occupied by Fe^{3+} with octahedral coordination and bond lengths in the normal range for Fe^{3+} (1.965-2.016 Å).[14-] In order to confirm the iron oxidation state and the location of the OH groups, Bond Valence Sum (BVS) calculations were carried out. The Bond Valance parameters relate the bond valances and the bond lengths (see Chapter 2, Section 2.3). The BVS calculations for **Fe-4** using the Bond Valance parameters reported in literature for the Fe-O bond (1.759 Å) and P-O bond (1.604 Å) are in good agreement with the hypothesised valence state of the iron (3+) and of the phosphorous (5+) atoms, allowing to consider of minimal size the disorder and the partial occupancy effects in the **Fe-4** structure (Table 5.4).[9,10]

Table 5.4 Selected bond lengths and bond valence sums for **Fe-4** monoclinic low temperature (173 K) crystal structure.

		Bond length (Å)	Bond valence
Fe1	O1	2.010(17)	0.507
	O2	1.966(17)	0.571
	O3	2.016(17)	0.499
	O4	1.965(17)	0.573
	O11	2.001(17)	0.520
	O18	1.983(18)	0.546
			∑ 3.216
Fe2	O5	2.017(17)	0.497
	O6	2.020(17)	0.493
	O7	1.954(18)	0.590
	O8	1.966(18)	0.571
	O17	1.989(17)	0.536
	O21	2.004(17)	0.516
			∑ 3.203
P1	O17	1.501(18)	1.367
	O18	1.494(18)	1.394
	O23	1.558(19)	1.170
	O24	1.573(2)	1.126
			∑ 5.057
P2	O11	1.501(18)	1.367
	O21	1.502(18)	1.365
	O25	1.577(2)	1.114
	O26	1.546(2)	1.212
			∑ 5.057
P3	O2	1.516(18)	1.314
	O8	1.515(18)	1.317
	O10	1.587(18)	1.085
	O12	1.518(18)	1.307
			∑ 5.024
P4	O4	1.519(17)	1.303
	O7	1.518(18)	1.307
	O9	1.511(18)	1.331
	O20	1.587(18)	1.082
			∑ 5.022
P5	O3	1.506(17)	1.370
	O6	1.504(17)	1.356
	O13	1.578(18)	1.109
	O14	1.575(19)	1.118
			∑ 4.953
P6	O1	1.504(18)	1.356
	O5	1.506(17)	1.351
	O19	1.575(19)	1.121
	O22	1.580(18)	1.103
			∑ 4.931

Table 5.5. Selected bond lengths and bond valence sums for **Fe-4** orthorhombic room temperature crystal structure.

		Bond length (Å)	Bond valence
Fe1	O1	1.998(15)	0.507
	O2	1.997(16)	0.571
	O5	2.015(15)	0.499
	O10	2.019(15)	0.573
	O11	1.968(16)	0.520
	O12	1.965(14)	0.546
			∑ **3.216**
P1	O1	1.497(16)	1.352
	O2	1.494(16)	1.371
	O3	1.548(16)	1.190
	O4	1.579(16)	1.156
			∑ **5.069**
P2	O5x2	1.503(16)	1.202
	O6x2	1.579(16)	1.311
			∑ **5.026**
P3	O7x2	1.572(15)	1.258
	O10x2	1.502(16)	1.243
			∑ **5.002**
P4	O8	1.582(18)	1.311
	O9	1.515(19)	1.309
	O11	1.515(16)	1.328
	O12	1.512(15)	1.091
			∑ **5.039**

The purity of the sample was verified by Powder X-ray diffraction (PXRD) experiments. The good match of the patterns suggests a good level of purity of the sample. Extra peaks at 17° and 33° correspond to the Teflon support used to carry out the powder diffraction measurements (Figure 5.16).

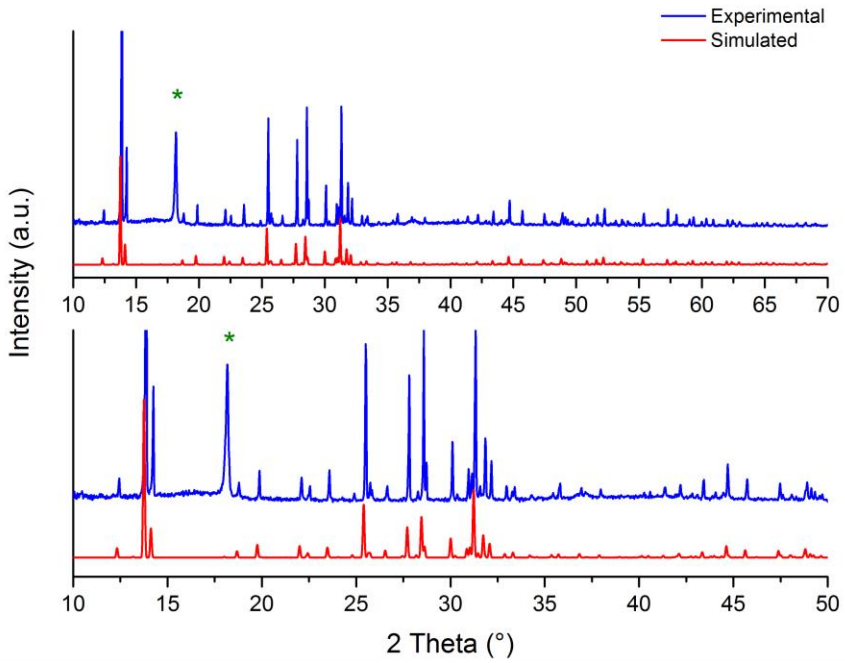

Figure 5.16. Observed and simulated PXRD pattern for **Fe-4**: Experimental patterns in blue and calculated patterns from single crystal data in red; full pattern on the top, zoom-in of low angle region on the bottom. Peaks arising from the Teflon sample mounting are marked with an asterisk.

Infrared spectroscopy (IR) was used to investigate the presence of P-H bonds in the structure. The IR spectrum of **Fe-4** mainly consists of strong absorption peaks due to P-H and P-O bonds of the phosphate moiety. The data show a typical P-H stretch around 2450 cm^{-1} and strong PO_4 stretching modes in the range of 950-1150 cm^{-1}, confirming the presence of P-H and P-O bonds in the crystal structure (Figure 5.17).[11]

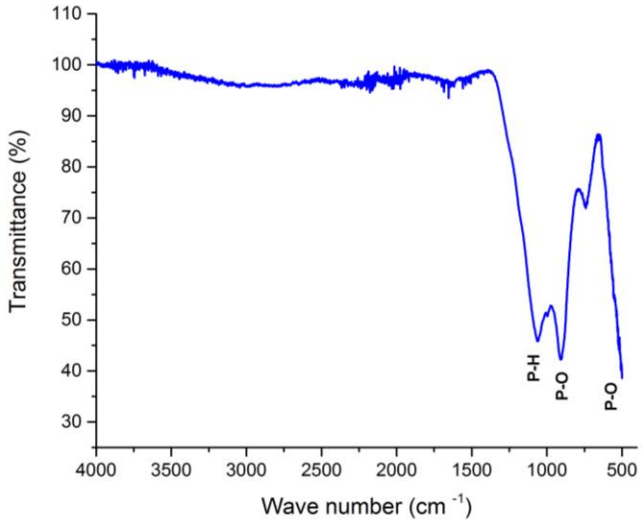

Figure 5.17. IR spectrum for **Fe-4**.

The increase in temperature during the charge and discharge process can drastically affect the performance of battery materials. In order to characterise **Fe-4** and understand how robust it is under temperature stress, Thermogravimetric analysis (TGA) was carried out. **Fe-4** exhibits good stability, no weight loss was observed until 143 °C, with a total weight loss of 15 % below 500 °C confirming its potential use as cathode material (Figure 5.18).

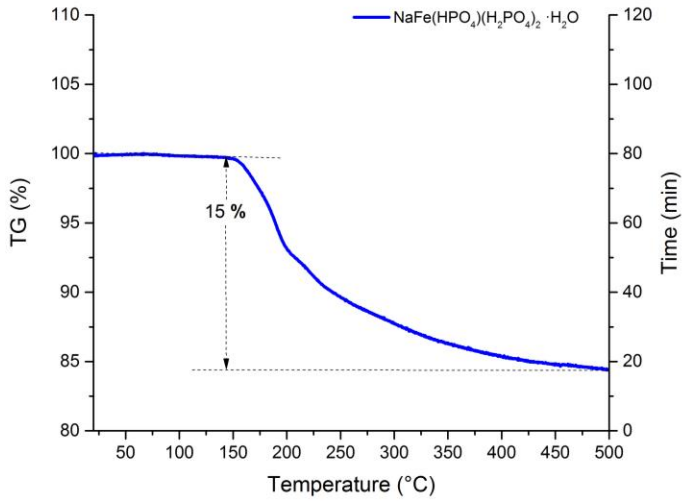

Figure 5.18. TGA curve for **Fe-4**.

5.3.3 Electrochemical characterisation

In order to evaluate the electrochemical activity of **Fe-4**, composite electrodes were prepared by mixing **Fe-4** with super S carbon and Ketjen black carbon in the weight ratio 60:15:15. These chemicals were mixed for 3.5 h using a Fritsch Pulverisette 7 mill. A solution of Kynar Flex 2801 in N-methyl-2-pyrrolidone (NMP) was then added as binder. The slurry obtained in this way was then cast on aluminium foil using a doctor blade. The final ratio of active material, conducting carbon and binder used in the composite electrodes was 60:30:10.

The coin cell batteries built in this way were then subject to galvanostatic cycling tests carried out in the potential range 1.2-4.5 V at various C-rates. The load curves correspond to sodium insertion and extraction and were obtained at a rate of 10 $mAhg^{-1}$ (C/10).

Following the data shown by the TGA, **Fe-4** was previously heated at 210 °C in order to remove the water present in the structure and improve the performance of this material as potential cathode for sodium batteries.

The data show the presence of a sloping potential with an average discharge voltage of 2.5 V *vs* Na^{+}/Na over the 1.2-4.5 V potential range. However, the material reaches capacity values far from the theoretical capacity (77.5 $mAhg^{-1}$). The shape on cycling is almost constant after the first cycle where the capacity reaches values of 16 $mAhg^{-1}$ (Figures 5.19). In addition, the Coulombic efficiency is very low with values around 1 $mAhg^{-1}$, indicating poor reversibility of the **Fe-4** during the sodium ion insertion (Figure 5.20).

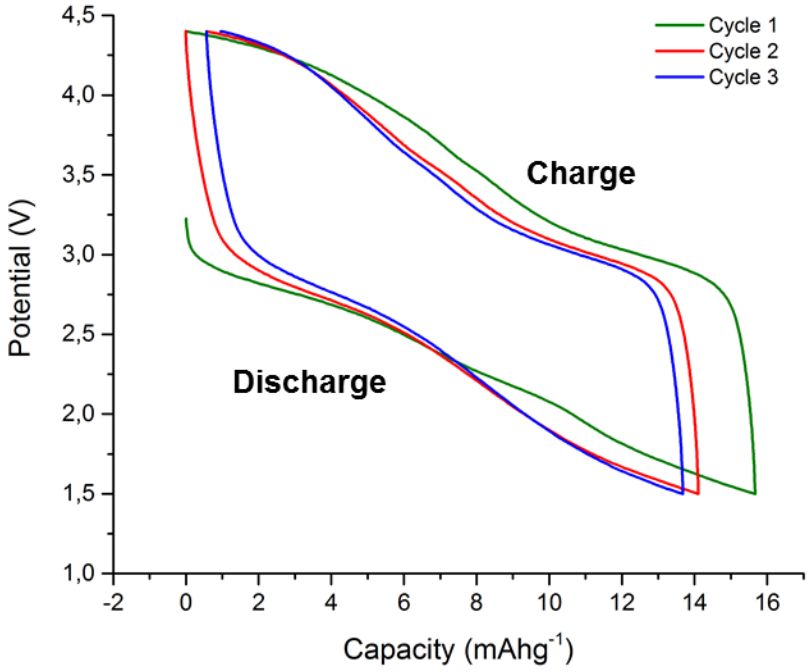

Figure 5.19. Load curves at a rate of C/10 (10 $mAhg^{-1}$) and a potential range 1.2-4.5 V (cycle 1-green, cycle 2-red, cycle 3-blue).

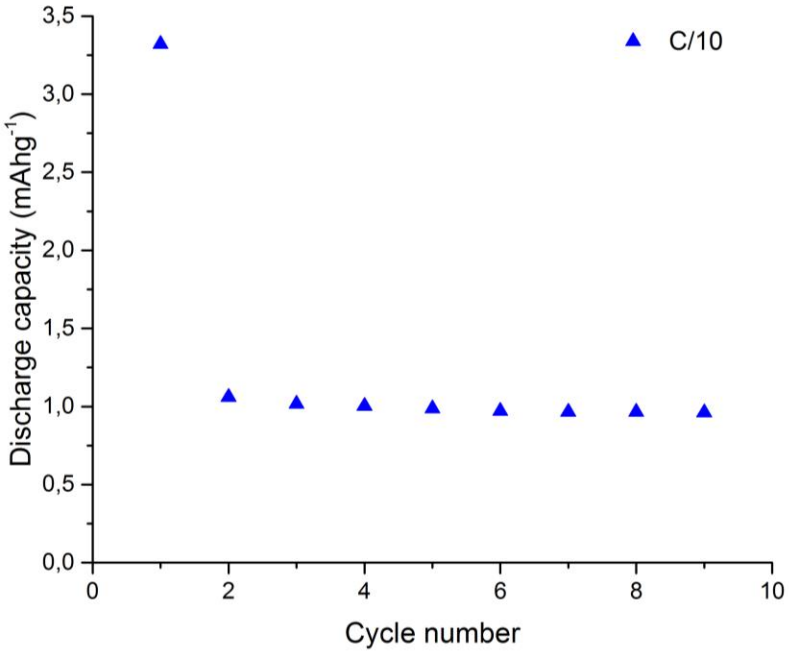

Figure 5.20. Discharge capacity *vs* cycle number for **Fe-4** at a rate of C/10 over the potential window 1.2-4.5 V.

5.3.4 Magnetic characterisation

In order to obtain greater insights into the magnetic properties of **Fe-4**, several measurements were performed in collaboration with Dr Lucy Clark at University of Edinburgh. In particular, measurements of the susceptibility (χ) and magnetisation (M) *versus* temperature were carried out.

The zero field cooled (ZFC) magnetic susceptibility measured in an applied field of 1 T is shown in Figures 5.23 and 5.24. It is possible to model the inverse magnetic susceptibility with a modified Curie-Weiss law (see Eq. 3.1) over the range 40-300 K to yield a Curie constant and a Weiss temperature value of C = 6.5 emu K/mol and Θ = -35.25 K, respectively.[39-41] However, even if the a negative value of the Weiss constant suggests the presence of antiferromagnetic correlations in the system, it has not been possible to observe any magnetic ordering transition in the **Fe-4** system. Indeed, the system does not appear to undergo a long-range ordering transition on the basis of the susceptibility data (Figure 5.21, 5.22, 5.23).

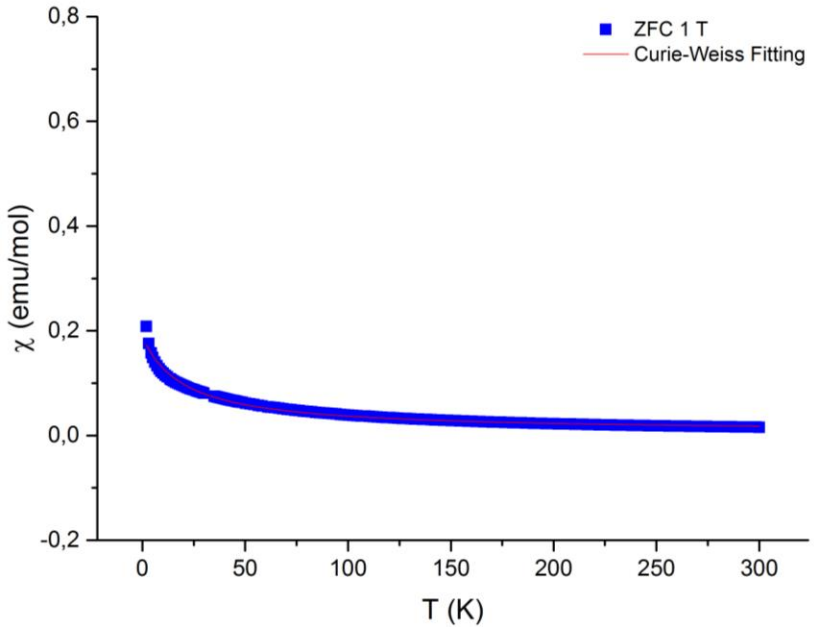

Figure 5.21. Susceptibility plot of **Fe-4**. with red line indicating the Curie-Weiss fit between 2 and 300 K.

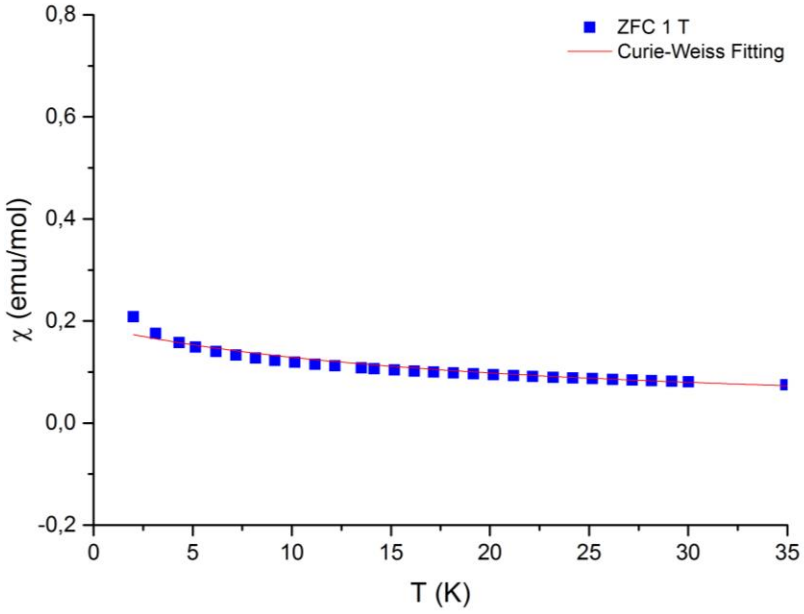

Figure 5.22. Zoom of the susceptibility plot between 2 and 35 K with red line indicating the Curie-Weiss fit between 2 and 300 K.

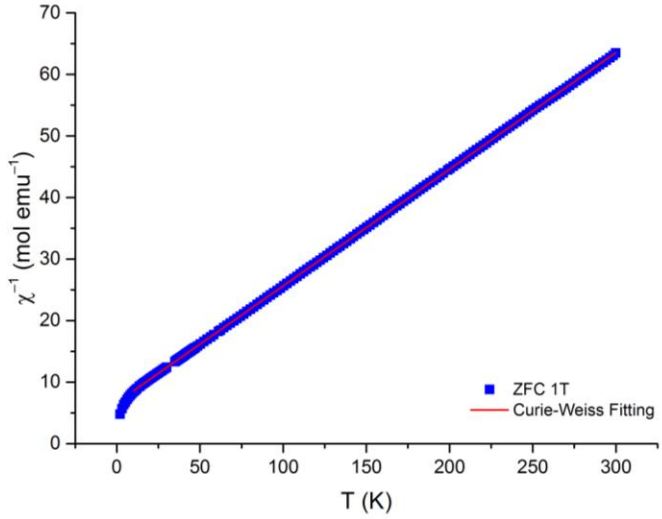

Figure 5.23. Inverse susceptibility plot of **Fe-4** with red line indicating the Curie-Weiss fit between 2 and 300 K.

5.4 Chapter conclusions

In this chapter two interesting iron based materials of formula $NaFe(H_2PO_3)_4$ and $NaFe(HPO_4)(H_2PO_4)_2 \cdot H_2O$ have been described. The phases have been synthesised by a low temperature cheap synthesis route.

Fe-3 and **Fe-4** exhibit framework crystal structures with open spaces running along all three dimensions, giving the possibility to intercalate and extract sodium ions. However, even if they are electrochemically active materials, both **Fe-3** and **Fe-4** show low observed capacity retentions, with an average discharge voltage of 2.5 V and a poor experimental capacity, far from the theoretical ones.

Fe-4 shows an interesting structural phase transition passing from a monoclinic crystal structure at low temperature (173 K) to an orthorhombic one at room temperature.

These compounds are therefore not suitable as new cathode materials for sodium batteries under the experimental conditions reported in this work.

5.5 References

1. R.E. Morris, M.P Attfield, A.K. Cheetham, *Acta Crystallogr. C*, 1994, **50**, 473.
2. G. Ritambhara, G. Shinde, P. Barpanda. "*Investigation of* $Nafe(PO_3)_3$ *and* $Na_3Fe_3(PO_4)_4$ *Orthophosphates for Sodium-Ion Batteries: Structural and Electrochemical Insight*.", PRiME 2016/230th ECS Meeting, 2016.
3. X. Lin, Y. Zhao, Y. Dong, Q. Kuang, Z. Liang, D. Yan, X. Liua, *Materials Science and Engineering B*, 2015, **197**, 58.
4. D. Kundu, E. Talaie, V. Duffort, L.F. Nazar, *Angew. Chem. Int. Ed.* 2015, **54**, 2.
5. J. Lu, S. C. Chung, S. Nishimura, A. Yamada, *Chem. Mater.*, 2013, **25**, 4557.
6. P. Moreau, D. Guyomard, J. Gaubicher, F. Boucher, *Chem.Mater.* 2010, **22**, 4126.
7. K. Saravanan, C.W. Mason, A. Rudola, K. H.Wong, P. Balaya, *Adv. Energy Mater.*, 2013, **3**, 444.
8. C.Jacoboni, C. Canali, G.. Ottaviani, A. Quaranta, Solid State Electron., 1977, **20**, 77.
9. N.E.Brese, M. O'Keeffe, *Acta Crystallogr.B.*, 1991, **47**, 192.
10. J. Loub, *Acta Crystallogr.B.*, 1991, **47**, 468.
11. K.Nakamoto, *Infrared and Raman Spectra of Inorganic and Coordination Compounds Part A*, John Wiley &Sons, 2009.
12. N. Anisimova, A. Ilyukhin, N. Chudinova, Z. Anorg. Allg. Chem., 1998, **624**, 1509.
13. J. Lu, S. C. Chung, S. Nishimura, A. Yamada, *Chem. Mater.*, 2013, **25**, 4557.
14. P. Moreau, D. Guyomard, J. Gaubicher, F. Boucher, *Chem.Mater.* 2010, **22**, 4126.

15. K. Saravanan, C.W. Mason, A. Rudola, K. H.Wong, P. Balaya, *Adv*. *Energy Mater.*, 2013, **3**, 444.

16. G. G. Amatucci, N. Pereira, *J. Fluorine Chem.*, 2007, **128**, 243.

17. B. L. Ellis, W. R. M. Makhanouk, Y. Makimura, K. Toughilland, L. F. Nazar, *Nat*. *Mater.*, 2007, **6**, 749.

18. N. Recham, J.-N. Chotard, L. Dupont, K. Djellab, M. Armand, J-M. Tarascon, *J. Electrochem*. *Soc.*, 2009, **156**, A993.

19. Y. Kawabe, N. Yabuuchi, M. Kajiyama, N. Fukuhara, T.Inamasu, R. Okuyama, I. Nakai, S. Komaba, *Electrochem*. *Commun.*, 2011, **13**, 1225.

20. Y. U. Park, D. H. Seo, H. S. Kwon, B. Kim, J. Kim, H. Kim, I. Kim, H. I. Yoo, K. Kang, *J. Am*. *Chem*. *Soc.*, 2013, **135**, 13870.

21. J. Barker, M. Y. Saidi, J. L. Swoyer, *Electrochem*. *Solid- State Lett.*, 2003, **6**, A1.

22. W. Song, X. Ji, Z. Wu, Y. Zhu, F. Li, Y. Yao, C. E. Banks, *RSC. Adv*., 2014, **4**, 11375.

23. P. Barpanda, G. Liu, C. D. Ling, M. Tamaru, M. Avdeev, S. C.Chung, Y. Yamada, A. Yamada, *Chem*. *Mater.*, 2013, **25**, 3480.

24. P. Barpanda, T. Ye, M. Avdeev, S. C. Chunga, A. Yamada, *J. Mater. Chem*. *A*, 2013, **1**, 4194.

25. P. Barpanda, J. Lu, T. Ye, M. Kajiyama, S. C. Chung, N. Yabuuchi, S. Komaba, A. Yamada, *RSC Adv*., 2013, **3**, 3857.

26. H. Kim, I. Park, D.-H. Seo, S. Lee, S.-W. Kim, W. J. Kwon,Y.-U. Park, C. S. Kim, S. Jeon, K. Kang, *J. Am*. *Chem*. *Soc.*, 2012, **134**, 10369.

27. H. Kim, I. Park, S. Lee, H. Kim, K.-Y. Park, Y.-U. Park, H. Kim, J. Kim, H.-D. Lim, W.-S. Yoon and K. Kang, *Chem. Mater.*, 2013, **25**, 3614.
28. L.P. Wang, L. Yu, X. Wang, M. Srinivasan, Z.J. Xu, *J. Mater. Chem. A*, 2015, **3**, 9353.
29. R.E. Morris, M.P Attfield, A.K. Cheetham, Acta Crystallogr. C, 1994, **50**, 473.
30. R. Gond, G. Shinde, P. Barpanda., Abstract MA2016-02 720, ECS Meeting abstracts, 2016.
31. X. Lin, Y. Zhao, Y. Dong, Q. Kuang, Z. Liang, D. Yan, X. Liua, *Materials Science and Engineering B*, 2015, **197**, 58.
32. J. Pizarro-Sanz, J. Dance, G. Villeneuve, M. Arriortua-Marcaida, *Mater. Lett.*, 1994, **18**, 327.
33. R. Tripathi, T. N. Ramesh, B. L. Ellis, L. F. Nazar, *Angew.Chem. Int. Ed.*, 2010, **49**, 8738.
34. R. Tripathi, T. N. Ramesh, B. L. Ellis, L. F. Nazar, *Angew.Chem. Int. Ed.*, 2010, **122**, 8920.
35. P. Barpanda, J.-N. Chotard, N. Recham, C. Delacourt, M. Ati,L. Dupont, M. Armand, J.-M. Tarascon, *Inorg. Chem.*, 2010, **49**, 7401.
36. M. Reynaud, G. Rousse, A. M. Abakumov, M. T. Sougrati, G. V. Tendeloo, J. N. Chotarda, J. M. Tarascon, *J. Mater. Chem.A*, 2014, **2**, 2671.
37. P. Barpanda, G. Oyama, C. D. Ling, A. Yamada, *Chem. Mater.*, 2014, **26**, 1297.
38. P. Barpanda, G. Oyama, S. Nishimura, S. C. Chung, A. Yamada, *Nat. Commun.*, 2014, **5**, 4358.
39. J. Ensling, P. Gutlich, R. Schmidt, R. Kniep, *Inorg. Chem.*, 1994, **33**, 3595.

40. V.M. Kovrugin, E.E. Gordon, E.E. Kasapbasi, M.H. Whangbo, M. Colomont, O.I. Siidra, S. Colis, S.V. Krivovichev, O. Mentré, *J. Phys. Chem. C*, 2016, **120**, 1650.
41. L.K. Elbouaanani, B. Malaman, R. Gerardin, *J. Solid State Chem.*, 1999, **148**, 455.

Chapter 6

Molybdenum Oxyfluoride Compounds: $Na_2MoO_2F_4$, $KNaMoO_2F_4$, $KMoO_2F_3$

6.1 Introduction

Perovskites represent a large structural family of compounds with crystal structures related to the $CaTiO_3$ mineral perovskite. In the ideal cubic perovskite (ABX_3), the *A* atom occupies the corner positions (0, 0, 0), the *B* atom sits in the centre position of the unit cell (½ , ½, ½) and the *X* atom occupies the face centred position (½ , ½, 0) of the unit cell. Many oxides adopt the perovskite structure with oxygen atoms as *X* atoms (ABO_3).The ideal cubic perovskite structure is not common and distorted versions of it with lower symmetry can be produced due to the different sizes of the atoms in the unit cell. When the BO_6 octahedra show tilts along different axes of the unit cell or the *B* atoms are displaced from their central positions, electric dipole properties may be produced and the perovskite structure modified in this way may show ferroelectricity.[1,2] There are many other physical properties commonly found in perovskites (*i.e.* magnetism and ionic conductivity) that can be altered by replacing the *A* or *B* atoms or creating vacancies removing either cations or anions.[3]

Previous reports about oxyfluoride perovskites containing ordered oxide and fluoride ions with the general formula $[MO_xF_{6-x}]^{n-}$ (x = 1, n = 2, and M = V^{5+}, Nb^{5+}, Ta^{5+}; x = 2, n = 2, and M = Mo^{6+}, W^{6+}; x = 2, n = 3, and M = V^{5+}, Nb^{5+}, Ta^{5+}; x = 3, n = 3, and M = Mo^{6+}) showing interesting magnetic and ferroelectric properties inspired the work described in this chapter.[2,4,14]

During this work, new classes of *A*-site deficient oxyfluoride perovskites $AA'MO_2F_4$ (where *A, A'* = K^+, Na^+ and *M* = Mo^{6+}) were targeted. In particular, the structural and electrochemical properties of new potential cathode materials for sodium batteries of formula $Na_2MoO_2F_4$, $KNaMoO_2F_4$ and $KMoO_2F_3$ are reported in this chapter.

6.2 Material synthesis

$Na_2MoO_2F_4$ hereinafter abbreviated "**Mo-1**" was synthesised hydrothermally by reaction of NaF (1 mmol) with MoO_3 (1 mmol), MoO_2 (1 mmol) and guanidinium carbonate (1 mmol). A 1:1 ratio of water (0.2 ml) and HF (48% aq.; 0.2 ml) was added to the resultant solution, without the addition of any other solvent. This mixture was sealed in a Teflon-lined stainless steel autoclave and heated to 160 °C for 2 days. The reaction was cooled to room temperature and transparent crystals were recovered by filtration from a minor aqueous phase. Guanidine is not incorporated into the product, but attempts to prepare this phase from similar reactions by omitting the guanidinium carbonate failed to produce the same product.

$KNaMoO_2F_4$ hereinafter abbreviated "**Mo-2**" was synthesised hydrothermally by reaction of KF (1 mmol) with $Na_2MoO_4{\cdot}2H_2O$ (1 mmol) and HF (48% aq.; 0.25 ml), without the addition of any other solvent. This mixture was sealed in a Teflon-lined stainless steel autoclave and heated to 160 °C for 2 days. The reaction was cooled to

room temperature and colourless air-stable crystals were recovered by filtration from a minor aqueous phase.

$KMoO_2F_3$ hereinafter abbreviated "**Mo-3**" was synthesised hydrothermally by reaction of KF (1 mmol) with LiF (1 mmol), MoO_3 (1 mmol) and HF (48% aq.; 0.20 ml), without the addition of any other solvent. This mixture was sealed in a Teflon-lined stainless steel autoclave and heated to 160 °C for 2 days. The reaction was cooled to room temperature and colourless air-stable crystals were recovered by filtration from a minor aqueous phase. Lithium is not incorporated into the product, but attempts to prepare this phase from similar reactions by omitting the lithium fluoride failed to produce the same product.

6.3 Structural characterisation

Mo-1, **Mo-2** and **Mo-3** crystals are well-faceted prismatic blocks with particle size about 250 μm, as shown in the SEM images (Figure 6.1).

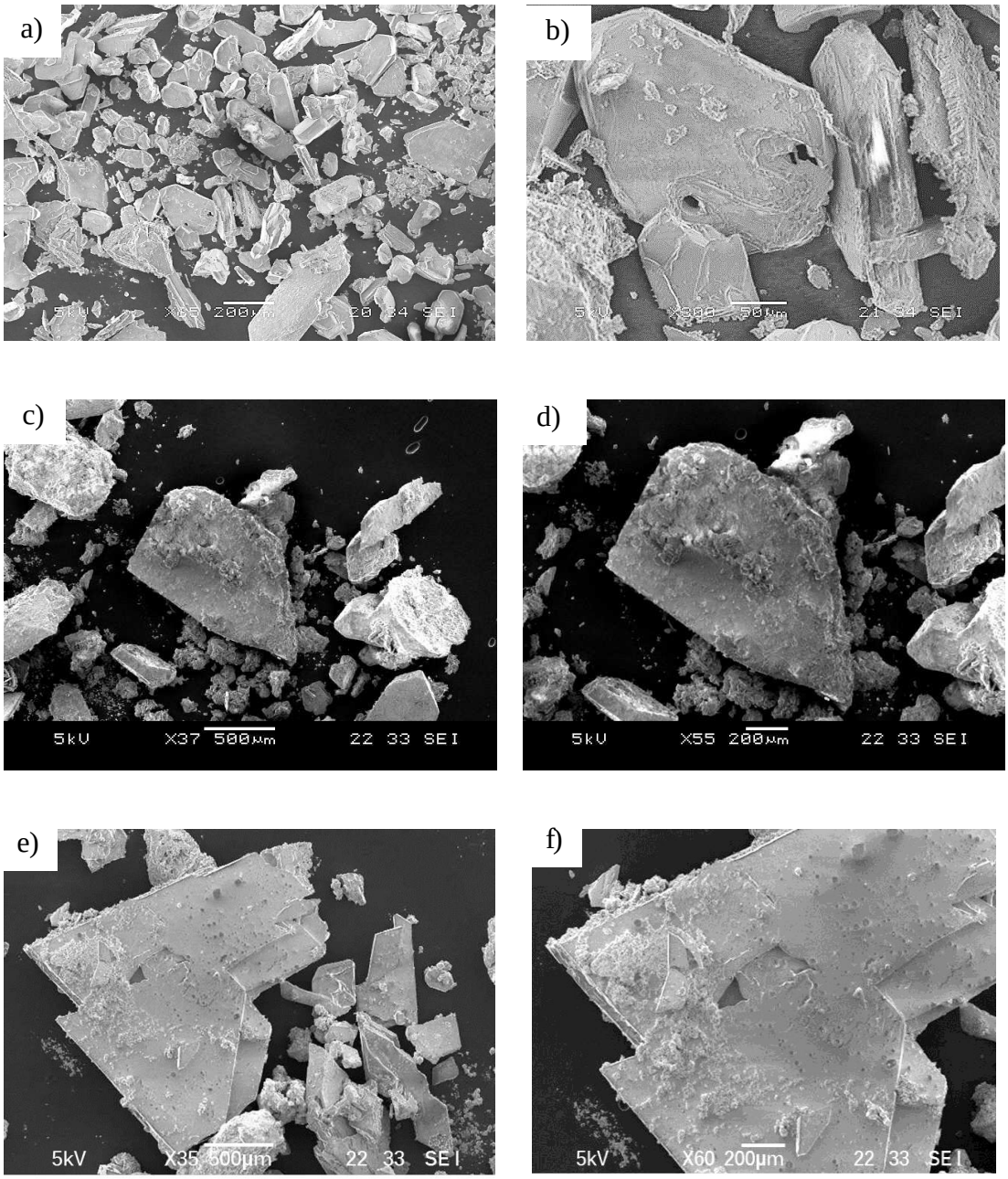

Figure 6.1. SEM pictures (left) and zoom-in (right) of typical a-b) **Mo-1**, c-d) **Mo-2** and e-f) **Mo-3** crystals.

The analysis of the single crystal X-ray diffraction data obtained for **Mo-1**, **Mo-2** and **Mo-3** suggest that these compounds adopt a monoclinic, tetragonal and orthorhombic crystal structure, respectively (Table 6.1, Figures 6.2-6.4).

Table 6.1. Crystallographic data for **Mo-1**, **Mo-2** and **Mo-3**.

Molecular formula	$Na_2MoO_2F_4$	$KNaMoO_2F_4$	$KMoO_2F_3$
Formula Mass (amu)	249.92	266.0	223.94
Crystal system	Monoclinic	Tetragonal	Orthorhombic
Space group	P 2_1/c	P 4/nmm	P $2_12_12_1$
a	5.4800(11) Å	5.8702(18)	11.3955(14)
b	5.7008(7) Å	5.869(3)	12.7750(9)
c	16.319(3) Å	8.4610(3)	11.8833(9)
α (°)	90.000(0)	90.000(0)	90.000(0)
β (°)	91.316(8)	90.16(2)	90.000(0)
γ (°)	90.000(0)	90.000(0)	90.000(0)
V (A^3)	509.7(6)	291.51(19)	1729.94(3)
Z	4	2	16
ρ (calcd) (g/cm^3)	1.628	1.52	3.44
Temp (K)	173(2)	173(2)	173(2)
F (000)	232	124	104
μ (mm^{-1})	1.375	1.522	3.949
R_{int}	0.0215	0.0467	0.0282
R_1/wR_2 (I >2σ)	0.0155/0.0582	0.0175/0.052	0.015/0.046
R_1/wR_2 (all data)	0.0167/0.0607	0.0162/0.054	0.015/0.047
Reflections number gt	1074	219	3838
Reflections number total	1126	222	3940
GOF on F^2	1.142	1.817	0.434

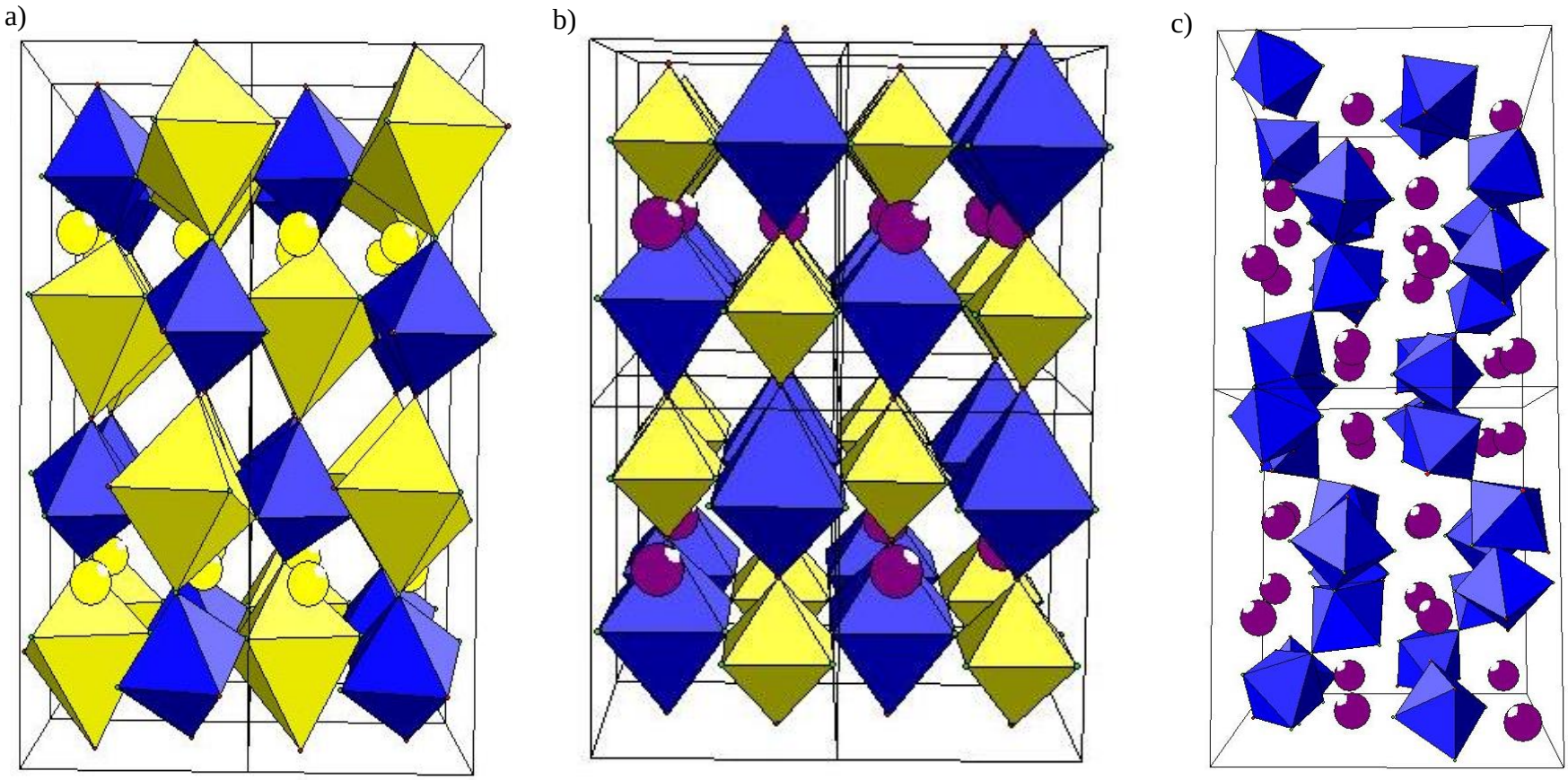

Figure 6.2. Polyhedral representation of a) **Mo-1**, b) **Mo-2** and c) **Mo-3** crystal structures along the *a*-axis. Mo-centred octahedra blue, Na-centred octahedra yellow, sodium ions in yellow and potassium ions in purple.

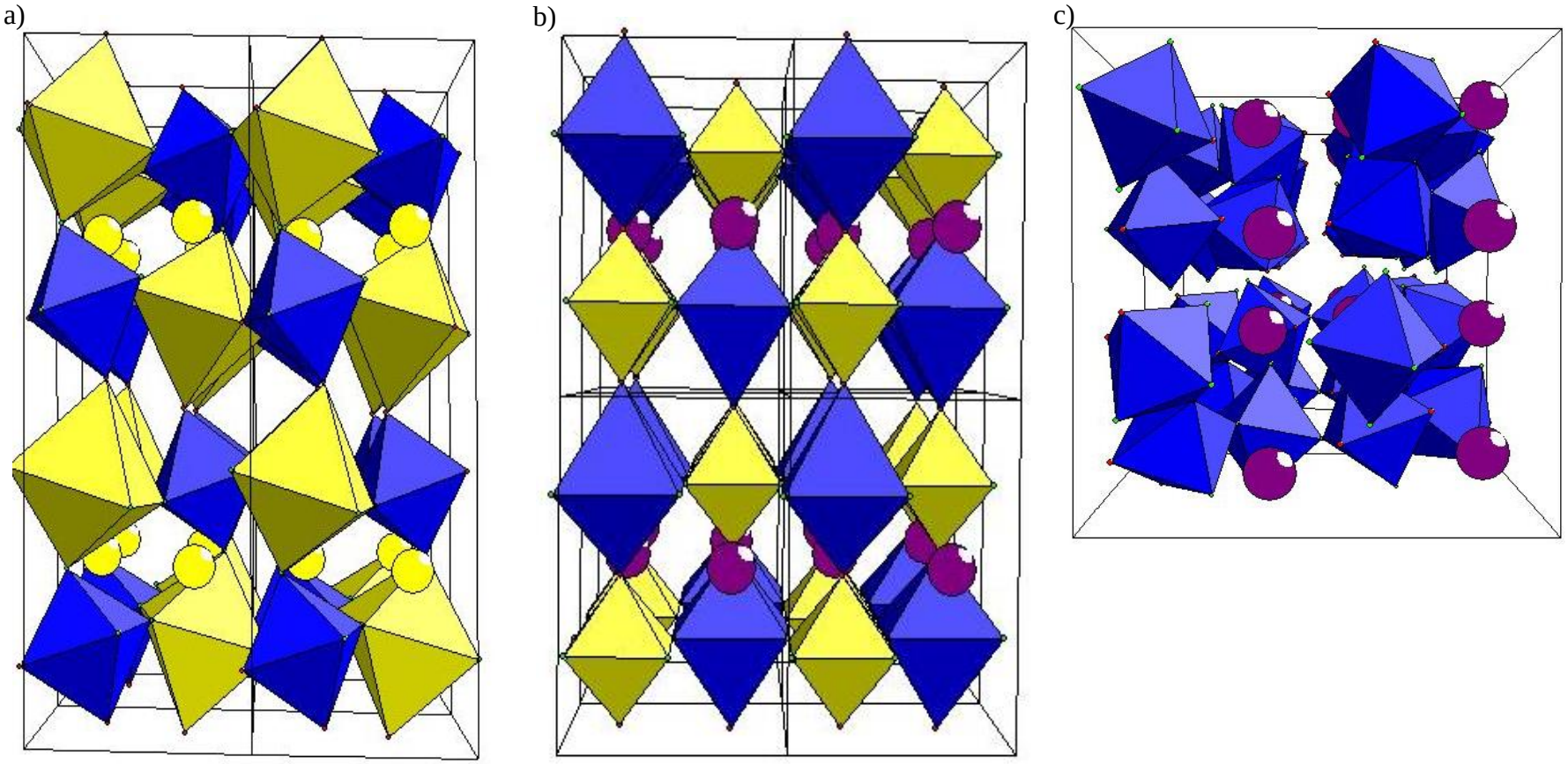

Figure 6.3. Polyhedral representation of a) **Mo-1**, b) **Mo-2** and c) **Mo-3** crystal structures along the *b*-axis. Mo-centred octahedra blue, Na-centred octahedra yellow, sodium ions in yellow and potassium ions in purple.

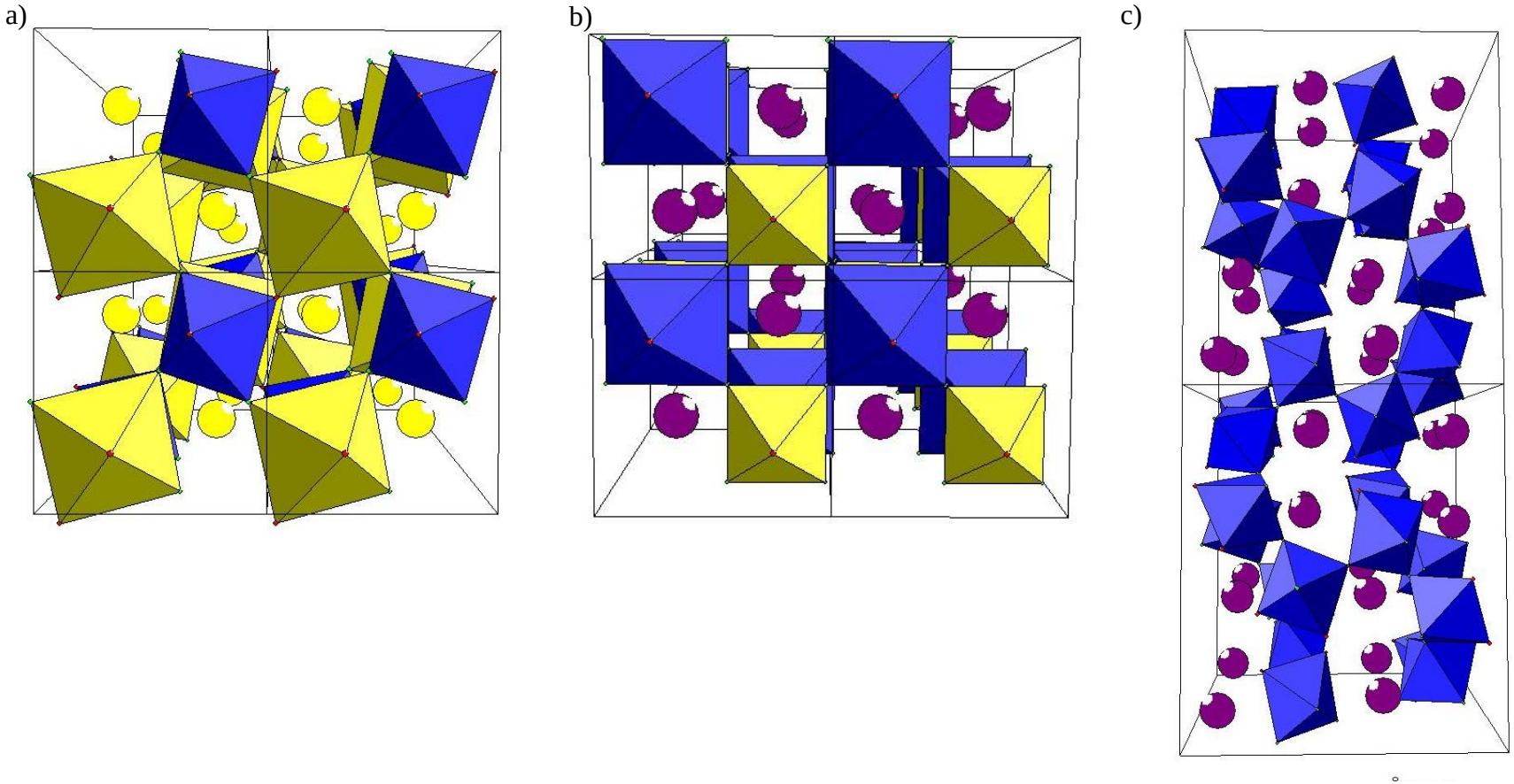

Figure 6.4. Polyhedral representation of a) **Mo-1**, b) **Mo-2** and c) **Mo-3** crystal structures along the *c*-axis. Mo-centred octahedra blue, Na-centred octahedra yellow, sodium ions in yellow and potassium ions in purple.

Mo-1 exhibits a unique variant of perovskite structure with sodium on both the *A* and *B* sites. Also, fully ordered sublattices are observed for the *A*-site (Na, vacancy), the *B*-site (Na, Mo) and the *X*-site (O, F) (Figure 6.5).

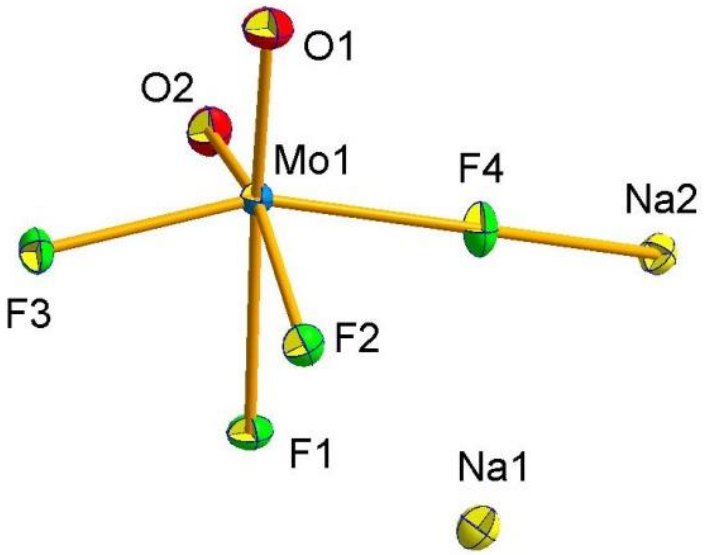

Figure 6.5. Asymmetric unit of **Mo-1**; molybdenum atom in blue, fluorine atoms in green, oxygen atoms in red, sodium ions in yellow.

In addition, **Mo-1** shows octahedral tilts around each of the principal axes. In particular, the principal axis of each octahedron does not match with the principal axis of the unit cell, leading to an octahedral tilting around *a*, *b* and *c*-axes. In order to better compare this tilting relationship with the ones already reported in the literature, it is useful to describe this tilting sequence as '*AACC*', where '*A*' represents anti-clockwise and '*C*' clockwise rotation of a single octahedron.[5] Looking at the literature, this tilt sequence is very rare and has been found only in other three perovskites, $NaNbO_3$,[6] $AgNbO_3$[7] and $Ca_{0.37}Sr_{0.63}TiO_3$.[8]

The tilting occurring along the *b*-axis of the monoclinic unit cell corresponds to simultaneous and equivalent 'out-of-phase' tilts around the *a* and *b* axes of the parent cubic cell (Figure 6.6).

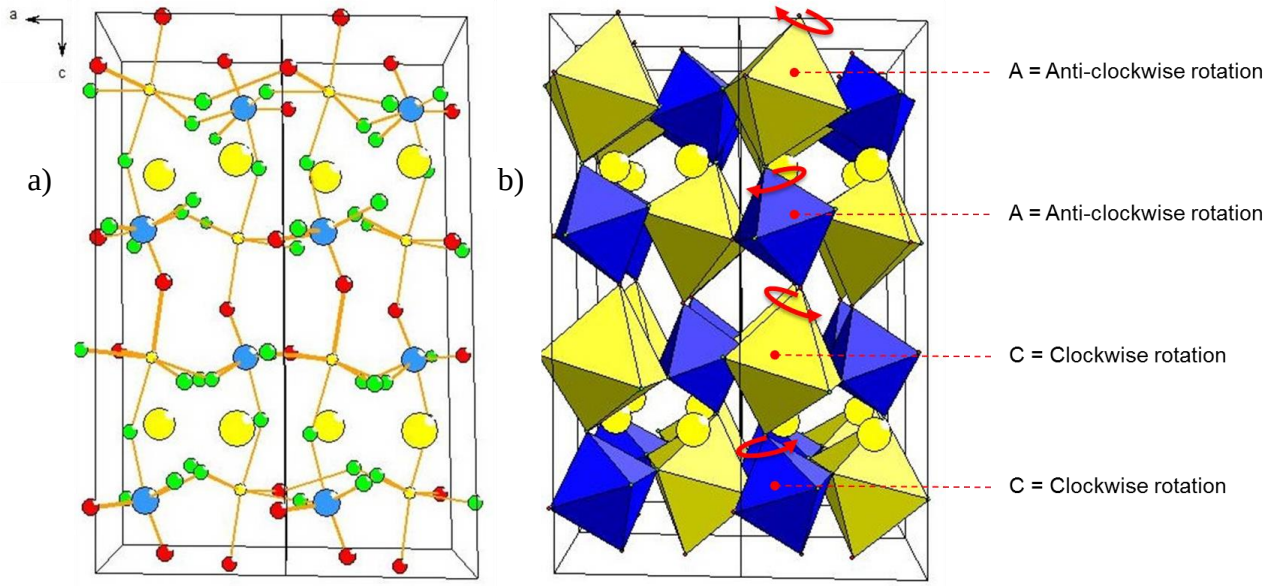

Figure 6.6. a) Unit cell packing and b) polyhedral representation of **Mo-1** with the "*AACC*" tilting sequence with the respective rotations along the *b*-axis (red arrows); molybdenum atoms in blue, fluorine atoms in green, oxygen atoms in red, Mo-centred octahedra in blue, Na-centred octahedral in yellow, sodium ions in yellow.

Looking at the tilting occurring around the *c*-axis, this is a more complex example, due to the 'in-phase', 'out-of-phase' and 'in-phase' tilts happening in sequence along this direction (Figure 6.7).

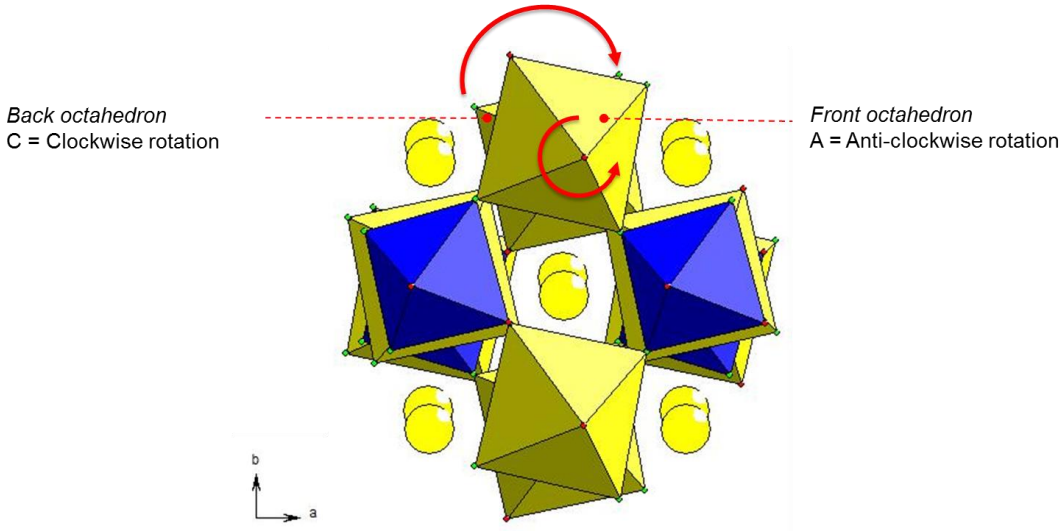

Figure 6.7. Polyhedral representation of **Mo-1** showing the details of the tilting sequence with the *A* and *C* rotations along the *c*-axis (red arrows); molybdenum atoms in blue, fluorine atoms in green, oxygen atoms in red, Mo-centred octahedra in blue, Na-centred octahedral in yellow, sodium ions in yellow.

The ordering on the *B*-site is relatively common in oxide perovskites due to the large size/charge difference of the two *B*-site cations.[3] On the other hand, the *A*-site ordering is relatively rare and it is facilitated by the tendency of the d^0 cation at the *B*-site to undergo a geometrical distortion (Jahn-Teller effect) in order to alleviate bond strains and reduce the overall energy.[3,9] In **Mo-1**, the *B*-site ordering is strongly correlated with the *A*-site ordering due to the two short Mo-O bonds in a *cis* configuration and O/F ordering, a common feature in Mo oxyfluorides (Table 6.2).[10-12] However, long-range ordering of O/F is less common in many d^0 cation oxyfluorides with perovskite-related structures, suggesting that the tilting observed for **Mo-1** is due to the tolerance factor effects normally associated with tilting in simpler perovskites.[13]

Due to this unusual atomic ordering and tilt scheme, **Mo-1** adopts a large low-symmetry unit cell. Its dimensions are approximately $\sqrt{2}\ a_P \times \sqrt{2}\ a_P \times 4\ a_P$, where a_P is the cubic aristotype perovskite unit cell parameter.

Mo-2 is an ordered oxide fluoride perovskite with the general formula *ABB'X*6, where K^+ occupies half the *A*-site positions, Na^+ and Mo^{6+} occupy the *B* and *B'* sites, respectively, and two O^{2-} and four F^- occupy the *X* sites. One of the two oxide ions is ordered together with its *trans* fluoride. The second one is disordered with the other three fluorides in the equatorial positions. However, even though this partial ordering between the oxide and fluoride ions is observed, the *A*- and *B*-site cations are both ordered. The *B*-site is occupied by Na^+ and Mo^{6+} which form corner-sharing octahedra without tilting. Half of the *A*-site positions are occupied by ordered K^+ cations in a layered arrangement, whereas in the adjacent layer where the axial oxides are located the *A*-site is vacant. This compound has been previously synthesised by Pinlac and co-workers using lower temperature (150 °C) and a shorter reaction time (24 hours).[14]

Mo-3 is a one-dimensional oxide fluoride with K^+ atoms and Mo^{6+} atoms forming corner-sharing octahedra which are linked together in spiral chains propagating along the *b*-axis. These octahedral chains form a quite complicated motif which can be better understood if K^+ atoms are removed from the polyhedral representation reported in Figure 6.8. The crystal structure contains *cis*-connected chains of Mo^{6+} atoms forming corner-sharing octahedral running along the *c*-axis similar to the ones reported in literature.[15]

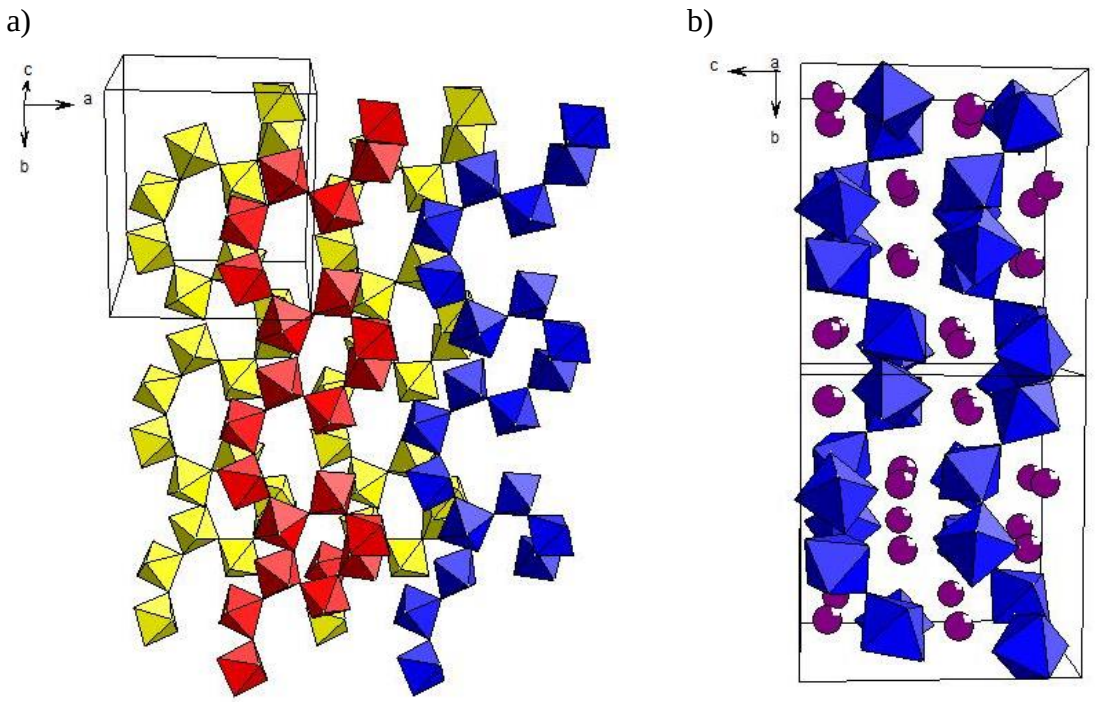

Figure 6.8. a) Distribution of octahedral [MoO_2F_3] chains and b) polyhedral representation of **Mo-3** crystal structure along the *c*-axis; molybdenum octahedral in blue, red and yellow, sodium ions in purple, fluorine atoms in green, oxygen atoms in red.

In order to investigate the chemical composition of **Mo-1**, **Mo-2** and **Mo-3** further and to confirm both the molybdenum oxidation state and the location of the O/F atoms, Energy-dispersive X-ray spectroscopy (EDX) and Bond Valence Sum (BVS) calculations were carried out. The qualitative EDX analysis confirmed the presence of oxygen, sodium, fluorine, molybdenum in the **Mo-1** compound, the presence of oxygen, sodium, fluorine, molybdenum and potassium in the **Mo-2** compound and the presence of oxygen, fluorine, molybdenum and potassium in the **Mo-3** compound (Figure 6.9).

The Bond Valance parameters relate bond valances and bond lengths (see Chapter 2, Section 2.3). The data obtained from the BVS calculations for **Mo-1**, **Mo-2** and **Mo-3**

using the Bond Valance parameters reported in literature for the Mo-O (1.907 Å) and the Mo-F (1.81 Å) bonds are in good agreement with the hypothesised valence state of the molybdenum (6+). The difference between the hypothesised valance state and the BVS calculations may be referred to the disorder and the partial occupancy effects in the **Mo-1**, **Mo-2** and **Mo-3** structures (Table 6.2).[16]

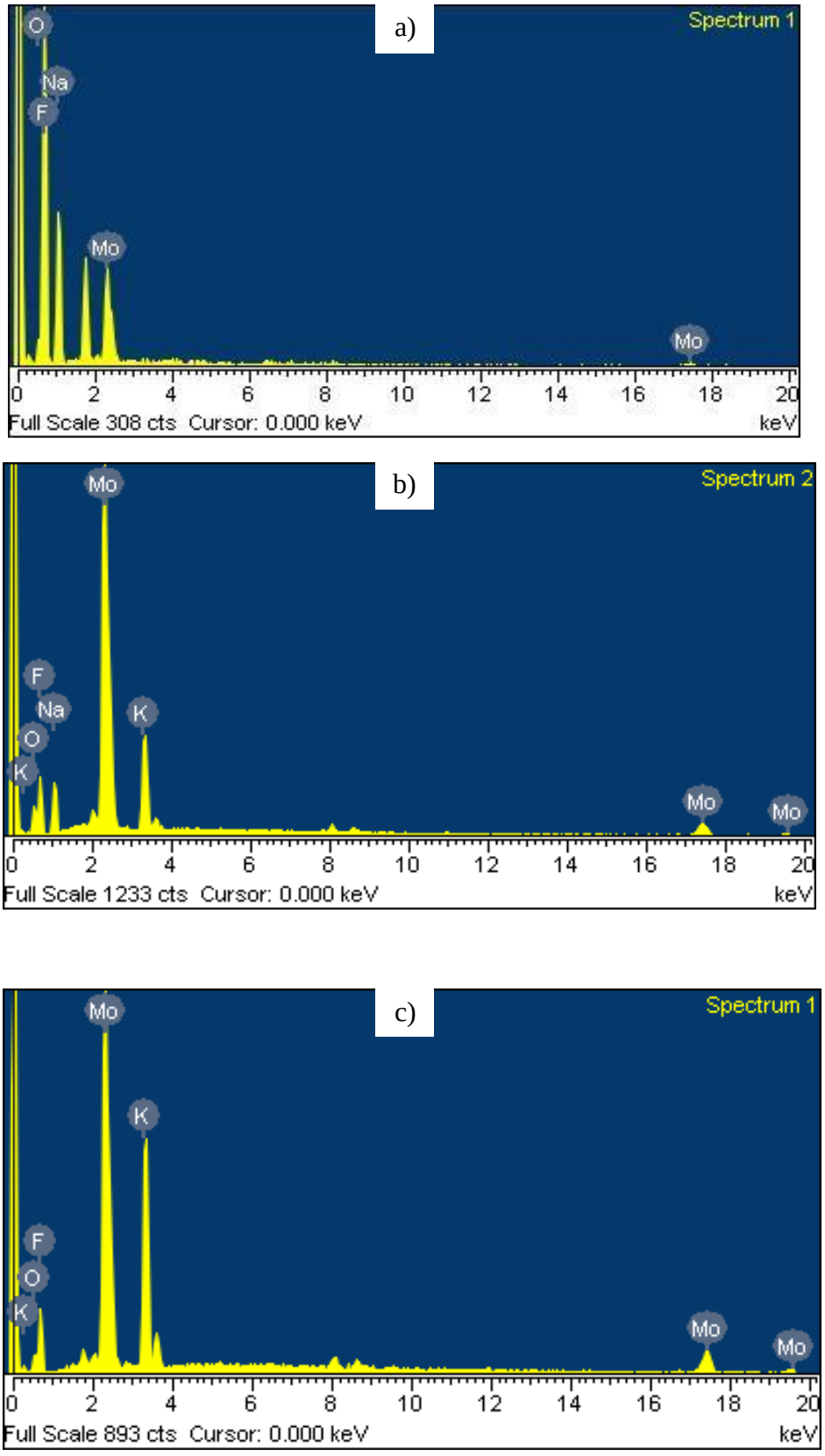

Figure 6.9. EDX spectra for a) **Mo-1**, b) **Mo-2** and c) **Mo-3**.

Table 6.2. Selected bond lengths and valence sums for **Mo-1**, **Mo-2** and **Mo-3**.

			Bond Length (Å)	Bond Valance
Mo-1	**Mo1**	O1	1.684(2)	1.827
		O2	1.727(1)	1.627
		F1	2.121(1)	0.431
		F2	2.050(1)	0.523
		F3	1.960(2)	0.667
		F4	1.916(2)	0.751
				∑ **5.826**
Mo-2	**Mo1**	O1	1.617(2)	2.191
		O2	1.873(1)	1.096
		F1	2.109(1)	0.446
		F2	2.050(1)	0.523
		F3	1.960(2)	0.666
		F4	1.916(2)	0.751
				∑ **5.673**
Mo-3	**Mo1**	O1	1.678(2)	1.852
		O3	1.707(2)	1.717
		F8	1.911(1)	0.761
		F9	1.916(1)	0.751
		F4	2.115(1)	0.439
		F5	2.177(1)	0.371
				∑ **5.891**
	Mo2	O6	1.683(2)	1.832
		O4	1.699(2)	1.754
		F12	1.919(1)	0.744
		F2	1.925(1)	0.733
		F4	2.107(1)	0.448
		F3	2.158(1)	0.391
				∑ **5.902**
	Mo3	O2	1.679(1)	1.852
		O7	1.688(2)	1.807
		F1	1.914(1)	0.755
		F10	1.927(1)	0.729
		F5	2.123(1)	0.431
		F7	2.206(1)	0.343
				∑ **5.917**
	Mo4	O5	1.684(1)	1.827
		O8	1.694(1)	1.778
		F6	1.896(1)	0.793
		F11	1.930(1)	0.723
		F3	2.157(1)	0.392
		F7	2.165(1)	0.383
				∑ **5.896**

The purity of the sample was verified by Powder X-ray diffraction (PXRD) experiments. The good match of the patterns suggests a good level of purity of the sample. Extra peaks at 17° and 33° correspond to the Teflon support used to carry out the powder diffraction measurements (Figure 6.10).

a)

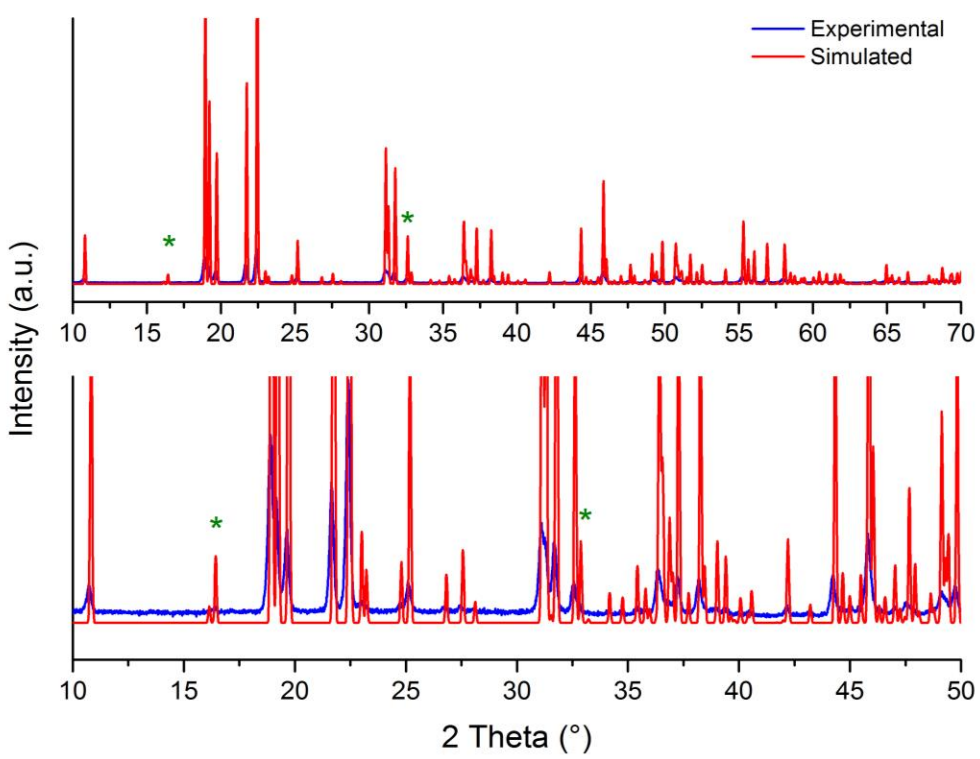

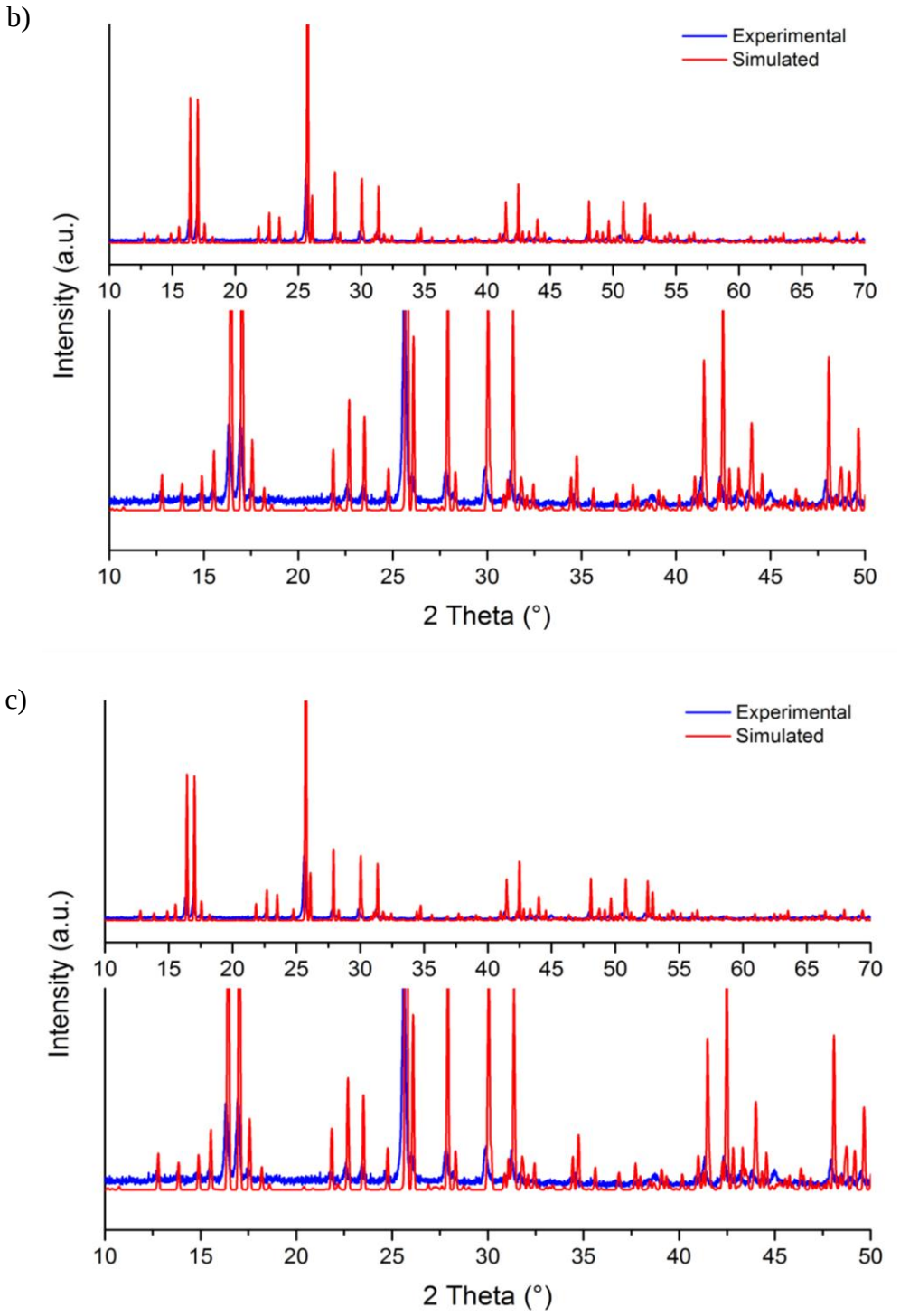

Figure 6.10. Observed and simulated PXRD pattern for a) **Mo-1**, b) **Mo-2** ad c) **Mo-3**: Experimental patterns in blue and calculated patterns from single crystal data in red; full pattern on the top, zoom-in of low angle region on the bottom. Peaks arising from the Teflon sample mounting are marked with an asterisk.

Infrared spectroscopy (IR) was used to determine the presence of Mo-O bonds in **Mo-1**, **Mo-2** and **Mo-3**. The IR spectra of **Mo-1**, **Mo-2** and **Mo-3** show a typical Mo-O stretch in the range 600-1000 cm^{-1} confirming the presence of Mo-O bonds in the **Mo-1**, **Mo-2** and **Mo-3** structures (Figure 6.11).[17]

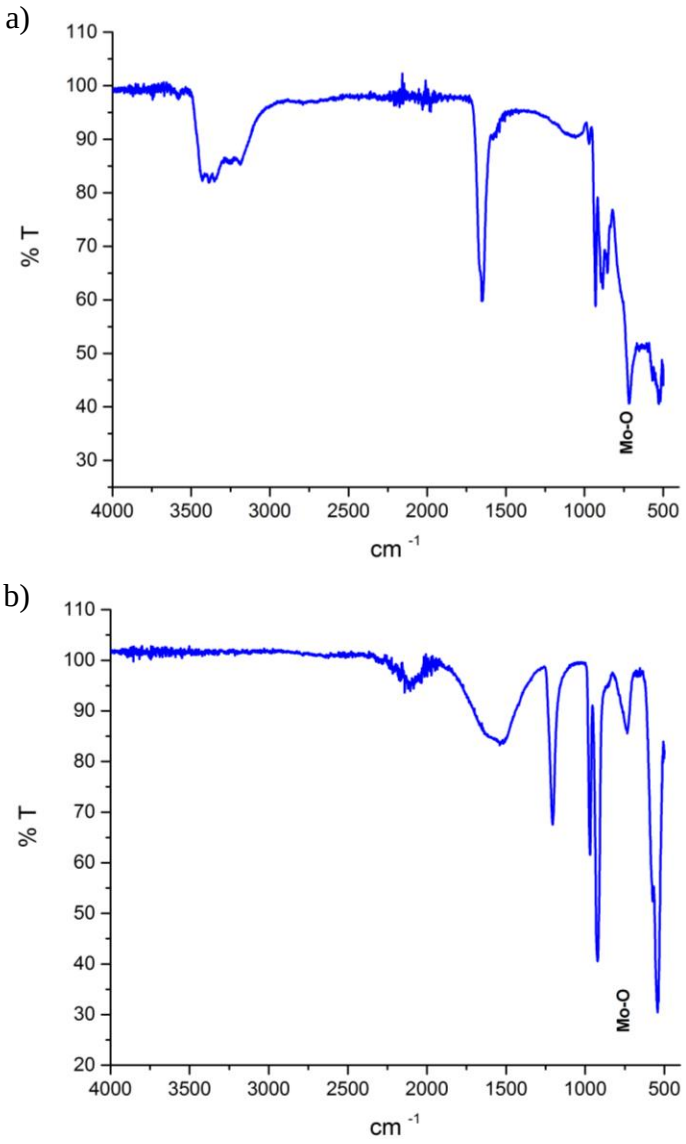

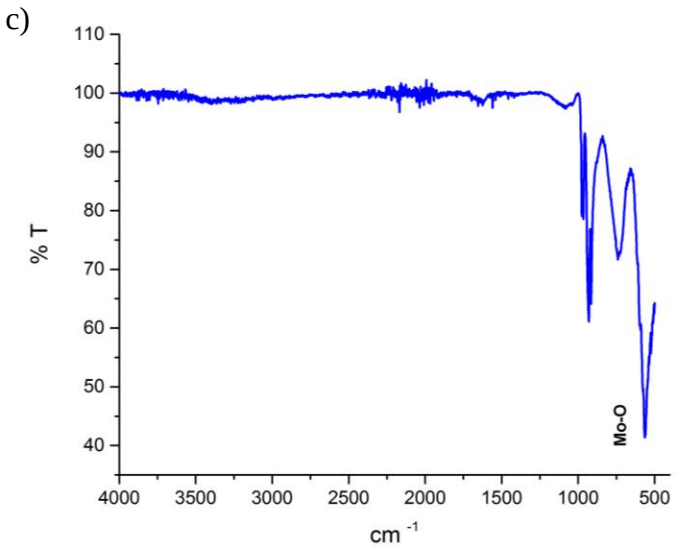

Figure 6.11. IR spectrum for a) **Mo-1**, b) **Mo-2** and c) **Mo-3**.

In order to characterise the temperature dependency of **Mo-1**, **Mo-2** and **Mo-3** from this point of view, Thermogravimetric analysis (TGA) was carried out. **Mo-1** and **Mo-2** show good stability without weight loss until 230 °C and 170 °C, respectively. A total weight loss of 19.3% and 19.8% up to 500 °C was then observed for **Mo-1** and **Mo-2**, respectively (Figures 6.12a and 6.12b). **Mo-3** shows a light weight loss of 2% until 250 °C and a total weight loss of 15% up to 500 °C (Figure 6.12c). The TGA data confirm the good thermal stability and the potential use of **Mo-1**, **Mo-2** and **Mo-3** as cathode materials.

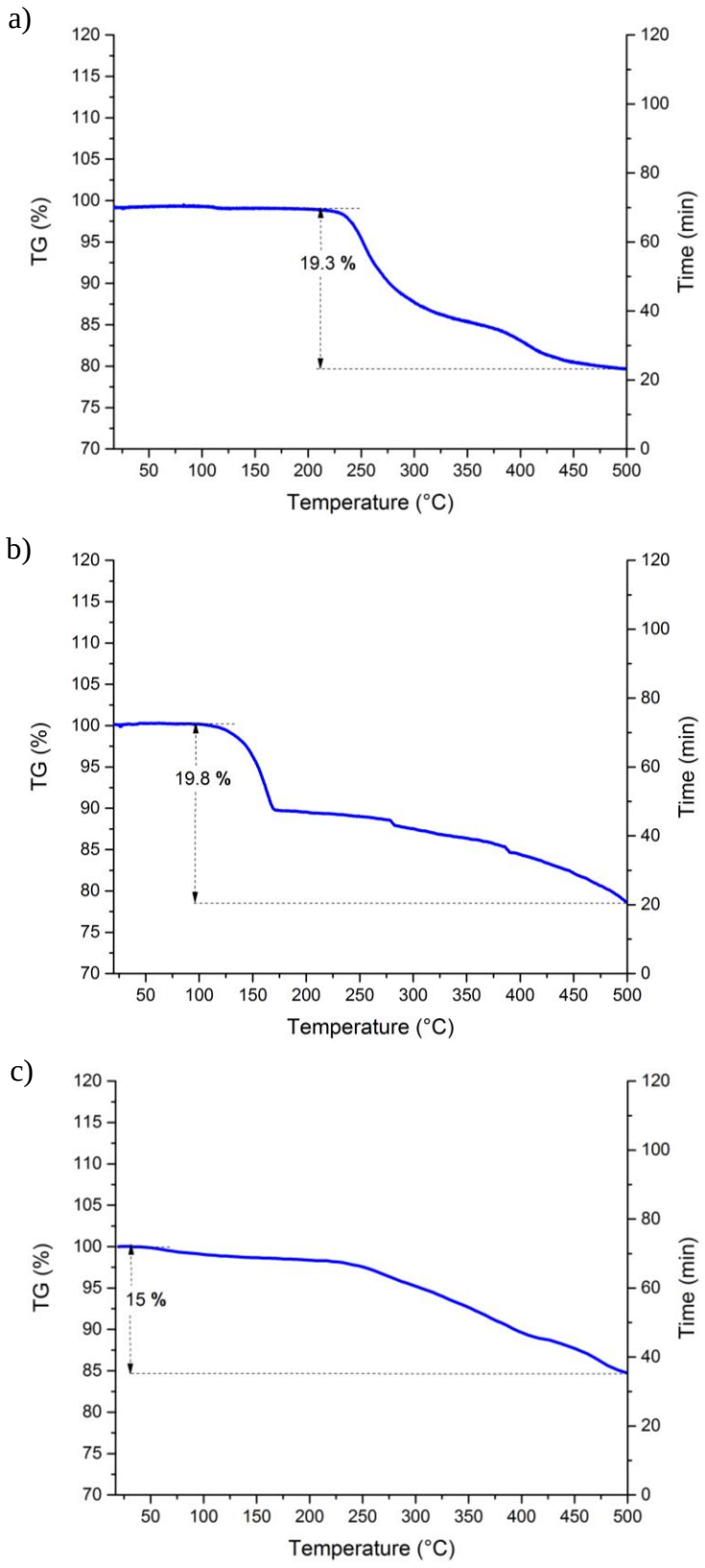

Figure 6.12. TGA curves for a) **Mo-1**, b) **Mo-2** and c) **Mo-3**.

6.4 Electrochemical characterisation

Oxyfluorides have received great attention as alternative cathode material for rechargeable batteries due to the modification of their physical properties by oxygen-fluoride replacement, as O^{2-} and F^- are anions of similar size.[18-21] This substitution is typical of different types of structures, including perovskite, and the relative difference in charge can be compensated by the reduction of the transition-metal's oxidation state.[18- 21] In addition, compounds containing fluorine have been proposed as battery materials due to the high electronegativity of the transition-metal-fluorine bond which leads to high ionicity and high redox potentials.[21-26] Interesting oxyfluoride-based nanomaterials are reported in the literature as potential materials for sodium batteries.[21,27-30] In order to evaluate the electrochemical activity of **Mo-1**, **Mo-2** and **Mo-3**, composite electrodes were prepared by mixing **Mo-1**, **Mo-2** and **Mo-3** with super S carbon and Ketjen black carbon in the weight ratio 60:15:15. These chemicals were mixed for 3.5 h using a Fritsch Pulverisette 7 mill. A solution of Kynar Flex 2801 in N-methyl-2-pyrrolidone (NMP) was then added as binder. The slurry obtained in this way was cast on aluminium foil using a doctor blade. The final ratio of active material, conducting carbon and binder used in the composite electrodes was 60:30:10. The coin cell batteries built in this way were then subject to galvanostatic cycling tests carried out at C/10 rate in the potential ranges 1.5-4.2 V for **Mo-1** and 1.5-4 V for **Mo-2** and **Mo-3**. The load curves correspond to sodium insertion and extraction and were obtained at a rate of 10 $mAhg^{-1}$ (C/10). **Mo-1**, **Mo-2** and **Mo-3** show capacity up to 35 $mAhg^{-1}$ in the potential range 1.5-4.2 V. Even if the discharge capacity shows a good stability for **Mo-1**, **Mo-2**, overall the discharge capacity values are weak for all the three structures (Figure 6.13).

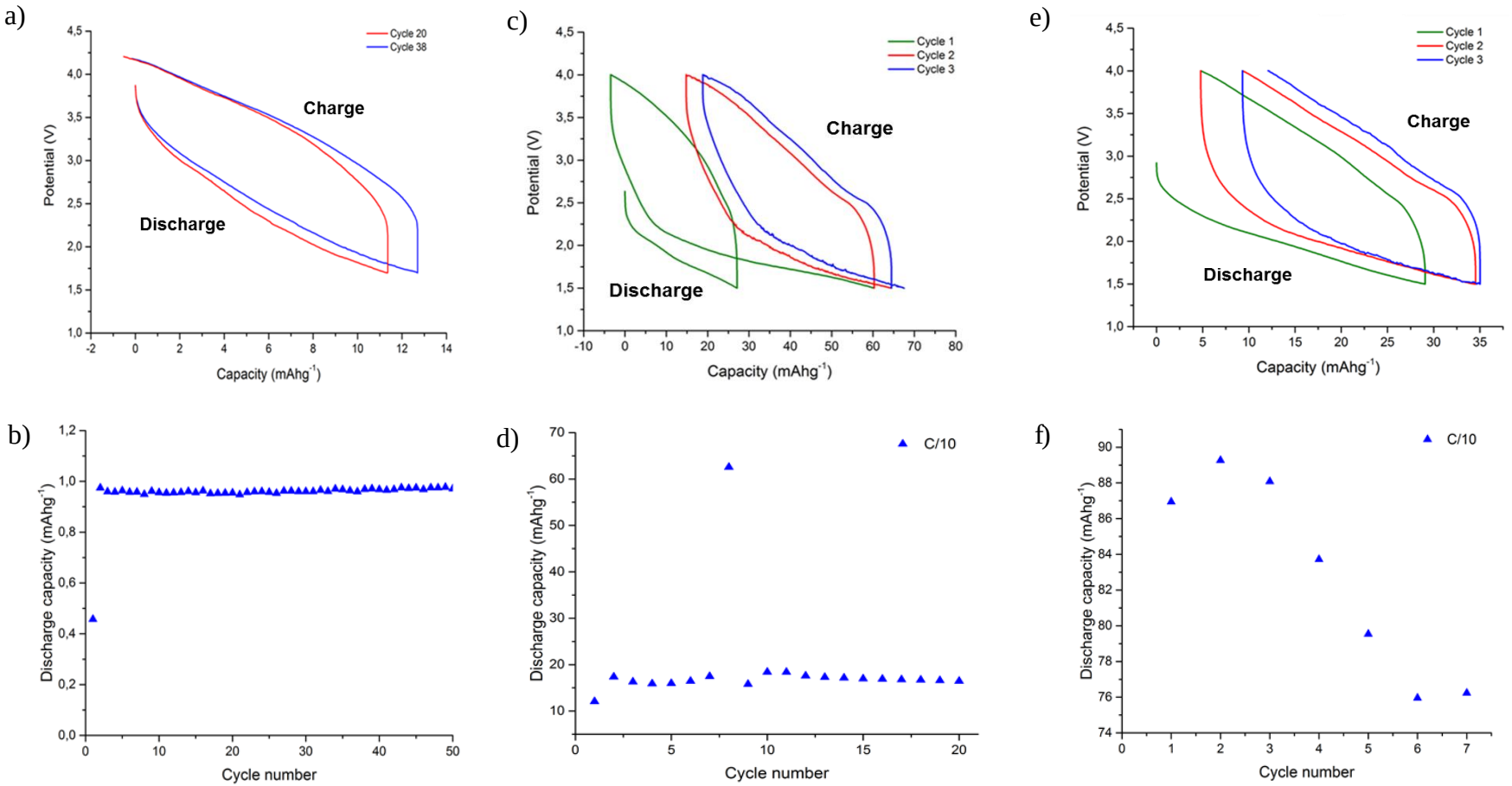

Figure 6.13. Load curves at a rate of C/10 (10 $mAhg^{-1}$) and a potential range of 1.5-4.2 V for a-b) **Mo-1** and in the potential range of 1.5-4 V for c-d) **Mo-2** and e-f) **Mo-3**.

6.5 Magnetic characterisation

According to the single crystal X-ray diffraction data, the **Mo-1** crystal structure can be well-modelled on the basis of an ideal stoichiometry $Na_2MoO_2F_4$, suggesting the presence of Mo^{6+} which is supported by the BVS calculations. However, the **Mo-1** crystals are characterised by a light blue colour, typical of the Mo^{5+} ion. In order to confirm the oxidation state of the molybdenum present in **Mo-1**, magnetic measurements were carried out by Dr. Hajime Ishikawa at the Institute for Solid State Physics of the University of Tokyo.

The zero field cooled (ZFC) magnetic susceptibility obtained in an applied field of 1 T was measured by a SQUID magnetometer (MPMS3, Quantum Design). The magnetic susceptibility increases drastically at low temperatures (Figures 6.14). This behaviour confirms that the main contribution to susceptibility comes from Mo^{5+} ions with localised spin of -1/2 according to a slightly modified formula $Na_2MoO_{2-\delta}F_{4+\delta}$.

It is possible to model the inverse magnetic susceptibility with the Curie law over the range 2-300 K represented in Equation 6.1.

$$\chi = \chi_0 + \frac{C}{T} \qquad \text{Eq. 6.1}$$

The temperature-independent term represented by χ_0 is equal to 2.34 x 10^{-5} emu/mol and the Curie constant (C) shows value of 0.0301 emu K mol^{-1} (Figure 6.15). The expected value of *C* for spin -1/2 is equal to 0.375 emu K mol^{-1}, meaning that the

observed Curie constant is equal to the 8% of the expected value. This suggests that approximately 8% of Mo ions in $Na_2MoO_{2-\delta}F_{4+\delta}$ exist as Mo^{5+} ions ($\delta \sim 0.08$).

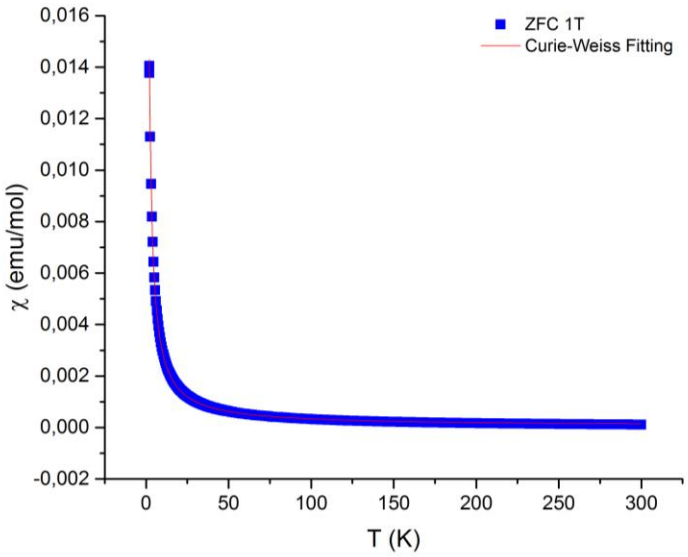

Figure 6.14. Susceptibility plot of **Mo-1** with red line indicating the Curie-Weiss fit between 2 and 300 K.

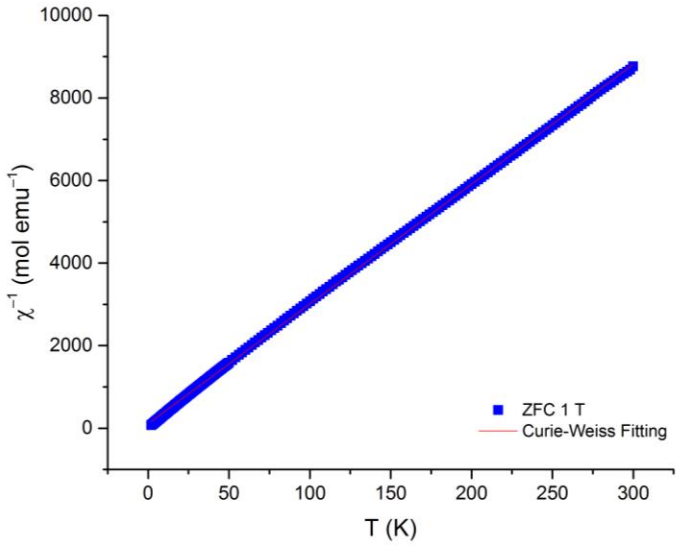

Figure 6.15. Inverse susceptibility plot of **Mo-1** with red line indicating the Curie-Weiss fit between 2 and 300 K.

6.6 Chapter conclusions

In this chapter, new examples of *A*-site deficient oxyfluoride perovskites $Na_2MoO_2F_4$ (**Mo-1**) and $KNaMoO_2F_4$ (**Mo-2**) were reported in addition to a novel chain-structure oxyfluoride, $KMoO_2F_3$ (**Mo-3**).

Mo-1 exhibits a unique variant of the perovskite structure with sodium on both the *A* and *B* sites. Also, fully ordered sublattices involve the *A*-site (Na, vacancy), the *B*-site (Na, Mo) and the *X*-site (O, F). In addition, **Mo-1** shows octahedral tilts around each of the principal axes. In particular, the octahedral tilting scheme corresponds to simultaneous and equivalent 'out-of-phase' tilts around the *a* and *b* axes of the parent cubic cell. The tilting around the *c*-axis is a more complex due to the 'in-phase', 'out-of-phase' and 'in-phase' tilts occurring in sequence along this direction.

Mo-2 is a layered oxide fluoride perovskite characterised by an $ABB'X_6$ formula where the *A*-site positions are half occupied by K^+, the *B* and *B'* sites are occupied by Na^+ and Mo^{6+} , respectively, and the *X* site is occupied by two O^{2-} and four F^-. Since the *B*-site is occupied by Na^+ and Mo^{6+}, corner-sharing octahedra without tilting are present in the structure.

Mo-3 is a novel oxide fluoride characterised by corner-sharing octahedra formed by Mo^{6+} atoms. These octahedra occupy the unit cell forming long zig-zag chains.

These interesting materials show open spaces running along all three dimensions, giving the potential possibility to intercalate and extract sodium ions into the open channels. Electrochemical studies were carried out in order to evaluate their potential use as cathode materials for sodium batteries However, the electrochemical properties and observed capacity retention showed in the tests performed during this PhD project are

limited, suggesting that these compounds are not suitable under these experimental conditions.

The whole work and more detailed measurements related to **Mo-1** were published in *Chemical Communications*: H. Ishikawa,‡ **I. Munaó**,‡ B.D. Bode, Z. Hiroi, P. Lightfoot, *Chem. Commun.*, 2015, **51**, 15469. (‡ These authors contributed equally to this work).

6.7 References

1. P.K. Davies, H. Wu, A.Y. Borisevich, I.E. Molodetsky, L. Farber, *Annu. Rev. Mater. Res.*, 2008, **38**, 369.
2. A.M. Glazer, *Acta Crystallogr.B*, 1972, **28**, 3384
3. G. King, P.M. Woodward, *J. Mater. Chem*., 2010, **20**, 5785.
4. H. Shorafa, H. Ficicioglu, F. Tamadon, F. Girgsdies, K. Seppelt, *Inorg. Chem*., 2010, **49**, 4263.
5. M.D. Peel, S.E. Ashbrook, P. Lightfoot, *Inorg. Chem*., 2012, **51**, 6876.
6. A.C. Sakowski-Cowley, K. Lukaszewicz, H.. Megaw, *Acta Crystallogr.B*, 1969, **25**, 851.
7. J. Fábry, Z. Zikmund, A. Kania, V. Petricek, *Acta Crystallogr.C*, 2000, **56**, 916.
8. C.J. Howard, R.L. Withers, K.S. Knight, Z. Zhang, *J. Phys. Condens. Matter*, 2008, **20**, 135202
9. P.N. Iyer, A.J. Smith, *Acta Crystallogr*., 1967, **23**, 740
10. P.A. Maggard, A.L. Kopf, C. L. Stern, K.R. Poeppelmeier, K.M. Ok, P S Halasyamani, *Inorg. Chem*., 2002, **41**, 4852.
11. D.W. Aldous, P. Lightfoot, *J. Fluor. Chem*., 2012, **144**, 108.
12. F.H. Aidoudi, C. Black, K.S.A. Arachchige, A.M.Z. Slawin, R.E. Morris, P. Lightfoot, *Dalton Trans*., 2014, **43**, 568.
13. I.N. Flerov, M.V. Gorev, A.Tressaud, N.M. Laptash, *Crystallogr. Rep*., 2011, **56**, 9.
14. R.A.F. Pinlac, C.L. Stern, K.R. Poeppelmeier, *Crystals*, 2011, **1**, 3.
15. R. Von Der Mühll, F. Daut, J. Ravez, *J. Solid State Chem.*, 1973, **8**, 206.
16. N.E.Brese, M. O'Keeffe, *Acta Crystallogr.B.*, 1991, **47**, 192.

17. J. Sheng, K. Tang, W. Cheng, J. Wang, Y. Nie, Q.J. Yang, *Hazard. Mater.*, 2009, **171**, 279.

18. P. Hagenmuller, *Inorganic Solid Fluorides: Chemistry and Physics*, Academic Press: New York, 1985.

19. R.D. Shannon, *Acta Crystallogr. A*, 1976, **32**, 751.

20. A. Simon, R. Ravez, *Ferroelectrics*, 1980, **24**, 305

21. H. Shorafa, H. Ficicioglu, F. Tamadon, F. Girgsdies, K. Seppelt, *Inorg. Chem.*, 2013, **52**, 9791.

22. G.G. Amatucci, N.J. Pereira, *Fluorine Chem.*, 2007, **128**, 243.

23. J. Barker, M.Y. Saidi, J.L. Swoyer, *J. Electrochem. Soc.*, 2003, **150**, A1394.

24. N. Recham, J.N. Chotard, L. Dupont, C. Delacourt, W. Walker, M. Armand, J.M. Tarascon, *Nat. Mater.*, 2010, **9**, 68.

25. M. Bervas, L.C. Klein, G.G. Amatucci, *J. Electrochem. Soc.*, 2006, **153**, A159.

26. J. Cabana, L. Monconduit, D. Larcher, M.R. Palacin, *Adv. Mater.*, 2010, **12**, 315.

27. M. Nishijima, I.D. Gocheva, S. Okada, T. Doi, J.I. Yamaki, T. Nishida, *J. Power Sources*, 2009, **190**, 558.

28. A. Kitajou, H. Komatsu, K. Chihara, I.D. Gocheva, S. Okada, J.I. Yamaki, *J. Power Sources*, 2012, **198**, 389.

29. E.M. Sorensen, H.K. Izumi, J.T. Vaughey, C.L. Stern, C. L., K.R. Poeppelmeier, *J. Am. Chem. Soc.*, 2005, **127**, 6347.

30. F. Sauvage, V. Bodenez, H. Vezin,T.A. Albrecht, J.M. Tarascon, K.R. Poeppelmeier, *Inorg. Chem.*, 2008, **47**, 8464.

Chapter 7

Conclusions

Recent concerns over the sustainability and the availability of the resources for alkali ions have pushed the development of low cost batteries with high energy densities that can meet a variety of applications. Sodium ion batteries have been shown to be promising candidates especially for stationary energy storage applications.

In this thesis, exploratory studies on the synthesis and characterisation of new cathode materials for second generation sodium batteries have been reported, with a particular emphasis on preparing new iron-phosphite and molybdenum oxyfluoride materials.

The most suitable candidate for this purpose reported in this work is $NaFe_3(HPO_3)_2[(H,F)PO_2OH)_6]$, abbreviated in **Fe-1**. This compound is characterised by a new 3D framework structure with both interesting electrochemical and magnetic properties. It is very stable upon sodium intercalation and extraction and shows excellent capacity retention together with good cycling stability, Coulombic efficiencies close to 100%, an average discharge voltage of 3 V and an experimental capacity of 60 $mAhg^{-1}$ close to the theoretical one (99 $mAhg^{-1}$).

The compound $Fe_2(HPO_3)_3$, abbreviated in **Fe-2**, is an electrochemically-active material with good capacity retention. Its 3D framework structure exhibits good stability upon sodium intercalation and extraction. However, the capacity values reached by **Fe-2** are

far from the theoretical capacity and the Coulombic efficiency is low, resulting in a poor electrochemical activity of this material.

The compounds $NaFe(H_2PO_3)_4$ abbreviated **Fe-3** and $NaFe(HPO_4)(H_2PO_4)_2 \cdot H_2O$ abbreviated **Fe-4** exhibit novel 3D framework crystal structures with open spaces running along all three dimensions, giving the possibility for intercalation and extraction of sodium ions. **Fe-4** is also characterised by an interesting structural phase transition, passing from a monoclinic crystal structure at low temperature (173 K) to an orthorhombic geometry at room temperature (293 K). However, even if **Fe-3** and **Fe-4** are electrochemically-active materials being stable upon sodium insertion and extraction, **Fe-3** and **Fe-4** are characterised by poor capacity retentions.

New examples of *A*-site deficient oxyfluoride perovskites are reported: $Na_2MoO_2F_4$ abbreviated **Mo-1**, $KNaMoO_2F_4$ abbreviated **Mo-2** and a novel chain-structure oxyfluoride of formula $KMoO_2F_3$ abbreviated **Mo-3**. The compound **Mo-1** exhibits a unique variant of perovskite structure with Na on both the *A* and *B* sites. In addition, it shows a fully ordered sublattice involving simultaneous ordering at the *A*-site (Na, vacancy), the *B*-site (Na, Mo) and the *X*-site (O, F), together with octahedral tilts around each of the principal axes. This octahedral tilting scheme corresponds to simultaneous and equivalent 'out-of-phase' tilts around the *a* and *b* axes of the parent cubic cell. The tilting around the *c*-axis is more complex due to the 'in-phase', 'out-of-phase' and 'in-phase' tilts occurring in sequence along this direction. **Mo-2** is a layered oxide fluoride perovskite characterised by an $ABB'X_6$ formula where the *A*-site positions are half occupied by K^+, the *B* and *B'* sites are occupied by Na^+ and Mo^{6+}, respectively, and the *X* site is occupied by two O^{2-} and four F^-. **Mo-2** does not show octahedral tilting due to the fact that the *A*-site is occupied by the larger K^+ cation. The third example of

molybdenum oxyfluoride reported in this thesis is **Mo-3**, which is a novel oxyfluoride characterised by corner-sharing octahedra formed by Mo^{6+} atoms. These octahedra occupy the unit cell forming long zig-zag chains. Compounds **Mo-1**, **Mo-2** and **Mo-3** exhibit open spaces running along all three dimensions, giving the possibility to intercalate and extract sodium ions. However, their electrochemical properties and the observed capacities are limited suggesting that these compounds are not suitable new cathode materials for second generation sodium batteries under the experimental conditions employed in this PhD project.

Further investigations of the structures reported in this thesis involving different synthetic methods and electrochemical characterisation would be of interest. In particular, the ionothermal synthetic method uses ionic liquids instead of water as a solvent. Ionic liquids are characterised by good solvent properties, high stability upon temperature changes and low volatility, facilitating in this way the nucleation. For these reasons, it would be of interest to synthesise new fluoride frameworks compounds based on the structures reported in this PhD thesis using ionic liquids as solvent. Going further, Metal Organic Framework compounds (MOFs) are compounds consisting of metal ions or clusters coordinated to organic ligands to form one-, two-, or three-dimensional framework structures. They are characterised by having channels and pores that can be of useful for intercalation and de-intercalation of ions in battery materials. Therefore, it would be of interest to synthesise and electrochemically characterise MOFs formed by the structures reported in this thesis together with organic ligands and ionic liquid as solvent.

Appendix

Atomic positions table A1: Fe-1 at 173 K; each value was multiplied by 10^{-4}.

Atom	X	Y	Z	U_{iso} or $_{equiv}$
Fe(1)	5000	5000	0	9(1)
Fe(2)	359(1)	-475(1)	2584(1)	10(1)
P(1)	1717(1)	3802(1)	3774(1)	118(18)
P(2)	2688(1)	-1538(1)	-374(1)	105(18)
P(3)	2456(1)	3026(1)	-715(1)	126(18)
P(4)	2529(1)	-1247(1)	5164(1)	125(18)
Na(1)	5000	5000	-5000	254(4)
O(1)	692(3)	-1116(2)	6461(2)	156(4)
O(2)	1445(3)	2260(2)	5446(2)	147(4)
O(3)	2321(3)	-1398(2)	3746(2)	159(4)
O(4)	4076(3)	3959(2)	-986(2)	144(4)
O(5)	3176(3)	3619(2)	2277(2)	158(4)
O(6)	1535(3)	-1993(2)	1488(2)	139(4)
O(7)	3078(3)	-3114(2)	-615(2)	144(4)
O(8)	1716(3)	-163(2)	-1575(2)	148(4)
O(9)	2308(3)	5219(3)	3979(3)	160(4)
O(10)	2190(3)	1262(2)	647(2)	176(4)
O(11)	3676(3)	-2862(3)	6050(3)	229(5)
O(12)	2892(3)	3059(3)	-2469(3)	250(5)
H(1)	720(4)	4070(3)	-410(3)	0(6)
H(2)	3760(4)	0(3)	4520(3)	0(6)
H(3)	4290(4)	-860(3)	-830(3)	10(6)
H(4)	120(4)	4340(3)	3360(3)	90(7)
H(5)	2160(5)	6070(5)	3230(5)	330(11)
H(6)	3620(5)	-2990(4)	6880(4)	190(9)
H(7)	2370(6)	2340(5)	-2300(5)	330(11)

Atomic positions A2: Fe-2 at 173 K; each value was multiplied by 10^{-4}.

Atom	X	Y	Z	U_{iso} or $_{equiv}$
Fe(1)	3333	6667	410(3)	1120(12)
P(1)	-470(3)	6450(2)	2500	1330(18)
O(1)	1220(5)	6150(7)	2500	530(11)
O(2)	1640(3)	5810(3)	540(100)	210(4)

Atomic positions table A3: **Fe-3** at 173 K; each value was multiplied by 10^{-4}.

Atom	X	Y	Z	U_{iso} or $_{equiv}$
Fe(1)	5000	5000	0	206(10)
P(1)	136(7)	2722(4)	688(2)	235(11)
Na(1)	5000	0	0	720(4)
O(1)	5010(20)	5687(12)	1205(6)	430(3)
P(2)	5703(14)	7247(6)	1797(3)	640(2)
O(2)	-2440(20)	2925(15)	2620(8)	490(3)
O(3)	2360(30)	3020(17)	158(7)	540(4)
O(4)	320(30)	646(16)	101\5(\\8)	560(4)
O(5)	4160(3)	7158(16)	2588(8)	700(5)
O(6)	5590(6)	9210(16)	1448(8)	1780(15)

Atomic positions table A4: Fe-4 at 173 K; each value was multiplied by 10^{-4}.

Atom	X	Y	Z	U_{iso} or $_{equiv}$
Fe(1)	2528(3)	1266(1)	2469(1)	73(13)
Fe(2)	2488(1)	1222(1)	-2529(1)	73(13)
P(1)	4471(1)	-231(1)	-2923(1)	120(16)
P(2)	535(1)	-203(1)	2115(1)	131(16)
P(3)	-3487(1)	4102(1)	-78(1)	84(15)
P(4)	3498(1)	907(1)	-14(1)	80(15)
P(5)	-14(1)	2514(1)	2897(1)	94(16)
P(6)	-14(1)	2475(1)	-2899(1)	104(3)
Na(1)	-1960(1)	2659(1)	-39(1)	280(3)
Na(2)	1888(1)	2330(1)	-164(1)	276(4)
O(1)	-831(2)	3015(1)	-2237(1)	132(4)
O(2)	-2814(2)	3679(1)	-985(1)	132(4)
O(3)	907(2)	2009(1)	2243(1)	122(4)
O(4)	2947(2)	1333(1)	934(1)	130(4)
O(5)	845(2)	1940(1)	-2234(1)	127(4)
O(6)	-939(2)	3017(1)	2222(1)	121(4)
O(7)	2919(2)	1295(1)	-998(1)	137(4)
O(8)	-3050(2)	3722(1)	945(1)	140(4)
O(9)	3082(2)	133(1)	22(1)	124(4)
O(10)	-5283(2)	4043(1)	-248(2)	187(4)
O(11)	830(2)	573(1)	2240(1)	140(4)
O(12)	-3060(2)	4879(1)	-84(1)	137(4)
O(13)	-1175(2)	2117(1)	3643(1)	167(4)
O(14)	1153(2)	2911(1)	3653(2)	170(4)
O(15)	-483(2)	1684(1)	218(2)	204(4)
O(16)	447(2)	3295(1)	231(2)	206(4)
O(17)	4182(2)	544(1)	-2784(1)	150(4)
O(18)	6055(2)	-454(1)	-2617(2)	182(4)
O(19)	-1191(2)	2092(1)	-3664(2)	198(4)
O(20)	5306(2)	976(1)	-47(2)	181(4)
O(21)	-1105(2)	-392(1)	2314(1)	154(4)
O(22)	1134(2)	2851(1)	-3681(1)	196(4)
O(23)	4217(2)	-447(1)	-4113(2)	251(5)
O(24)	3307(2)	-667(1)	-2239(2)	291(5)
O(25)	1567(2)	-634(1)	2924(2)	313(5)
O(26)	942(3)	-463(1)	984(2)	363(6)
H(1)	1190(5)	1690(2)	3610(3)	450(12)
H(2)	880(4)	3258(19)	3890(3)	250(9)
H(3)	3490(5)	220(2)	4400 (3)	520(12)
H(4)	630(4)	1340(2)	130(3)	360(11)

H(5)	550(4)	365(2)	150(3)	330(10)
H(6)	350(5)	1560(2)	870(3)	500(12)
H(7)	390(5)	3460(2)	890(4)	580(13)
H(8)	1660(5)	220(2)	710(3)	420(11)

Atomic positions table A5: Fe-4 at 273 K; each value was multiplied by 10^{-4}.

Atom	X	Y	Z	U_{iso} or $_{equiv}$
Fe(1)	2520(1)	-3757(3)	7529(1)	86(15)
Na (1)	3073(12)	-2658(1)	5088(5)	392(6)
P(1)	537(9)	-5217(1)	7901(3)	152(8)
P(2)	5000	-2500(18)	7900	127(17)
P(3)	0	-2500(5)	7104	113(1)
P(4)	1519(1)	-4100(2)	5044(2)	99(1)
O(1)	822(5)	-4447(2)	7766(2)	185(1)
O(2)	-1073(7)	-5428(1)	7654(1)	223(3)
O(3)	857(2)	-5444(14)	9070(9)	358(5)
O(4)	1646(2)	-5647(1)	7161(1)	378(4)
O(5)	5849(16)	-1964(12)	7234(8)	162(3)
O(6)	6156(18)	-2872(13)	8676(9)	248(4)
O(7)	1155(17)	-2105(1)	6342(9)	233(4)
O(8)	-276(2)	-4033(13)	5140(11)	238(4)
O(9)	1936(2)	-4878(9)	5022(9)	194(4)
O(10)	927(16)	-3002(12)	7770(8)	146(3)
O(11)	2136(2)	-3691(12)	5982(7)	184(4)
O(12)	2011(2)	-3696(11)	4063(7)	178(4)
O(13)	4519(4)	-1687(3)	4768(2)	298(14)
H(1)	4093(4)	-1575(3)	4905(2)	6870(14)
H(2)	-5982(5)	-4743(2)	7437(18)	895(10)

Atomic positions table A6: Mo-1 at 273 K; each value was multiplied by 10^{-4}.

Atom	X	Y	Z	U_{iso} or $_{equiv}$
Mo(1)	2290(3)	7256(3)	1163(2)	91(12)
Na(1)	2605(15)	2805(14)	2487(5)	147(2)
F(1)	1429(2)	6759(2)	2411(7)	139(2)
F(2)	4187(2)	9888(2)	1617(6)	143(2)
F(3)	5201(19)	5394(2)	1632(6)	132(2)
F(4)	899(2)	4177(2)	1092(7)	171(3)
O(1)	3379(3)	7404(3)	212(11)	186(4)
O(2)	-421(2)	8802(2)	1077(8)	172(3)

Atomic positions table A7: Mo-2 at 273 K; each value was multiplied by 10^{-4}.

Atom	X	Y	Z	U_{iso} or $_{equiv}$
Mo(1)	2500(3)	2500(3)	7649(2)	116(1)
K(1)	7500(1)	2500(3)	5000(1)	123(2)
Na(1)	2500(15)	2500(14)	2383(5)	111(2)
F(1)	2500(2)	2500(2)	6474(7)	2129(2)
F(2)	1952(2)	1952(2)	7522(6)	1790(2)
F(3)	2500(19)	2500(2)	-25144(6)	3013(2)
F(4)	241(2)	241(2)	7292(7)	233(3)
O(1)	2500(3)	2500(3)	9579(11)	298(4)
O(2)	2500(3)	2500(3)	15166(8)	122(3)

Atomic positions table A8: Mo-3 at 273 K; each value was multiplied by 10^{-4}.

Atom	X	Y	Z	U_{iso} or $_{equiv}$

Mo(1)	1458(18)	8975(14)	1643(17)	106(6)
Mo(2)	-1379(1)	10974(14)	1305(17)	96(6)
Mo(3)	3635(17)	11400(15)	1453(16)	93(5)
Mo(4)	3524(17)	13565(14)	3837(16)	87(6)
K(1)	1011(5)	10948(4)	-1020(5)	177(12)
K(2)	-3600(5)	11258(4)	3558(5)	161(11)
K(3)	1274(5)	13708(4)	1159(5)	188(11)
K(4)	6023(5)	13751(4)	6024(5)	153(11)
F(1)	4248(13)	10860(11)	2836(13)	177(3)
F(2)	-1455(13)	10534(10)	-242(12)	191(3)
F(3)	1943(13)	14388(10)	3375(13)	163(3)
F(4)	168(12)	10080(10)	1169(15)	230(3)
F(5)	2201(12)	10497(11)	2055(13)	172(3)
F(6)	4038(13)	14292(11)	2536(13)	190(3)
F(7)	2769(13)	12512(8)	2606(11)	131(3)
F(8)	1943(12)	9343(11)	155(12)	165(3)
F(9)	846(14)	9270(11)	3111(13)	201(3)
F(10)	2422(12)	11966(11)	503(13)	168(3)
F(11)	2397(13)	12799(10)	4729(13)	156(3)
F(12)	-1151(13)	10826(12)	2897(13)	195(3)
O(1)	557(2)	7972(14)	1352(17)	208(4)
O(2)	4064(14)	10425(13)	598(17)	196(4)
O(3)	2720(16)	8375(13)	2050(16)	197(4)
O(4)	-2774(2)	11441(13)	1368(16)	187(4)
O(5)	3767(15)	14498(13)	4811(15)	164(3)
O(6)	-561(17)	12059(13)	1130(16)	200(4)
O(7)	4686(17)	1210(14)	1241(17)	199(4)
O(8)	4718(16)	12791(13)	4006(15)	172(4)